Doppler Imaging of Starspots: Spectral Diagnostics. A Case Study of the RS CVn Star σ Geminorum

vorgelegt von
Alina A. Semenova
aus Pavlograd/Ukraine

Göttingen 2006

D7
Referent: Prof. Dr. Stefan Dreizler
Korreferent: Prof. Dr. Sami K. Solanki
Tag der mündlichen Prüfung:

Dedicated to my sister...

Contents

1 Introduction

The study of cool stars is an important topic in astrophysics. Stars are considered to be cool stars with photospheric temperatures $T_{Ph} < 7000$ K and spectral types later than A, i.e. stars with an outer convection zone. Convection combined with high stellar rotation leads to the appearance of a dynamo mechanism which converts the mechanical energy of convective rotation and motion into magnetic energy. Sighns of stellar activity (for example, spots or plages), as a result of magnetic dynamo, appear on the surface. The activity level depends mainly on the rotation velocity: the faster a star rotates, the more active it is. In the Hertzsprung-Russel Diagram, where the spectral class or the surface temperature is given on the x-axis and the luminosity on the y-axis (Fig. 1.1), cool stars occupy the right side (hatched region).

A typical example of a star from this class is our Sun. The Sun is a normal star – a yellow dwarf – from the middle-lower part of the main sequence with the spectral class G2 and the effective temperature 5777 K. Because of its rather close distance to the
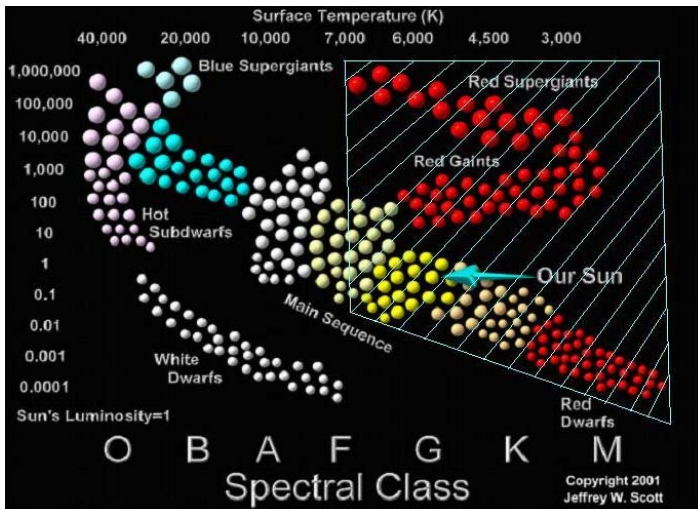
Figure 1.1: Herzsprung-Russel Diagram. The hatched section on the top right marks the location of cool stars.

Earth (approximately 1.5×10^8 km), it was the first star where activity on the surface was observed. A first report about sunspots was published on 9th of March, 1611 by David Febricius not long after the telescope had been brought into astronomy in 1609 by Galileo Galilei.

Although observational techniques have evolved much since that time, the Sun is still the only star where details of the topographic structure can be observed directly (except α Ori= Betelgeuse, whose surface has been directly imaged with the Faint Object Camera on the Hubble Space Telescope in March 1995). Even using the largest telescopes, one cannot resolve the surface structure of other stars. It is only possible to observe the surface-integrated radiation emitted from the visible stellar disk, e.g. the radiation flux. However, it is known that the activity phenomena like those on the Sun also occur on other stars.

The underlying mechanisms of activity phenomena in stars of different spectral classes are of different origin. Single and well separated binary stars the cause of activity is stressing of the magnetic field by convective motions. Members of close binary systems, such as the RS Canum Venaticorum systems, have an additional mechanism — the interaction of magnetic fields with the magnetospheres of the companion star. In pre-main sequence stars magnetic fields can also interact with the accretion disk.

Obviously, investigations of physical processes on the Sun help in understanding of structuring and evolution of stellar atmospheres. Many of the physical processes assumed to occur on stars are known from the Sun. However, the study of only one star is not enough if one wants to be able to predict how the magnetic activity of a star with a given spectral type, temperature, mass, chemical composition and rotational period will evolve in time until its end.

2 Doppler Imaging Technique

2.1 Starspots: history, properties, comparison with sunspots

One of the *visible* signs of a magnetic field on a star is the presence of cool features (e.g. spots) on its surface. First indirect observations of stellar spots were made by Hertzsprung (1924) without knowing the origin of this phenomenon: a different brightness of the same star was observed during one observing night. Hertzsprung supposed that it was an asteroid which fell down on the star and caused the change in brightness. Later, in 1950, the International Astronomical Union (IAU) classified all stars with similar behaviour to the new class of periodically variable pulsars. However, now we know that in this case we are dealing with stars covered with spots similar to those observed on the Sun.

The existence of magnetic activity on the surface and in the atmosphere of several types of stars is today generally accepted and has been investigated by several methods. For example, measuring the chromospheric excess emission can indicate a presence of magnetic activity Wilson (1978). Ca II H and K emission and X-ray emission serve as probes of the high chromospheric and coronal activity. The presence of cool spots on the stellar surface is indicated by the periodic variation of the visible light during a star's rotation. To specify this activity on the rapidly rotating stars in more detail one can analyse time-series of spectral line profiles Rice (1996). This method is called Doppler Imaging and it will be described later in this chapter.

At present, we know 8 groups of stars which are believed to have spots of magnetic origin on their surfaces (Berdyugina 2005). There are:

1. red dwarfs and BY Draconis stars (main sequence star of spectral type M or late K with the mass range from $0.08M_\odot$ to $0.5M_\odot$);

2. solar-type stars (similar to the Sun in mass and evolutionary state stars on the lower main-sequence with a spectral type from F7 to K2);

3. T Tauri stars (young, less than 10 million years, pre-main-sequence stars of about $1M_\odot$);

4. FK Com stars (late-type giants of G to K spectral type with a very short rotational periods of only a few days);

5. RC CV type stars (close detached binaries with a more massive primary component, which is G-K spectral type giant and the secondary component, which is a G-M spectral type subgiant or dwarf);

6. W Uma stars (eclipsing binaries, which consist of two solar-type components surrounded by a common envelope and have a periods of $5 - 20$ h);

7. Algols (eclipsing binaries with a hot, main-sequence primary component of B-F spectral class and a cool evolved, less massive secondary component, which is a G or K subgiant).

Although stellar spots are believed to be similar to sunspots, there are two major differences between them. First, all of the detected stellar spots have sizes much lager then sunspots. First observations of photometric variability predicted stellarspots 100 times bigger than sunspots Hall (1972), Rodono et al. (1986). This can be a result of a larger amount of magnetic flux on active stars or the low resolution of the detection techniques: it is possible that a group of small spots is seen as one big spot.

The second difference between starspots and sunspots is the location on the stellar disk. Usually starspots occupy higher latitudes then spots on the Sun. Stellar spots can be present at different positions: both low and high latitudes or even polar caps Strassmeier (1996), Piskunov (1990). This fact can be explained in two ways: first, the Coriolis force which is stronger on more rapidly rotating stars can deflect spots towards the pole, or, a possible meridional circulation can transport the magnetic flux and thus the starspots to higher latitudes Schuessler and Solanki (1992). A very interesting and still open question is whether these stellar spots show similarities to the solar spots.

The only way to check this is to observe different spotted stars during periods which are much longer than the lifetime of their spots. How can one do this if it is possible to see the structured disk only of one star - our Sun? For other stars, all that one can see is the disk integrated radiation coming out from the outer layers (photosphere, chromosphere, transition region and corona). Applying the Doppler Imaging technique, we can reconstruct surface maps of some stars from sets of high resolution spectroscopic observations.

2.2 Basics of the Doppler imaging technique for mapping of stellar surfaces

Doppler Imaging is an inversion technique to reconstruct 2-dimensional (latitude and longitude) images from a time series of 1-dimensional (intensity) spectral line profiles, taken at different rotational phases. This technique is based on the effect discovered by the Austrian mathematician and physicist Christian Doppler in 1842.

In the non-relativistic limit one can find the absolute value of the Doppler shift, $|\Delta\lambda_0|$, for the wavelength λ using the equation:

$$\frac{|\Delta\lambda_0|}{\lambda} = \frac{v_r}{v_w}, \tag{2.1}$$

where λ_0 is the so called rest wavelength (e.g. the wavelength (or frequency) which the source (star) emits when it has no radial velocity), v_w is the velocity of the wave, for example the speed of sound or the speed of light (in this case we will have $v_w = c$, where c is the speed of light) and $v_r \ll c$ is the radial velocity of the source with respect to the receiver. The sign for the Doppler shift $\Delta\lambda_0$ depends on the direction the source's radial velocity v_r.
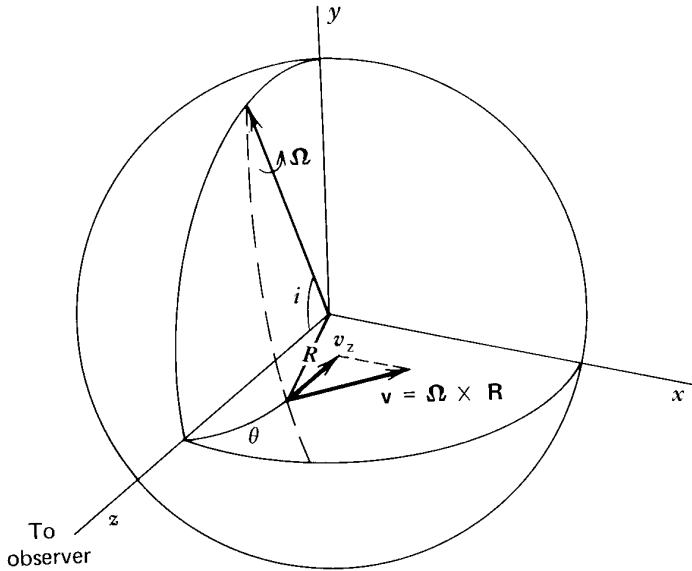
Figure 2.1: A schematic presentation of a rotating star in spherical coordinates. The rotation axis of the star lies in the y plane. The angular velocity is Ω and i is the inclination angle. Further details are given in the text.

The idea to use the Doppler effect for rapidly rotating stars to reconstruct their surface maps (for example, the temperature distribution) first came to Deutsch (1957), Deutsch (1958). The general method was mostly devised by Russian astronomers (Goncharskii et al. (1977), Goncharskii et al. (1982); Rice et al. (1981)). The term Doppler Imaging was introduced by Vogt and Penrod (1983b). Essential contribution to the investigation of the inverse problem and stellar surface reconstruction was done by Cameron and Horne (1985), Rice et al. (1989), Collier Cameron et al. (1990), Jankov and Foing (1992), Piskunov and Rice (1993), Kurster (1993) and Unruh and Collier Cameron (1995).

First of all a star is assumed to be spherical and rotate as a rigid body. Then, a spherical coordinate system is chosen such, that the z-axis corresponds to the line of sight and is directed to the observer (see Fig. 2.1). The rotation axis is prescribed to lie in the y-z plane and forms an angle to the z-axis (inclination angle i). The star rotates with the angular velocity $\vec{\Omega}$. Then each point on the stellar surface has a linear velocity which is equal to the vector product of the angular velocity $\vec{\Omega}$ and the radius vector $\vec{R}$:

$$v = \vec{\Omega} \times \vec{R} \, .$$

The Doppler shift results from the z component of the vector product, $y\Omega_x - x\Omega_y$. The

coordinate system is chosen such that the $x - z$ component of Ω vanishes. Then, $\Omega_x = 0$ and $\Omega_y = \Omega \sin i$. In this case the Doppler Shift is

$$\Delta\lambda = v = x\,\Omega \sin i\,. \tag{2.2}$$

This means, that all points on the stellar surface which have the same x coordinate have the same Doppler shift.

Let us divide a stellar disk into 5 vertical stripes of the same area as shown on top of Fig 2.2 (Vogt and Penrod 1983a). The radial velocity, v_r, within a given strip has approximately the same value. Now let the star rotate in anticlockwise direction. Then the regions I and II are moving towards the observer with $v_r^{I,II} > 0$. The region III does not move along the line of sight, such that $v_r^{III} = 0$ (neglecting any motion of the star as a whole relative to the observer). Finally, regions IV and V are receding with $v_r^{IV,V} < 0$ from the observer. Thus the spectral line profiles from regions I and II have a blue shift. There will be no shift for the lines produced in the middle region III. A red shift can be observed for the regions IV and V. The final spectral line profile which one gets from the integration over all 5 regions on the disk will be broader then the line from a non rotating object and will provide information about the rotation of the star (see left panels of Fig. 2.2).

Assume now that 50% of the middle region III are covered by an absolutely black spot (which means that this region emits zero flux). Then the region III produces a local continuum which is 50% less compared with not spotted regions (see the right-hand side of Fig. 2.2). The final integration of the absorption line profile over all regions results in a bump in the central part. This line distortion looks like an emission peak, which is not the case. It shows only that there are less photons originating from region III which can be absorbed by the line.

The Doppler Imaging Technique is based on the fact that all points on the stellar surface with the same radial velocity correspond to the same point in a spectral line profile. This means that there is a relation between the position in the spectral line and the position on the stellar disk. Obviously, the technique will work best if the line profile width is dominated by rotational broadening.

Clearly, from one spectrum of a spotted star it is only possible to find the information about the longitude of the cool feature on the stellar surface. In order to reconstruct the latitudinal position, time series of spectral line profiles taken at different rotational phases of the star are necessary. The spot is observed from different angles as the star rotates. Thus, the bump appears at different parts of the line profile. After having analysed all available spectra it is possible to say whether the spot is close to the pole or to the equator. For example, in the top series of Fig. 2.3 we see the distortion created by a spot closer to the pole in a line profile. In this case the bump will always stay close to the central part of the spectral line and never reach its wings. In addition, the speed with which its position changes across the spectral line will be very slow. In case of a spot at the low latitudes (bottom series in Fig. 2.3) the bump travels across almost the whole line profile with a speed higher then in the first case. The frequency remains the same in both cases, however, unless the star shows a strong differential rotation.

This is, of course, a very simple example and in practice the things are more complicated. One difficulty is that one has to take into account the position of the spot on the
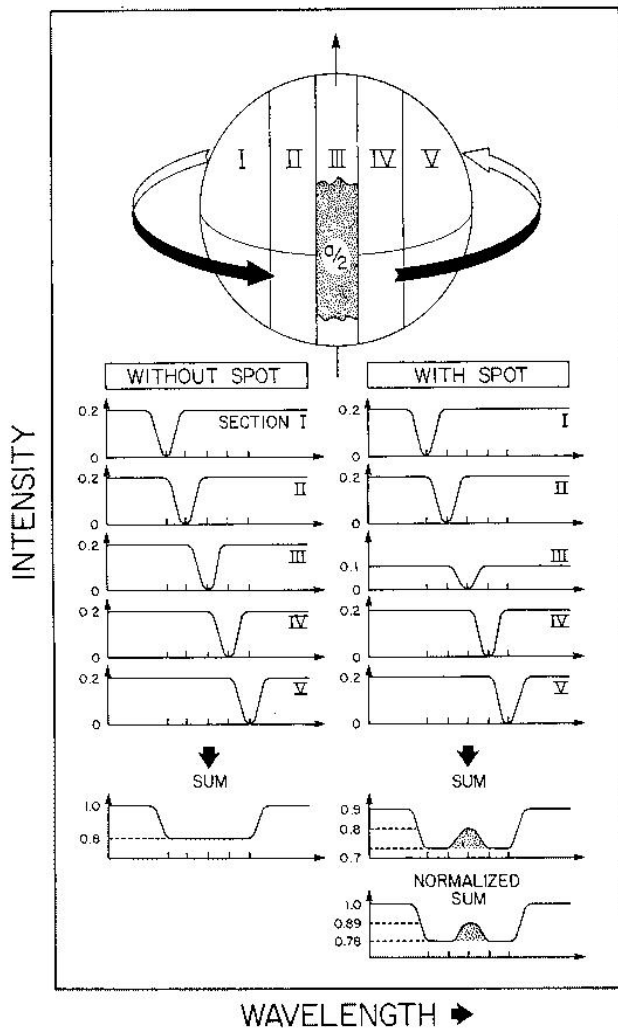
Figure 2.2: Illustration of the line broadening mechanism for a rapidly rotating star due to the Doppler shift (left side) and the formation of a bump in the line profile in the case of a spotted star (right side) by Vogt and Penrod (1983b)
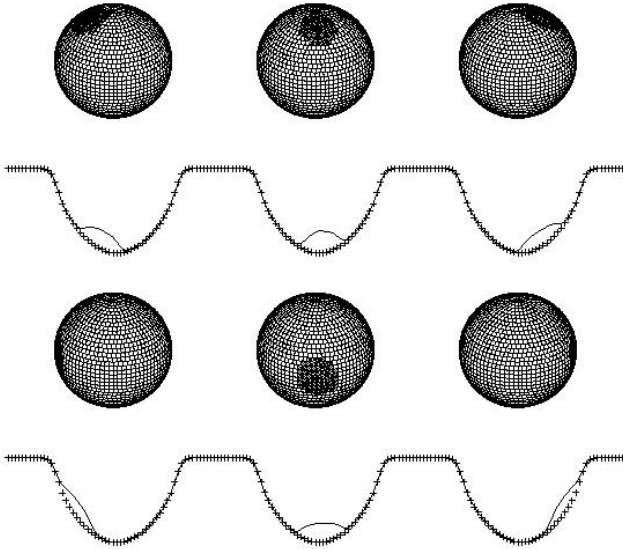
Figure 2.3: Top series: a high latitude spot on a rotating star and the resulting deformation of the line profile. Bottom series: the same for a low latitude spot by A. Hatzes

stellar disk, because the "visibility" of the spot depends on the limb angle. A spot close to the limb will produce a weaker bump then a spot in the central part.

Zeeman-Doppler imaging is one of the adapted variant which allows to reconstruct both the temperature distribution on the stellar surface and the magnetic field map analysed fpr polarization Semel (1989), Donati and Semel (1990), Brown et al. (1991).

2.3 Necessary conditions for Doppler imaging

A necessary condition for a star to be a candidate for Doppler imaging is a high rotational velocity or more precisely, a high $v \sin i$. Then the rotational broadening is the main line broadening mechanism. In a first approximation the number of elements that could be resolved on the stellar surface is approximately $2v \sin i/W$ (where $v \sin i$ is the projected rotational velocity and W is the full width of the line profile at its half-maximum in case of no rotation). Typically, $W \approx 10$ km/s for spotted cool stars, in particular RS CVn primaries like the star, studied here, which puts a limit of about $20 - 30$ km/s on the projected velocity ($v \sin i$) of the star.

On the other hand, the equivalent width of the lines is almost fixed even for different
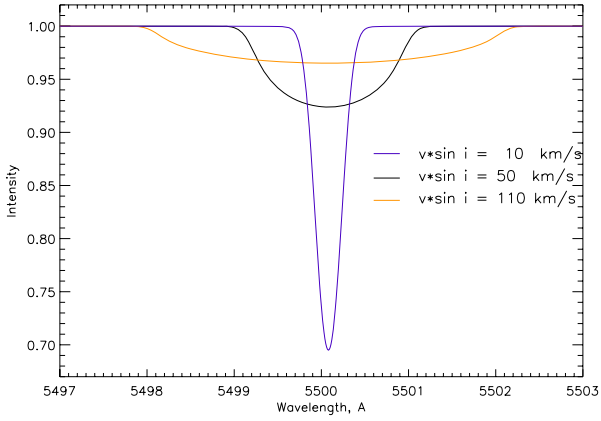
Figure 2.4: Line profiles calculated with different projected rotational velocities $v \sin i$

Table 2.1: Summary of the requirements for Doppler imaging.

Observations	
Phase coverage	> 6 observed spectra
Spectral resolution, $\lambda/\Delta\lambda$	$\geq 30\,000$
S/N	≥ 200
Observational period	$< 2 - 3$ months
Input geometrical parameters of the star	
Projected velocity, $v \sin i$	$20 - 100$ km/s
Inclination, i	$20° - 70°$
Rotational period	$\neq$ n days and < 2 months

rotational velocities. Therefore, stars with higher rotational velocities will produce less deep lines. The maximum value which a "bump" in the line profile can reach is around $3 - 4\%$ of the continuum, but it is usually around 1% i.e. for average sized spot. If the lines are too shallow, the small "bump" produced by the spot on the stellar surface cannot be distinguished from noise. The problem of a great number of telluric lines, which are always present in some wavelength bands of the spectra and are not identified, also has to be taken in account. Thus only stars with $v \sin i$ not more then $80 - 100$ km/s are usually considered. Three different line profiles calculated for different $v \sin i$ are shown in Fig. 2.4.

11

It is also important to have highly resolved spectra with $\lambda/\Delta\lambda \geq 30\,000$. Because of the small size of the "bumps" (usually only 1% of the continuum) a high signal-to-noise ratio (S/N $\geq$ 200) is needed for the observed spectra. In order to get a more precise stellar surface map, one needs to have a set of observations which is covering as many different rotational phases as possible. The rotational phase of the star should not be equal to $24n$ hours (where n= 1, 2, 3...), otherwise each night the same phases are observed. For the method to work, at least 6 different rotational phases need to be observed. Observations for one Doppler Imaging study have to be taken within approximately 2 or 3 months (not longer). It is assumed that within this short time period spots cannot evolve too much. For the analysis it is better to choose several temperature insensitive and unblended spectral lines.

Stars with inclinations equal to zero (i.e. $i = 0°$, so that the rotational axis lies on the line of sight) cannot be used either because then $v_r = 0$ km/s and Doppler imaging is impossible. Also, $i = 90°$ is not suitable for Doppler imaging as in this case it is not possible to distinguish whether the cool feature is located in the northern or southern hemisphere. This will affect all results obtained from inclinations bigger then 70°. Thus, the best is to have $20° \leq i \leq 70°$.

In Table 2.1 a summary of the necessary restrictions for the star to become a candidate for Doppler Imaging are given, together with appropriate observational conditions for stellar surface reconstruction.

All geometrical parameters (rotational period, $v \sin i$ and i) as well as physical parameters (like the spectral type, effective temperature, T_{eff}, gravitational acceleration, $\log g$, macroturbulence, ζ, and microturbulence, ξ) have to be determined with high precision.

2.4   Basics of the inverse problem

2.4.1   Calculation of Doppler shifted spectral line profiles

First of all, it should be explained how the shape of a spectral line profile is calculated for a star without rotation. In Fig. 2.5, a spherical surface is used to represent a star with a spherical coordinate system in its center. θ is the angle between an arbitrary point M and the line of sight. $dS(M)$ is an infinitesimal surface element. From the basics of radiative transfer it is known that the flux, F, is equal to $\int dI \cos(\theta) dS(M)$, where I is the intensity. Thus the line depth at the wavelength λ is

$$R(\lambda) = \frac{F_c - F_\lambda}{F_c} = 1 - \frac{F_\lambda}{F_c} = 1 - \frac{\oint I_\lambda \cos(\theta) dS(M)}{\oint I_c \cos(\theta) dS(M)}, \qquad (2.3)$$

where F_c and I_c are the flux and intensity of the continuum, F_λ and I_λ are the flux and intensity at the wavelength λ, $\oint$ is the integral over the visible stellar surface.

In practice the star is rotating and a shift $\Delta\lambda$ is observed for the central wavelength λ_0 of the line profile at the point M. In this case, the line depth also depends on the rotational phase of the star which is assumed to be known and equal to $\Phi = \omega(t_0)$, where ω is angular velocity, t_0 is time corresponding to phase 0. Now, Eq. 2.3 can be rewritten in the form:
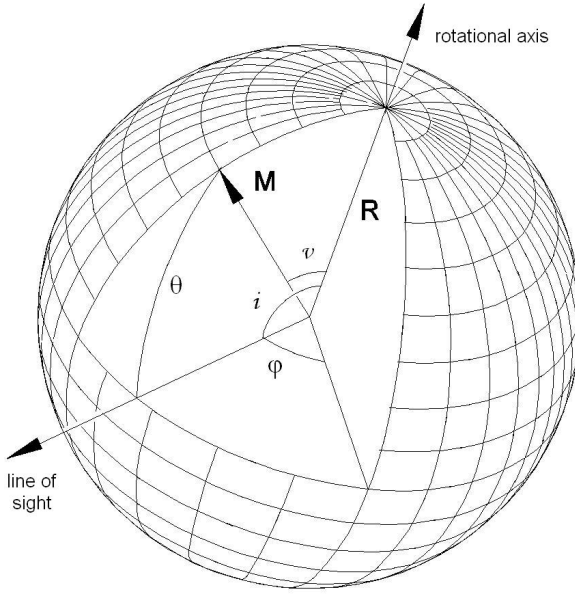
Figure 2.5: Stellar surface in spherical coordinates as used for Doppler imaging. R in fig. is radius, not to be mixed up with $R(\lambda)$ in Eq. (2.3)

$$R(\lambda, \Phi) = 1 - \frac{\int \int I(M, \theta, \lambda + \Delta\lambda(M)) \cos(\theta) dS(M)}{\int \int I_c(M, \theta) \cos(\theta) dS(M)}, \qquad (2.4)$$

where M represents the spatial coordinates across the stellar surface (longitude and latitude), θ represents rotational phases and wavelengths or (equivalently) radial velocities, $I(M, \theta, \lambda + \Delta\lambda(M))$ is the local intensity at the surface point M. If I and I_c are represented as functions of the coordinates on the stellar surface and specified by M with the stellar longitude φ and latitude θ, then the shape of the local line profile (i.e. line absorption normalized to local continuum intensity) which depends on the coordinate M and rotational phase θ) is

$$R_{loc}(M, \theta, \lambda) = 1 - \frac{I(M, \theta, \lambda)}{I_c(M, \theta)} . \qquad (2.5)$$

Doing so, Eq. 2.4 becomes

$$R(\lambda, \Phi) = 1 - \frac{\int \int I_c(M, \theta) R_{loc}(M, \theta, \lambda + \Delta\lambda(M)) \cos(\theta) dS(M)}{\int \int I_c(M, \theta) \cos(\theta) dS(M)} . \qquad (2.6)$$

13

The basic problem is now in the definition of the local line profile R_{loc} which we observe at angle θ (Eq. 2.5). $R_{loc}(M, \theta, \lambda)$ depends on the abundances of elements at point M, line broadening mechanism and the structure of the atmosphere. In order to find the dependence of the local surface brightness $I_c(M, \theta)$, which includes limb darkening and intrinsic inhomogeneities, on angle θ, the center-to-limb darkening law of the star for the continuous spectra has to be known. Basically, Doppler Imaging Technique is stable against errors in the calculation of line profiles with different limb darkening dependence (Unruh and Collier Cameron 1995). If one defines $\Lambda(\theta) = 1 - \gamma + \gamma \cos(\theta)$, where γ is the limb darkening coefficient and $\theta = \theta_0 = 0$, then the local surface brightness is

$$I_c(M, \theta) = I_c(M, \theta_0) \Lambda(\theta) .\qquad(2.7)$$

The main task of Doppler Imaging is to reconstruct the stellar surface brightness distribution from a given set of line profiles I_t needs the solution of an integral equation:

$$D(\theta) = \int P(M, \theta)\, S(M) dM ,\qquad(2.8)$$

where $D(\theta)$ is the observed function (data), $S(M)$ is the function, which needs to be reconstructed (an image), M and θ, as was written before, represent the coordinates on the stellar surface and the rotational phase accordingly. All information about geometric conditions, local stellar line profiles, stellar limb darkening and instrumental characteristics is included in the response function $P(M, \theta)$. Thus, we need to find $S(M)$. Finding the integrand if the integral is known as an inverse problem.

2.4.2 The inverse problem

Mathematically, the inverse problem for solving Eq. 2.8 to restore the the image $S(M)$, can be presented as a matrix equation:

$$D = PS \quad \text{or} \quad D_i = \sum_{j=1}^{n} P_{ij} S_j, \quad i = 1, ..., m ,\qquad(2.9)$$

where D is a data set with m points. The task is now to reconstruct a composition of the parameters over the stellar surface S which consists of n image pixels. The set of measurements is a data vector D now. The set of image pixels is an image vector S. The response matrix P is the discrete version of the response operator. The elements of the matrix P are given by $P_{ij} = \partial D_i / \partial S_j$. Using P, it is possible to find how the image (S) can be transformed to the model (D). In the simple case when the number of data points is equal to the number of points over the stellar surface ($n = m$) the matrix P can be simply inverted into the matrix P^{-1} in order to solve Eq. 2.8. In spite of that, this is an ill-possed or underdetermined problem. The inverse matrix P does not exist. Thus the number agreeable with the data solutions is infinite. In addition, as the data will never be free of noise, such a solution will be unstable, however. Problems of this type are in general called ill-conditioned. To this type belong models which do not satisfy one of the following properties:

- a solution exists;

- the solution is unique;

- the solution depends continuously on the data, in some reasonable order.

One of the best variants to solve this problem is to select one particular solution (image) from all possible. This can be done by applying some additional constraint on the solution. Then one has a unique solution, the inverse problem becomes well-posed and it is called *regularized*.

In general, one has to deal with the case when $m \neq n$. Then, the observed data D and the distribution of parameters over the stellar surface S have a probability density function $f(D; S)$. The overall probability to obtain D is the so-called *likelihood function*:

$$L = \prod_{j=1}^{m} f(D_j; S),$$ (2.10)

where D_j is given statistically independent observations. There is a single value of D_j that is most likely; that is, makes the likelihood, L, as big as possible. That value of L is known as the maximum likelihood estimate. Thus, one has to find a solution which maximizes L. This solution is given by the following system of equations:

$$\frac{\partial}{\partial S_i} \ln L(S) = 0, \quad i = 1, n.$$ (2.11)

We get the observed data D when the solution corresponds to the maximum probability. Due to noise in the data which cannot be reduced, such a solution is not executable. Thus, during calculation of the highest probability at some point we start to fit the noise. In order to protect our solution from fitting the noise we can set up a limit L_0 for the overall probability where the calculation has to stop:

$$L = L_0.$$ (2.12)

Even with a limited overall probability, still a lot of solutions exist which are rather different and satisfy the condition Eq. (2.11). Now only one of them has to be chosen. To select the appropriate, reasonable and not noisy solution two different approaches to the inverse problem can be applied: the Bayesian approach and the Occamian approach. For the last two decades several codes for Doppler Imaging have been developed. They all use on the common method to invert the spectral lines information to the stellar surface map using the regularization technique. However, they are based on either of the two approaches and differ mainly by the applied regularization limits to get a unique solution.

2.4.3 The Bayesian approach and codes based on it

"Bayesian" probability or "Bayesian" theory is named after Thomas Bayes (1702 - 1761). The term Bayesian, however, came into use not before 1950, and in fact it is not clear whether Bayes really introduced the very broad interpretation of probability, now called "Bayesian". The Bayesian interpretation of probability allows probabilities to be assigned to random events, but also allows the assignment of probabilities to any other kind of statement. In other words, to choose a unique solution one needs to invoke some *prior*

information (additional constrains $g(S)$, where S the distribution of temperature over the stellar disk) on the properties of the solution and then to maximize the functional

$$\Phi = \ln L(S) + \lambda \, g(S) \, , \tag{2.13}$$

where λ is a Lagrange multiplier which is determined under the condition given by Eq. (2.11). Different codes which are based on the Bayesian approach have different definitions of $g(S)$. For example:

- the Tikhonov method (TM) (Goncharskii et al. 1977) searches for the solution with the minimum gradient of the parameters across the stellar map ($g(S) = \text{grad}S$), thus, it considers as a right solution the smoothest image consistent with the data;

- the Maximum Entropy Method (Vogt et al. 1987) searches the images with the minimum of information (with the least content of configurational information), e.g. with the largest entropy ($g(S) = S \, \log S$);

- the method which considers only two temperature values ($S_j \in \{S_{sf}, S_{sp}\}$, where S_{sf} and S_{sp} are stellar surface and spot temperatures, respectively) was developed by Collier Cameron et al. (1990) and Kurster (1993).

All these additional constrains are artificial. They allow a reasonable, but distorted solution with an unknown bias. In principle, with the increase of quality of observations, the influence of the applied constraints is decreasing.

2.4.4 The Occamian approach

Around ten years ago Terebizh and Biryukov (1994), Terebizh and Biryukov (1992) and Terebizh (1995a), Terebizh (1995b) introduced a non-Bayesian approach to the inverse problem. The new approach is based on the philosophical principle of "Occam's Razor" propounded by the English philosopher William of Occam (1300- 1349). This principle advocates that "Entia non sunt multiplicanda praeter necessitatem" (Latin for "Entities should not be multiplied more than necessary" or, in other words, one should not increase the number of entities required to explain anything beyond what is necessary). The principle states that one should not make more assumptions than the minimum needed.

The new method for the calculation of the inverse problem is called the Occamian approach and it has several features in common with the Singular - Value Deconvolution method described by Press et al. (1992). The advantage of the Occamian approach is that it uses only one artificial constraint to the solution, e.g. that the solution must be not negative. The negativity can naturally appear in many inverse problems.

The choice of the solution can be made from the analysis of all accessible information, e.g. the observational data, D, and the model, P. Based on this, one can make a first approximation of the Fisher information matrix. Using this information matrix, it is possible to determine the error ellipsoid in the space of solutions or the stable solution itself. The error ellipsoid is used to calculate the accuracy of the solution.

To make a simple description of the problem, let us consider a one-dimensional case. S is a deterministic column vector of the real non-negative parameters, that is $S = [S_1, ..., S_n]^T$ where T means a transportation operation. The statistical estimate $\tilde{S}$ of the

parameters S has to be found on the basis of the known Point Spread Function (PSF), that is the $(m \times n)$ matrix $P = [p_{jk}]$. One can write a non-negative and symmetric $(n \times n)$ matrix $F(S)$ as

$$F(S) \approx P^T Q^{-1} P, \quad F_{ik}(S) = \sum_{j=1}^{m} \frac{p_{ji} p_{jk}}{D_j(S)}, \qquad (2.14)$$

where Q is the diagonal $(m \times m)$ matrix with observed data set $(D_1, ..., D_m)$:

$$Q(S) = \text{Diag}[D_1, ..., D_m]. \qquad (2.15)$$

Equations (2.13) gives an explicit representation of the Fisher information matrix. When the solution is found, the observed data D has to be replaced by the model calculation R in order to reach the exact equivalence. The eigenvectors $V_1, ..., V_n$ and the corresponding eigenvalues $\Lambda_1, ..., \Lambda_n$ of this matrix define the orientation (the axis of the ellipsoid is proportional to $\Lambda_i^{-1/2}$) and the shape of the error ellipsoid. The new frame of reference with the coordinates $Y_1, ..., Y_n$ is characterized by the directions of the axes of the error ellipsoid. The coordinates $Y_1, ..., Y_n$ are a linear combination of the unknown parameters $S_1, ..., S_n$. This combination is defined by the orthogonal transform and forms the so-called principal components of $S_1, ..., S_n$:

$$Y = V^T S, \quad S = V Y, \qquad (2.16)$$

where $V^T = V^{-1}$, $V = [V_1, ..., V_n]$.

This orthogonal transform describes the rotation of the coordinate system in the space of solutions. The new coordinates Y include these 'principal components' of the solution. Then smallest eigenvalues, $\Lambda_1, ..., \Lambda_n$ of the information matrix $F(S)$ represent principal components with relatively large errors of the solution of the inverse problem. Thus, the error ellipsoid is strongly elongated in these directions. At the same time, combinations in the direction of large eigenvalues can be estimated with a much better accuracy. In addition, if these is a lack of observations and the number of points over the stellar disk, n, is smaller then the number of data points $(m < n)$, $(n - m)$ eigenvalues become zero, and the respective parameters are linear. Thus, only a part of the principal components completely covers the information of S The relatively small number of p of estimates of the principal components $\tilde{Y}^{(p)} = [\tilde{Y}_1, ..., \tilde{Y}_p]$ instead of S have to be done with a given number of restrictions: $S_k(Y) \geq 0$, $k = 1, ..., n$ and $Y_j = 0$, $j > p$. Then the transform is

$$\tilde{S}^{(p)} = V \tilde{Y}^{(p)}. \qquad (2.17)$$

Together with the restrictions listed earlier, Eq. 2.15 leads to the acceptable stable solution $\tilde{S}^{(p)}$. In that way the solution of the inverse problem in the Occamian approach has provided a fit to the observed data, D, which is statistically good enough, and with a minimum set of $\tilde{S}^{(p)}$. The choice of p makes the solution unique and removing of principal components which contain no significant information but noise gives the stability for the solution.

To apply the Occamian approach the probability density function $f(D_j; S)$ and the principle for calculation of the level L_0 must be defined. It is possible to use a Gauss

function for the probability density function in case of high signal-to-noise observations. In the present realization of the Occamian approach a Poisson function is applied. It is similar to the Gauss function for high signal-to-noise observations and is never negative for low signal-to-noise observations.

A way to judge the level of goodness, L_0, was proposed by Terebizh and Biryukov (1992). They used the mean information principle and supposed that the likelihood function L is equal to its mathematical expectation value $\langle L \rangle$ or deviates from it only by a statistically inconsiderable value. Then one has $L = \langle L \rangle$ which represents the class of mean likelihood solutions. The complete information J can be found using the Shannon definition of the information, e.g.

$$J = -\ln L. \tag{2.18}$$

As a consequence, the mean likelihood principle is equivalent to the mean information principle

$$J = \langle J \rangle. \tag{2.19}$$

This procedure yields a solution containing the mean amount of information $\langle J \rangle$ rather than minimum and in the case here, with the Poisson function and a high signal-to-noise ratio, the mean information matrix is

$$\langle J \rangle = \sum_{j=1}^{m} \ln \sqrt{2\pi e R_j}, \tag{2.20}$$

where R is the calculated model. It should be mentioned that the choice of the limit for the likelihood function (L_0) does not change the main principle of the Occamian approach.

To show how the Occamian approach works on practice, let us consider that a Point Spread Function P transforms a composition of the true parameters S into a calculated model R:

$$R = PS. \tag{2.21}$$

At the same moment we have a given set of measurements D (observed data), which is:

$$D = PS. \tag{2.22}$$

Assuming that the PSF P is exactly known, we can estimate S of the true vector from this equation. To solve this problem with the Occamian Approach we have the following algorithm:

1. assuming some non-zero solution S_0 and using the model P we calculate a vector R_0;

2. calculation of a Fisher matrix for given P and D;

3. finding of eigenvalues Λ and eigenvectors V of the fisher matrix $F(S)$ and then principal components Y_0;

4. the final step is minimization of the information J down to the mean information $\langle J \rangle$ (minimization of discrepancies between the vector R_0 and D)

After the step 4, we can make a final estimation of the solution S_1 and corresponding vector R_1.

In our case the role of calculated model R plays a set of calculated with the radiative transfer equation local line profiles and the data D are observed and normalized flux profiles.

In contrast with many others techniques, the Occamian approach, during the inversion, does not presupposed a shape for the distribution of the cool features (spots) over the stellar surface.

2.5 Doppler imaging code based on the Occamian approach

In this work the Doppler Imaging set of codes developed by Berdyugina (1998) based on the Occamian approach is used. The codes are written in Fortran77 and the set consists of 5 codes for the data inversion: `chem05.f`, `sloc05.f`, `dark.f`, `sq.f`, `occ_di.f`. The codes are briefly described individually in Sect. $2.5.1 - 2.5.5$.

2.5.1 Calculation of number densities of atoms and molecules

The programm `chem05.f` calculates number densities of atoms and molecules (if the latter are included in the Doppler Imaging calculations) under the assumption of chemical equilibrium between the different atomic and molecular types (Berdyugina et al. 2003). There are two processes in order to ensure chemical equilibrium which have to be taken into account for cool stellar atmospheres: ionization and dissociation (Tsuji 1973). The assumption of chemical equilibrium means that the number of associations is equal to the number of dissociations. The number of ionized atoms is calculated from the Saha equation.

Calculations need parameters which are included in several input files with:

- parameters (names of input and output files);

- abundances of elements (in our case we used abundances of 42 elements);

- a catalogue of atomic and molecular lines included for calculations. The list of atomic lines is taken from the VALD database (Piskunov et al. 1995) for lines having a central depth not less then 1%. The information for molecular lines is taken from different sources;

- information about stellar atmospheres models taken from the Kurucz database.

2.5.2 Calculation of local line profiles

The next code `sloc05.f` calculates a set of synthetic line profiles for a given temperature range and gravity ($\log g$) using the stellar atmosphere models by Kurucz (1993). Using this code it is possible to find opacities. Furthermore, there is an option to calculate intensities or the flux in the considered wavelength interval, taking into account continuum, atomic and molecular lines opacities.

The computation is based on the output files from the above described code with the calculated number densities of atoms and molecules. Also it uses partly the same input files for `chem05.f` (list of abundances, files containing the model information). Some additional files are also used. They contain information about:

- parameters: microturbulence, considered wavelength intervals. The wavelength intervals have to include lines chosen for Doppler imaging. It is better to choose more than one line for the inversion, because simultaneous inversion of several line profiles usually reduces the effect of systematic deviations in a certain line due to noise and blends;

- information about atomic lines (name of the element, ionization state, wavelength, excitation potential, microturbulence, oscillator strength, radiative broadening, Stark gamma factor, Van der Waals gamma factor, Lande factor and the central depth) and about the molecular lines (wavelength, oscillator strength).

2.5.3   Limb darkening coefficients

As mentioned above, limb-darkening effects are important for the calculation of the broadening of line profiles of rotating stars (see Sec. 2.4.1). Using limb darkening coefficients for each limb angle makes the inversion process much faster. The code `dark.f` recalculates the local line profiles for the intensities for the concerned number of angular points on the stellar disk (normally, it is 10).

Input parameters required by this code are:

- instrumental profile;

- macroturbulence velocity.

The output file contains continuum intensity in different spectral regions, normalized local line profiles for the center of the stellar disk and limb darkening coefficients for each wavelength.

2.5.4   Surface grid and geometry

In this code the grid on the stellar surface according to the stellar parameters (inclination, number of rotational phases) is specified. The input file for the code `sq.f` includes information about

- the observed rotational phases;

- inclination;

- size of one pixel on the stellar surface;

- $v \sin i$, e.g. projected rotational velocity.

2.5.5 Inversions

The last step is to calculate the Point Spread Function from the local line profiles and to make an inversion. This step is carried out by the last code, `occ_di.f`. The algorithm is described in the previous subsection 2.4.4. The file containing observations is used in this code as well as files with area of geometrical information and local line profiles obtained as described in Sects. 2.5.3 and 2.5.4. The file with input parameters includes the following information:

- accuracy factor for neglecting of those principal components, which correspond to small eigenvalues of the Fisher matrix;

- convergence tolerance;

- the wavelength shift for the observed profiles (if necessary);

- the number of wavelength intervals used for the inversion and the intervals themselves;

- names of all input and output files.

The resulting output files contain the information about the fit of line profiles to the inverted line profiles and the final solution of the temperature distribution on the stellar surface (the temperature is recovered for each pixel).

3 Doppler Imaging of Sigma Geminorum

3.1 RS CVn binary system σ Geminorum

3.1.1 General information, orbital elements and photometric properties

Sigma Geminorum (75 Gem, HR 2973, HD 62044) is a spectroscopic binary star from the Twins constellation (lat. Gemini). It is situated on the line between two bright stars: Pollux (β Gem) and Castor (α Gem) (Fig. 3.1).
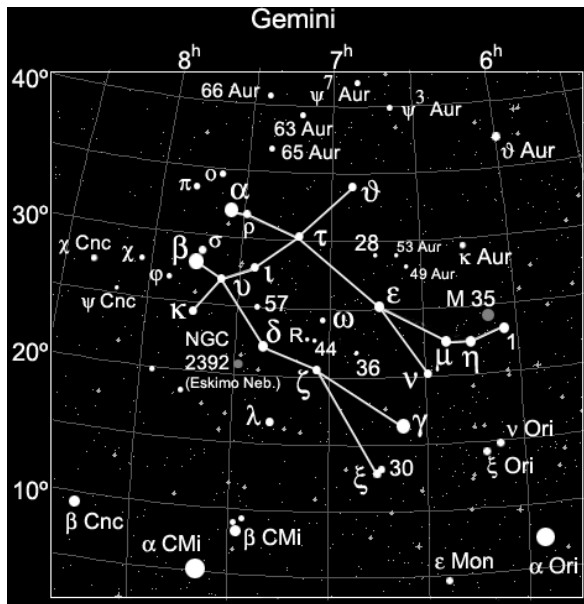

Figure 3.1: Constellation of Twins (Gemini)

Sigma Geminorum with the coordinates $\alpha = 7^h 37^m 0$, $\delta = +29° 07'$ (Harper 1911) can be seen with the naked eye and its absolute visual brightness is $M_V = 0.22$. The maximum brightness in V bandpass is $V = 4^m 14$, $B - V = 1.122$ (Strassmeier et al. 1993) or $(B - V)_{Hipparcos} = 1.118 \pm 0.006$ mag. $(V - I)_{Hipparcos} = 1.12 \pm 0.05$ mag. The luminosity of σ Gem is $L = 52.5^{+14.5}_{-8.2} L_{\odot}$. σ Geminorum is at a distance (Hipparcos) of 37.5 ± 1.1 pc. Hoffleit and Jaschek (1982) gives the distance is equal to 55.6 pc.

The binary system has a marginally eccentric orbit with the orbital eccentricity $e = 0.0210 \pm 0.0069$, but it also might be circular (Bopp and Dempsey 1989). The orbital period is almost synchronized with the rotational period of the primary component and does not show a significant variability. Values for the orbital period obtained by different authors are shown in Table 3.1. The rotational axis of the orbit is parallel to the rotational axis of the primary component. The semiamplitude for the system is $K = 34.78 \pm 0.25$ km/s. The radial velocity for the system's center-of-mass is $V_o = 43.8$ km/s. The heliocentric Julian date of conjunction with the primary behind (i. e. when the primary star passes through the ascending node) is $T_{conj} = 2,418,962.43 \pm 0^d07$ (Fried et al. 1983) or $T_{conj} = 2,447,221.2 \pm 1.^d1$ (Bopp and Dempsey 1989) or $T_{conj} = 2,447,227.08$ (Strassmeier et al. 1993).

The photometric variability of the primary component of σ Gem was first observed by Hall et al. (1977). Many authors derived the orbital P_{orb} and rotational P_{rot} periods during the last century (which are almost equal) from the light curve using different methods. Results of their studies can be seen in the Table 3.1.

Author	P_{orb} (days)	P_{rot} (days)
Harper (1911)	19.605	-
Harper (1938)	19.603	-
Hall et al. (1977)	19.6	-
Hall and Henry (1979)	19.603	19.4657 ± 0.02
Fried et al. (1983)	–	19.423
Eker (1986)	19.60468	-
Strassmeier et al. (1988)	-	19.410
Bopp and Dempsey (1989)	19.60447	-
Eaton (1990)	-	19.54
Strassmeier et al. (1993)	19.60447	19.410
Jetsu (1996)	-	19.607 ± 0.029
Duemmler et al. (1997)	-	19.60447

Table 3.1: Orbital and rotational periods for σ Gem obtained by different authors

In this work I use the values for the orbital and rotational periods from Duemmler et al. (1997), which are $P_{rot} = P_{orb} = 19.60447 \pm 0.00007$ days.

The value of the projected velocity (i. e. $v \sin i$), the photospheric temperature and the temperature of cool spots on the surface and the inclination of the primary component varies from one author to another. For a comparison of this parameters see Table 3.2.

σ Gem has $\log g = 2.5^{+0.23}_{-0.42}$, microturbulence for Ca $\xi_{Ca} = 0.7$ km/cm, microturbulence for Fe $\xi_{Fe} = 1.0$ km/s and macroturbulence $\zeta = 3.0$ (Kovári et al. 2001).

Author	T_{phot}(K)	T_{spot} (K)	$v\,\sin i$ (km/s)	i (°)
Poe and Eaton (1985)	4400	3870	-	60
Strassmeier et al. (1988)	4400	3870	25	-
Strassmeier et al. (1993)	-	-	26	60
Hatzes (1993)	4400	3850	27.0	60
Duemmler et al. (1997)	4500	-	27.0 ± 0.2	> 46
Kovári et al. (2001)	4630 ± 100	-	27.5 ± 1.0	60 ± 15

Table 3.2: Temperature of the photosphere, spot temperature, projected velocity ($v\,\sin i$) and the inclination (i) for σ Gem obtained by different authors.

The lower limit for the radius of the star can be found using the equation

$$R\,\sin i \; = \; \frac{P_{rot}}{2\pi} v\,\sin i\,, \tag{3.1}$$

where i is the inclination and $v\,\sin i$ is the projected rotational velocity. Duemmler et al. (1997) took $P_{rot} = P_{orb} = 19^d601562$ and $v\,\sin i = 27.0$ km/s and found $R_{min} = 10.5\,R_\odot$ for σ Gem. The same authors determined the limits for the mass of the primary of Sigma Geminorum as $0.4 M_\odot < M < 2.2 M_\odot$. Kovári et al. (2001) determines the radius of the star as $R = 12.3^{+1.6}_{-1.0} R_\odot$ and Nordgren et al. (1999) as $9.3\,R_\odot$.

3.1.2 Spectroscopic properties

Sigma Geminorum is a good example of a cool and well studied K1 III spectral type star from the class of RS Canum Venaticorum stars. This group of stars includes close binary systems with a massive evolved primary component (G-K giant or subgiant) and, typically, a low luminosity secondary component (G-M subgiant or dwarf). RS CVn stars show photometric variabilities, Ca II H and K emission lines, fast rotation (the rotational period is almost synchronized with the orbital period of a few days) and orbital period variations. With respect to the condition of fast rotation, σ Gem has untypically long periods for RS CVn stars. Due to the high luminosity of the primary component, σ Geminorum is a single-line binary which makes the spectral analysis of the star easier.

Strong Ca II H and K emissions were observed by many authors. The presence of this lines is a sign for chromospheric activity on the star. The absolute surface flux emitted in the H line is $F(H_2) = 5.7 \times 10^5$ erg cm^{-2} s^{-1} and in the K line F(K$_2$) = 7.0×10^5 erg cm^{-2} s^{-1} (Bopp 1983).

Smith and Bopp (1982), (Bopp et al. 1988) report about the H$_\alpha$ lines, which are definitely filed in by chromospheric emission. After a detailed high resolution study, Eker (1986) showed that the core of H$_\alpha$ varies with the orbital phase according to the stellar active regions (spot zones). The central intensity (R$_c$) of H$_\alpha$ is 0.44 when looking at the average spectrum.

σ Geminorum has an X-ray luminosity of logL$_x \approx 31.0 \pm 0.2$ erg s^{-1} (Yi et al. 1997), (Zhang and Zhang 1999), (Nordon et al. 2006), (Walter et al. 1978). This value is calculated for a distance of 37.5 pc. From the ROSAT observations it was found that the X-ray emission varies in a time range from years to hours and minutes. The spectral

analysis made by Singh et al. (1987) shows that X-ray emission on σ Gem can be interpreted by a bimodal temperature distribution with one component having a temperature of $\sim 5 \times 10^6$ K and the second component having a temperature of $\sim 40 \times 10^6$ K where the first temperature is the dominant source of X-ray emission.

Ayres et al. (1984) report about bright and broad ultraviolet emission lines of σ Geminorum. Despite the fact that the primary component of the system at V-R= 0.92 lies on the red giant branch, Sigma Gem has anomalous properties for a star of that class e.g. prominent high-temperature emissions in its far-ultraviolet spectrum and no traces of cool and low-velocity wind. It has been found that there are significant changes in the profiles of high-excitation lines (such as Si IV and C IV) during two successive days of observations, which could be produced by the rotation of large magnetic active regions on the star. Engvold et al. (1988) found redshifts of high temperature lines in far-ultraviolet spectra relative to low-excitation emission characteristic of the chromospheric layers.

3.1.3 The secondary component

The secondary component of the system Sigma Geminorum is not seen in the photometry nor in the spectroscopy. Its luminosity is not more than 1% of the luminosity of the primary. If $M_v = 0.^m3$ for the primary component, the secondary can not be brighter then $M_v \approx 5^m$ (Gray 1988). Thus the secondary can be a main-sequence star of type G6 or later, or a compact object like a white dwarf or neutron star. According to the predicted G6 spectral type, its mass must be less than 0.95 $M_\odot$ or less than 1.4 $M_\odot$ if the star is a white dwarf. From the maximum value for the mass of the star (0.95 $M_\odot$) one can calculate the lower limit for the inclination, e.g. $i > 46.°2$ (Duemmler et al. 1997).

3.2 Observations

For the present study 70 spectra of σ Gem are available. They were observed with the Nordic Optical Telescope (NOT) in La Palma and with the Telescope Bernard Lyot (TBL) at the Observatoire du Pic du Midi.

3.2.1 Nordic Optical Telescope

The Nordic Optical Telescope (NOT) is a 2.56 m Cassegrain telescope situated in La Palma, Canaries. It is equipped with the SOFIN (SOviet FINish) échelle spectrograph. SOFIN was designed and manufactured at the Crimean Astrophysical Observatory in collaboration with the Observatory of Helsinki University. First observations took place in June 1991. Depending on the aim of the observations and the brightness of the star, three different spectral resolutions are allowed: $R = \lambda/\Delta\lambda = 30000, 80000, 170000$.

The observations were recorded with a CCD camera having 2052×2052 pixels. Almost the all spectral range is covered by two échelle frames centered at 6427 Å and 7516 Å. For the observation of Sigma Geminorum, an entrance width of 65 μm, corresponding to an angle of about 0.5″ on the sky, was set. The spectral resolution in this case is $\lambda/\Delta\lambda = 83000$. The dispersion at 6170 Å was 37 mÅ/pix. The temperature of the camera

during observations was about 150 K and a S/N ratio of about 240 was achieved for most of the spectra. Observations were done by I. Ilyin and I. Tuominen.

3.2.2   Telescope Bernard Lyot

The MuSiCoS échelle spectrograph was constructed in 1990/1991 and is installed on the 2 m Foyer Cassegrain Télescope Bernard Lyot at Pic du Midi, France. The spectrograph covers most of the visible domain in 2 exposures (the blue domain ranging from 380 to 540 nm and the red domain $540 - 870$ nm) with a resolving power of 35000.

The observations were recorded with a 1024×1024 CCD camera. The 50 micron slit corresponds to 2.1 arcsec on the sky. Each observation of Sigma Geminorum had a total exposure time of 1440.0 s (360.0 s + 360.0 s + 360.0 s + 360.0 s). The mean S/N ratio varies from one year of observations to the other. For 1998, it was about 550, for 2000 about 480 and for 2001 about 590.

3.2.3   Data description

Sigma Geminorum was observed during four different epochs: December 2000 with NOT (observations by I. Ilyin and I. Tuominen) and February 1998, February 2000 and December 2001 with TBL (observations by The MuSiCoS collaboration). This allows us to compose 4 independent sets of observations covering the full rotational periods of the star. Exact dates and times of observation, the Julian date, the rotational phases and the S/N ratios of all 4 sets are given in Tables $3.3 - 3.6$.

Number	Date	Time	JD (2450000+)	Phase	S/N
1	04 Feb.	$23^h : 45' : 50''$	849.4902	0.7747	760
2	05 Feb.	$01^h : 14' : 21''$	850.5516	0.8288	630
3	06 Feb.	$23^h : 05' : 59''$	851.4625	0.8753	570
4	07 Feb.	$23^h : 28' : 55''$	852.4784	0.9271	510
5	09 Feb.	$21^h : 50' : 48''$	854.4103	0.0257	700
6	11 Feb.	$21^h : 01' : 33''$	856.3761	0.1259	770
7	12 Feb.	$22^h : 52' : 12''$	857.4529	0.1809	770
8	13 Feb.	$21^h : 05' : 06''$	858.3785	0.2281	560
9	14 Feb.	$21^h : 07' : 10''$	859.3800	0.2792	570
10	15 Feb.	$23^h : 04' : 59''$	860.4618	0.3343	370
11	16 Feb.	$23^h : 05' : 06''$	861.5035	0.3875	170
12	17 Feb.	$23^h : 46' : 17''$	862.4905	0.4378	550
13	18 Feb.	$21^h : 02' : 52''$	863.3770	0.4831	570
14	19 Feb.	$21^h : 36' : 38''$	864.4004	0.5353	440
15	20 Feb.	$22^h : 36' : 45''$	865.4422	0.5884	630

Table 3.3: List of observational parameters for February 1998 (TBL).

Rotational phases were calculated with an orbital period $P_{orb} = 19.60447$ days (Duemmler et al. 1997) and a zero-phase, $P_0 = 2\,450\,388.36853$, taken from Kovári et al. (2001). The rotational phase, E, can be calculated with the following equation:

Number	Date	Time	JD (2451000+)	Phase	S/N
1	02 Feb.	$01^h : 32' : 22''$	577.5641	0.9129	440
2	03 Feb.	$23^h : 36' : 50''$	578.4839	0.9598	410
3	05 Feb.	$20^h : 07' : 20''$	580.3384	0.0544	300
4	09 Feb.	$20^h : 40' : 02''$	584.3611	0.2596	520
5	12 Feb.	$23^h : 56' : 07''$	587.4973	0.4195	500
6	21 Feb.	$23^h : 45' : 40''$	596.4900	0.8783	520
7	22 Feb.	$23^h : 21' : 36''$	597.4733	0.9284	590
8	24 Feb.	$22^h : 42' : 15''$	599.4460	0.0290	450
9	25 Feb.	$22^h : 35' : 50''$	600.4415	0.0798	480
10	26 Feb.	$23^h : 40' : 55''$	601.4867	0.1331	470
11	27 Feb.	$22^h : 50' : 58''$	602.4521	0.1824	480
12	28 Feb.	$23^h : 25' : 30''$	603.4760	0.2346	550
13	29 Feb.	$19^h : 58' : 58''$	604.3326	0.2783	250
14	02 Mar.	$22^h : 44' : 56''$	606.4479	0.3862	490
15	04 Mar.	$23^h : 04' : 21''$	608.4614	0.4889	530
16	05 Mar.	$23^h : 57' : 35''$	609.7483	0.5545	550
17	07 Mar.	$22^h : 39' : 08''$	611.4438	0.6410	580
18	08 Mar.	$23^h : 13' : 31''$	612.4677	0.6933	620

Table 3.4: List of observational parameters for February - March 2000 (TBL).

Number	Date	Time	JD (2451000+)	Phase	S/N
1	07 Nov.	$06^h : 28' : 32''$	855.7698	0.8504	144
2	07 Nov.	$06^h : 52' : 43''$	855.7866	0.8513	162
3	08 Nov.	$06^h : 18' : 35''$	856.7629	0.9011	214
4	08 Nov.	$06^h : 42' : 02''$	856.7792	0.9020	208
5	09 Nov.	$06^h : 35' : 28''$	857.7746	0.9527	216
6	09 Nov.	$07^h : 07' : 59''$	857.7972	0.9539	225
7	13 Nov.	$04^h : 32' : 21''$	861.6891	0.1524	214
8	13 Nov.	$05^h : 07' : 38''$	861.7136	0.1537	244
9	14 Nov.	$05^h : 43' : 16''$	862.7384	0.2060	285
10	14 Nov.	$06^h : 16' : 42''$	862.7616	0.2071	298
11	15 Nov.	$06^h : 06' : 40''$	863.7546	0.2578	265
12	15 Nov.	$06^h : 39' : 23''$	863.7774	0.2589	248
13	09 Dec.	$02^h : 43' : 22''$	887.6134	0.4749	223
14	10 Dec.	$01^h : 36' : 22''$	888.5669	0.5235	245
15	11 Dec.	$02^h : 42' : 11''$	889.6126	0.5769	229
16	12 Dec.	$02^h : 43' : 04''$	890.6137	0.6279	294
17	13 Dec.	$02^h : 08' : 33''$	891.5893	0.6777	201
18	14 Dec.	$02^h : 21' : 51''$	892.5985	0.7292	260
19	15 Dec.	$02^h : 29' : 32''$	893.6038	0.7805	289

Table 3.5: List of observational parameters for November - December 2000 (NOT).

Number	Date	Time	JD (2452000+)	Phase	S/N
1	01 Dec.	$02^h : 44' : 17''$	245.6141	0.9893	450
2	02 Dec.	$02^h : 03' : 20''$	246.5856	0.0388	490
3	05 Dec.	$00^h : 55' : 06''$	249.5383	0.1894	400
4	06 Dec.	$01^h : 18' : 56''$	250.5548	0.2413	580
5	07 Dec.	$02^h : 47' : 35''$	251.6164	0.2954	520
6	08 Dec.	$02^h : 31' : 47''$	252.6054	0.3459	510
7	09 Dec.	$02^h : 37' : 59''$	253.6097	0.3971	520
8	10 Dec.	$02^h : 41' : 15''$	254.6120	0.4482	580
9	11 Dec.	$01^h : 40' : 42''$	255.5699	0.4971	530
10	12 Dec.	$02^h : 05' : 40''$	256.5873	0.5490	640
11	13 Dec.	$01^h : 26' : 38''$	257.5602	0.5986	500
12	15 Dec.	$02^h : 02' : 01''$	259.5847	0.7019	460
13	16 Dec.	$02^h : 05' : 11''$	260.5869	0.7530	590
14	17 Dec.	$01^h : 50' : 29''$	261.5767	0.8035	640
15	18 Dec.	$02^h : 04' : 27''$	262.5864	0.8550	610
16	27 Dec.	$00^h : 55' : 47''$	271.5387	0.3116	530
17	05 Jan.	$01^h : 19' : 03''$	280.5549	0.7715	530
18	06 Jan.	$00^h : 48' : 53''$	281.5339	0.8215	530

Table 3.6: List of observational parameters for December 2001 - January 2002 (TBL).

$$E = \frac{HJD - P_0}{P_{orb}}, \qquad (3.2)$$

where HJD is the heliocentric Julian date of the observation.

In total 70 spectra are available for Doppler Imaging: 15 from February 1998, 18 from February – March 2000, 19 from November – December 2000 and 18 from December 2001 – January 2002. Example of one set of observations consisting of 15 spectra from February 1998, which are cover a full rotational period, is shown in Fig. 3.2. Some of the observed lines show clear distortions and changes from one rotational phase to the next. Only a short section of full spectrum with 4 atomic lines which were used for Doppler Imaging is shown.

The lines chosen for Doppler Imaging in case of the observations from TBL are Fe I 6173 Å, Ni I 6175 Å, Ni I 6177 Å, Fe I 6180 Å(Fig. 3.3) and Fe I 6430 Å, Ca I 6439 Å (Fig. 3.4). The wavelength interval in the reduced data files kindly provided by I. Ilyin for observations from NOT is 6158 – 6199 Å. Thus we can use only 4 lines (Fe I 6173 Å, Ni I 6175 Å, Ni I 6177 Å, Fe I 6180 Å) for the analysis.

In order to see the evolution of spots one needs to compare the same places on the star observed at different epochs, e.g. in different years. In order to see whether there is any change in the spectral line profiles between different years we compare approximately the same rotational phase (the difference between maximal and minimal phases is 0.0222) observed at different epochs (Fig. 3.5).
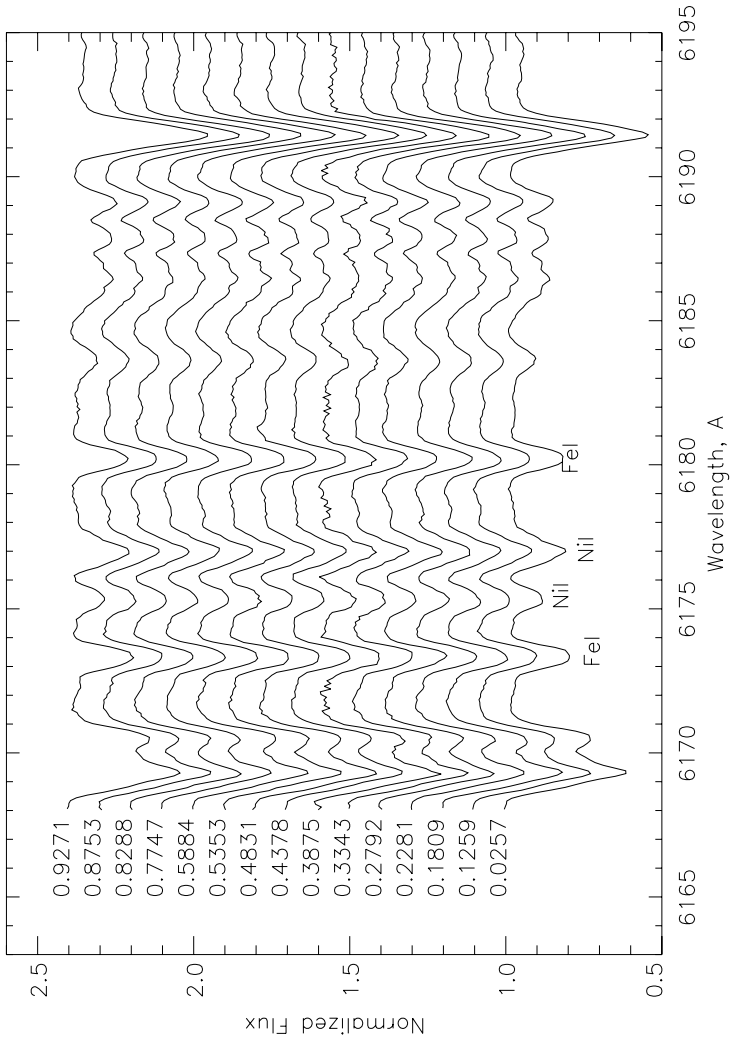
Figure 3.2: Set of 15 spectra recorded with TBL in February 1998. Line profiles of consecutive phases have been shifted in the vertical direction. The corresponding phases are given on the left side. Four lines that are analysed in detail are identified.
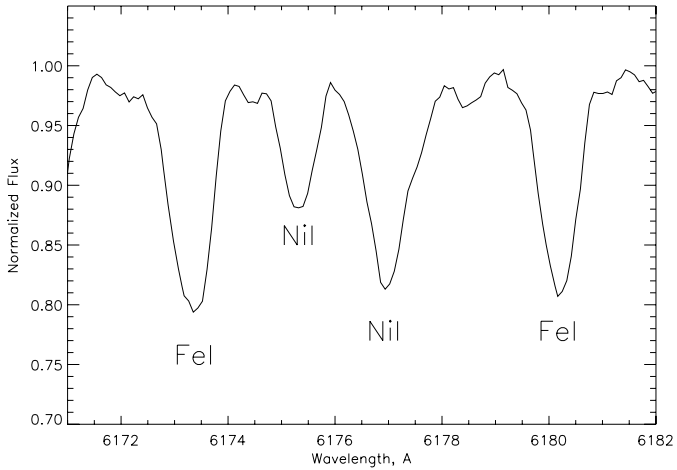
Figure 3.3: Atomic lines used for Doppler Imaging: Fe I 6173 Å, Ni I 6175 Å, Ni I 6177 Å and Fe I 6180 Å (observations from 06.01.2001, TBL).
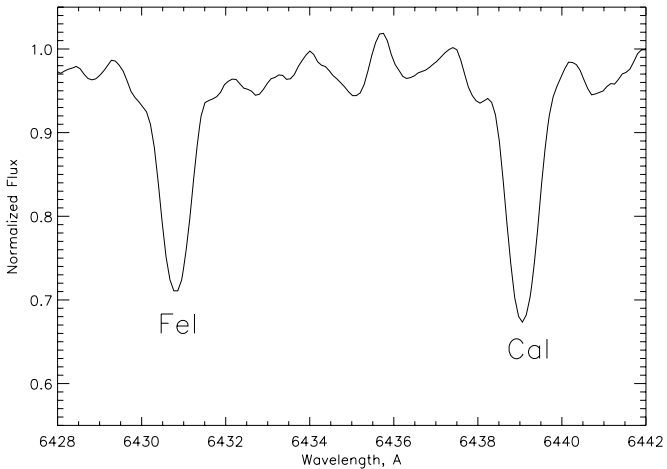

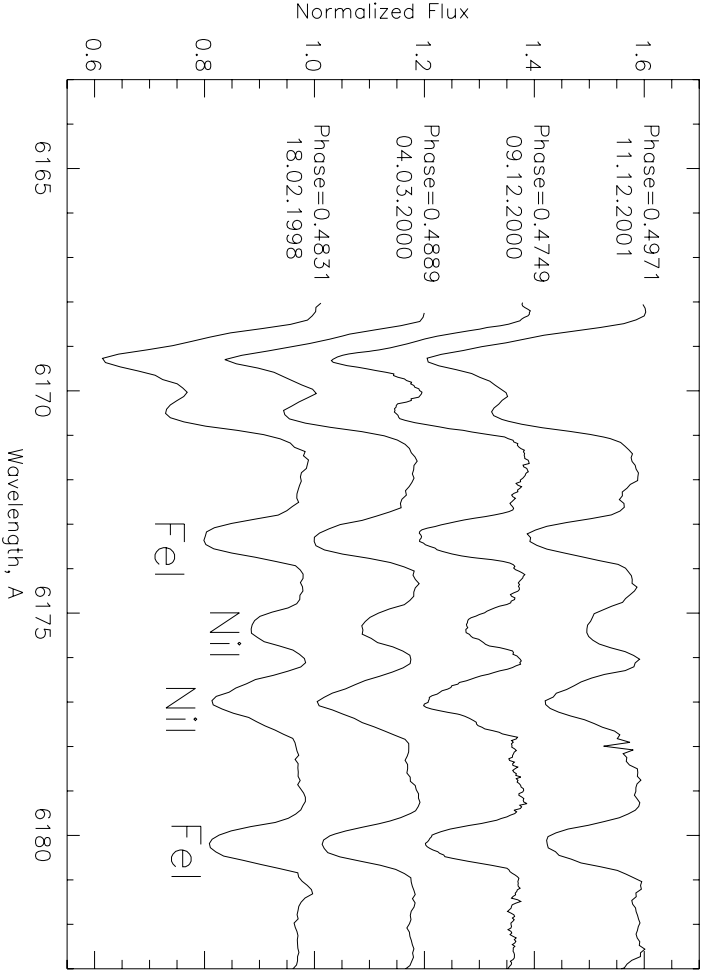Figure 3.4: Atomic lines used for Doppler Imaging: Fe I 6430 Å and Ca I 6439 Å(observations from 06.01.2001, TBL).

31

Figure 3.5: 4 spectra taken approximately at the same rotational phase, but at different epochs. Phase 0.4831 from February 1998, phase 0.4889 from March 2000, phase 0.4749 from December 2000 and phase 0.4971 from December 2001.

3.3 Studying of the physical parameters of σ Geminorum

The choice of values of stellar parameters has a big influence on the quality of a reconstructed map of the star Vogt et al. (1987), Rice et al. (1989), Piskunov et al. (1990) and (Unruh 1996). In order to reconstruct a picture which is free from any artificial features all parameters have to be known with a high precision. The big variations in values of the parameters determined by different authors presented in Sec. $3.1.1 - 3.1.2$ show that this is not the case for Sigma Geminorum. Thus, first of all we need to analyse all physical parameters necessary for the reconstruction by varying them within the range of values other authors have determined.

In order to select the best suitable set of parameters we made several reconstructions varying each parameter within the known range with a step individually adopted for every parameter. The value which gives the best fit of the calculated spectra to the observed ones is taken for the final run. As a quantitative characteristic of the agreement between calculations and observations we used the standard deviations (Δ) between the two spectra at the wavelengths of those lines which we used for the inversion. The standard deviation (Δ) is:

$$\Delta = \sqrt{\frac{1}{n} \sum_{i=1}^{n} (I_{calc} - I_{obs})^2}, \qquad (3.3)$$

where $I_{calc} - I_{obs}$ is the difference between the calculated and observed spectra and n is the number of calculated points. If the difference between the two compared spectra is small, then the standard deviation will be low (closer to zero). If the data points are highly variable, then the standard deviation is high (further from zero). Thus, we are searching for the solution with the minimal Δ.

In order to find the best set of parameters I took the set of observations (18 phases) from December 2001 taken at the TBL. The following 6 atomic lines: Fe I 6173 Å, Ni I 6175 Å, Ni I 6177 Å, Fe I 6180 Å, Fe I 6430 Å and Ca I 6439 Å were analysed.

The first approximation of the astrophysical parameters and their ranges were taken from the paper of (Kovári et al. 2001). They are given in Table 3.7.

Parameter	Value	'Standard' model
$\log g$	$2.5^{+0.23}_{-0.42}$	2.5
Macroturbulence, ζ	3.0 km s^{-1}	3.0
Microturbulence for Ca, ξ_{Ca}	0.7 km s^{-1}	0.7
Microturbulence for Fe, ξ_{Fe}	1.0 km s^{-1}	-
T_{eff}	4630 ± 100 K	4630
Inclination, i	$60° \pm 15°$	60
$v \sin i$	27.5 ± 1 km s^{-1}	26.7

Table 3.7: Astrophysical parameters of Sigma Geminorum found by Kovári et al. (2001) and used in this work as a 'standard' model

Detailed study of the parameters listed in Table 3.7 is presented in the next 5 subsections.

3.3.1   Surface gravity

The surface gravity obtained by the standard analysis of a stellar spectrum is the effective gravity $g = GM/R^2$, where G is the universal gravitational constant, M and R are stellar mass and radius respectively. The surface gravity relates to the gas pressure of a star according to the equation $P_{gas} \approx constant \cdot g^p$, where the power p depends on the optical depth and varies in the range from 0.64 for deep layers to 0.57 for shallow layers. The gas pressure P_{gas} increases at all optical depths with increasing surface gravity.

One of the important indicators of surface gravity is the size of Doppler broadening. The line wings become broader with higher g, but the physical mechanism for this is still not well understood. The difference in spectral line profiles calculated with 3 different $\log g$ is presented in Fig. 3.6. The plotted spectral lines are not normalized to the continuum level. Thus in case we do it, the depth of the spectral line will be changed.
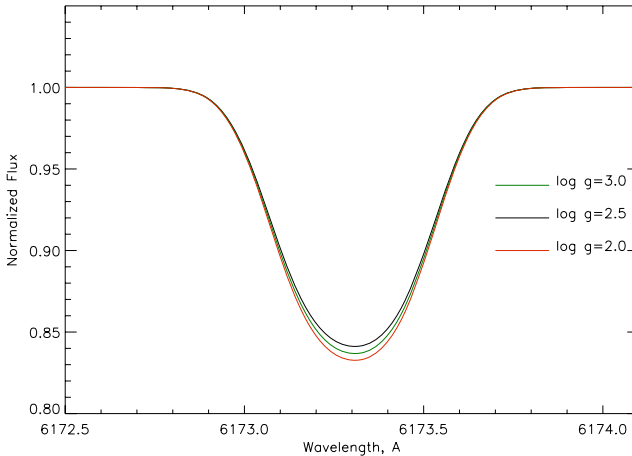
Figure 3.6: Spectral line profiles of Fe I (6173.33Å) line calculated with $v \sin i = 27.5$ km/s calculated with 3 different $\log g$. The red line represents the line profile calculated with $\log g = 2.0$, the black line — with $\log g = 2.5$ and the green line — with $\log g = 3.0$

As seen from table 3.7, the value of $\log g$ for Sigma Geminorum is lying within the range from 2.08 to 2.73. Synthetic line profiles are calculated using the stellar atmosphere models by Kurucz (1993) for a given temperature range and gravity. The grid of models cover the gravity range from $\log g = 0.0$ to +5.0 in steps of +0.5. Thus we can calculate synthetic line profiles only for the following values: 2.0, 2.5, 3.0. Resulting spectra calculated with these 3 different $\log g$ are presented in Figs. 3.7 — 3.12. Fits to the data are plotted in Figs. 3.7, 3.8, 3.9: the observed and calculated line profiles are shown by plus signs and lines, respectively. Profiles for consecutive phases have been shifted in the vertical direction such that the earliest phase is on the bottom and the latest one is on

the top of the graph. Surface maps of σ Gem for the 3 different values of log g in the scale of effective temperatures are shown in four orbital phases and pole-on projections with a coordinate grid of 30° in both latitude and longitude in Figs. 3.10, 3.11, 3.12. Note that unless stated explicitly, other parameters are as listed in Table 3.7 under 'standard' model.

Standard deviations between theoretical spectra calculated with different log g and the observed spectra are following:

log g	Δ
2.0	0.00148
2.5	0.00119
3.0	0.00131

Thus the best value of log g is 2.5 (Fig. 3.10), which is not surprising since this is also the most probable value obtained from independent observations (Kővári et al.; see Table 3.7)). Note that the positions of spots on the maps of Sigma Geminorum calculated with log g = 2.0 (Fig. 3.11) and 2.5 are the same, but the lower value of log g gives a more noisy picture. The map with log g = 3.0 (Fig. 3.12) differs significantly from the two previous pictures. Spots form now a strong dark belt close to the poles. Therefore in the subsequent calculations the value log g = 2.5 will be used.
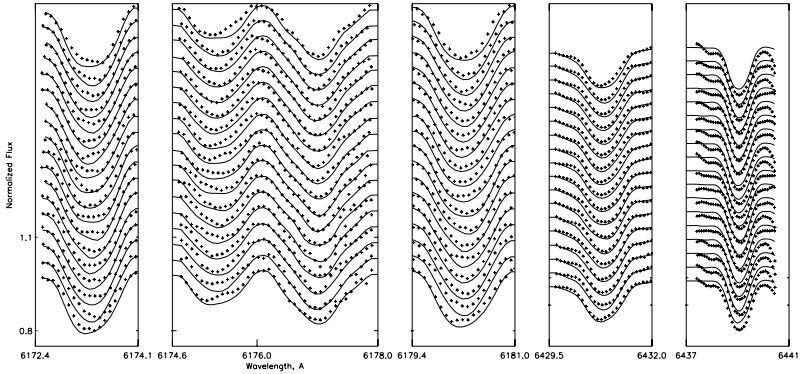
Figure 3.7: A fit to the observations calculated with log g = 2.0. The observed and calculated line profiles are shown by plus signs and lines, respectively. Profiles for consecutive phases have been shifted in the vertical direction such that the earliest phase is on the bottom and the latest one is on the top. The 5 panels are for the lines (left to right): Fe I 6173 Å, Ni I 6175 Å and Ni I 6177 Å, Fe I 6180 Å, Fe I 6430 Å and Ca I 6439 Å .
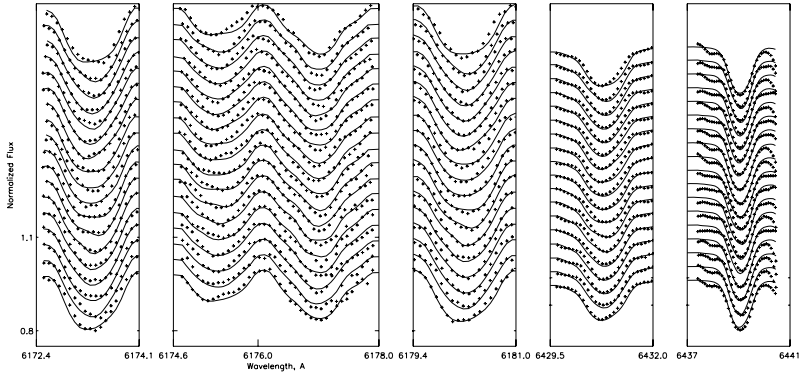
Figure 3.8: Same as Fig. 3.7 but with $\log g = 2.5$, $\xi = 0.7$ km/s, $\zeta = 3.0$ km/s.
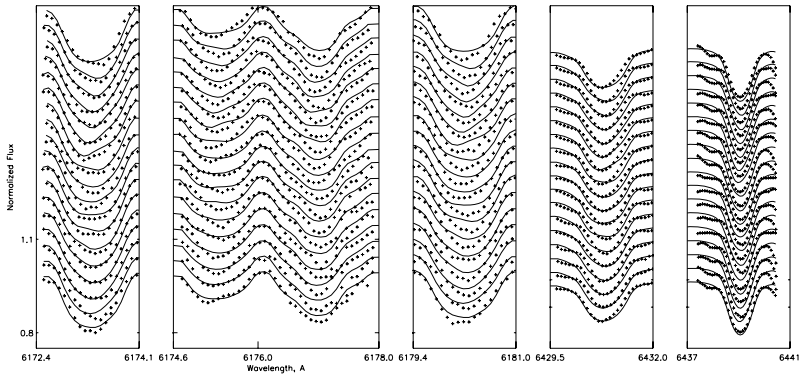
Figure 3.9: Same as Fig. 3.7 but with $\log g = 3.0$.

3.3.2 Turbulent motions: microturbulence and macroturbulence

Doppler shifts appear even for stars with small rotational broadening, due to the motions of the gas in the photospheres of stars. This kind of line broadening mechanism is suprathermal. The motion of gases in the photosphere of a star was discovered in early stellar spectroscopic study and was called "turbulence" ((Rosseland 1928)). Turbulent motions are usually divided into two types: microturbulence and macroturbulence. When we deal with the turbulent cells which have element sizes that are smaller compared to the

mean free path of a photon, that is a *microturbulent motion* . If the size of the turbulent elements is small compared to unit optical depth then we have microturbulence. When the turbulent cells are so large that photons stay in them from the creation until they leave the star, that is a case of a *macroturbulent motion*. Thus if the size of the turbulent elements is large compared to the unit optical depth it is macroturbulence. In case of an unresolved star we view all macrocells at the same moment. Each of this cells gives a complete spectrum with the corresponding to its velocity Doppler Shift. In this case we can say that the macroturbulence influences the line profiles similar to rotation.

Comparison of the synthetic atomic lines with those calculated with 3 different values of microturbulence, ξ, and 3 different values of macroturbulence, ζ, is presented in Figs. 3.13 and 3.14 respectively.

In Table 3.7 two values for microturbulence are given: microturbulence for Ca, $\xi_{Ca} = 0.7$ km/s and microturbulence for Fe, $\xi_{Fe} = 1.0$ km/s. In order to find the best value for microturbulence, I made 5 calculations for $\xi = 0.6, 0.7, 0.8, 0.9$ and 1.0 km/s. Standard deviations between the theoretical spectra calculated with different microturbulence and the observed spectra are the following:

ξ, km/s	Δ
0.6	0.00137
0.7	0.00119
0.8	0.00120
0.9	0.00126
1.0	0.00129

The minimal standard deviation corresponds to the microturbulence for Ca, $\xi_{Ca} = 0.7$. Calculated spectra compared to the observed ones as well as stellar surfaces reconstructed for 2 different values of microturbulence are shown on the Figs. 3.8, 3.11 and 3.15, 3.16. Fits to the simulations are plotted in Figs. 3.8 and 3.16. The corresponding surface maps of σ Gem in the scale of effective temperatures are shown in four orbital phases and pole-on projections with a coordinate grid of 30° in both latitude and longitude in Figs. 3.11 and 3.15.

The difference between maps reconstructed with $\xi = 0.7$ (Fig. 3.11) and $\xi = 1.0$ (Fig. 3.16) is almost negligible. This means that the value of the microturbulence does not play an important role in the reconstruction of stellar surfaces. For later calculations I used a microturbulence equal to 0.7 km/s.

The value of macroturbulence, ζ, is accurately known and equal to 3.0. I used that value for my calculations (Fig. 3.8, 3.11). In fact, different macroturbulences do not influence much on the final result also. I made two test calculations for $\zeta = 2.5$ and $\zeta = 3.5$ to check this. Stellar surface maps reconstructed with different macroturbulences are present on the Fig. 3.17 and 3.18.
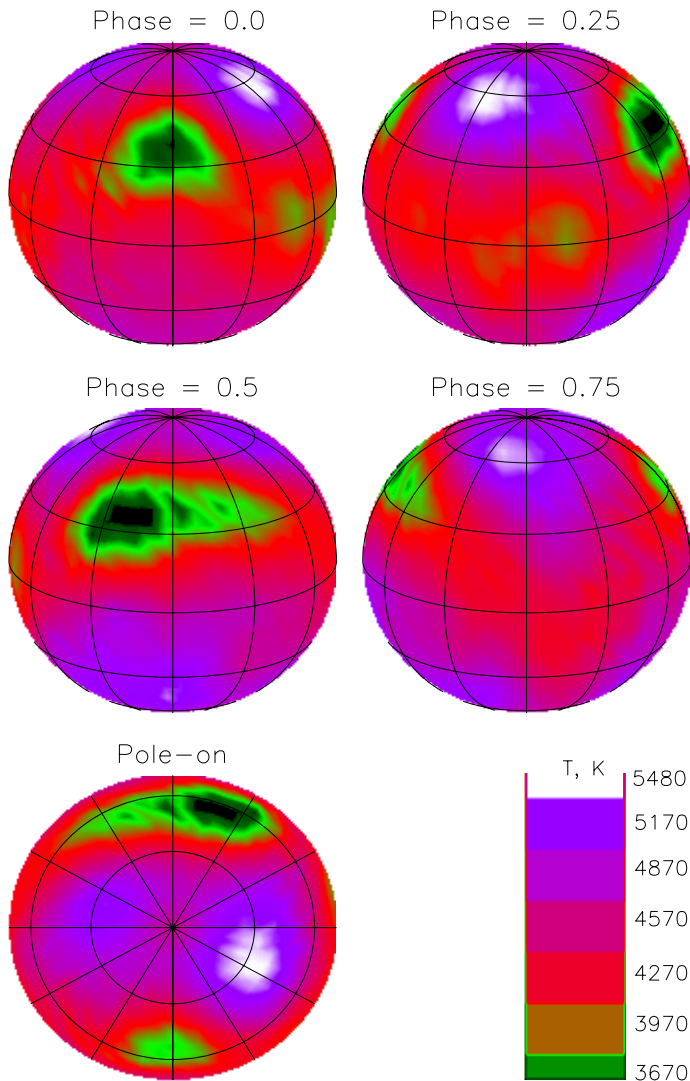
Figure 3.10: Reconstructed surface map of σ Gem for $\log g = 2.0$ is shown in four orbital phases with a coordinate grid of 30° in both latitude and longitude. Plotted is the effective temperature distribution given by the colour scale, which is clarified by the bottom right panel.
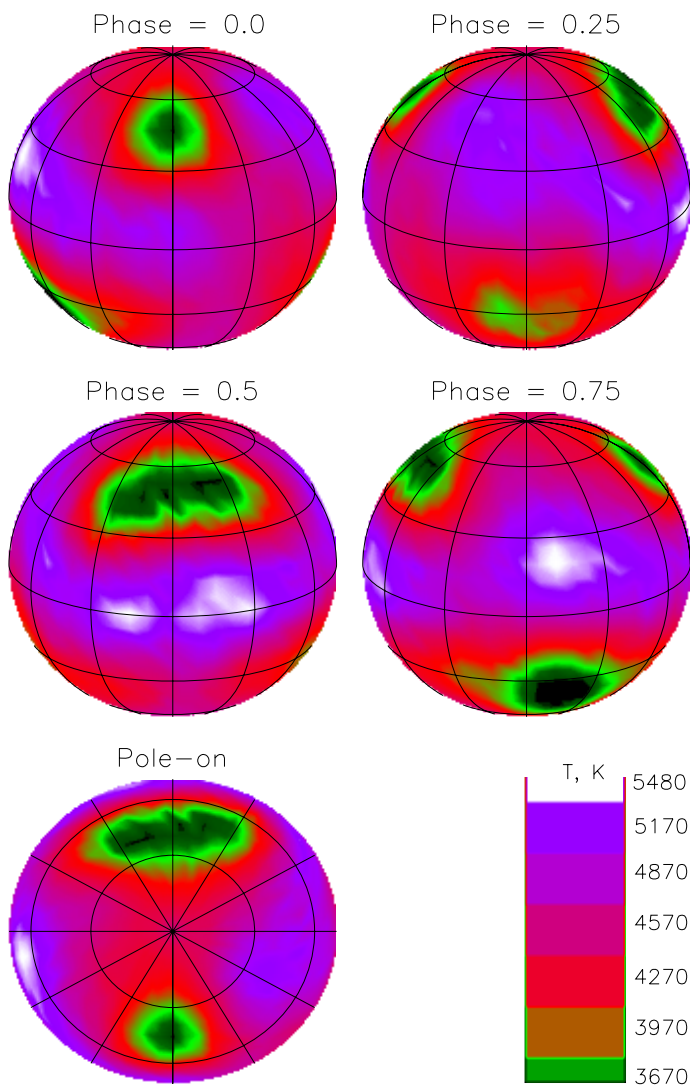
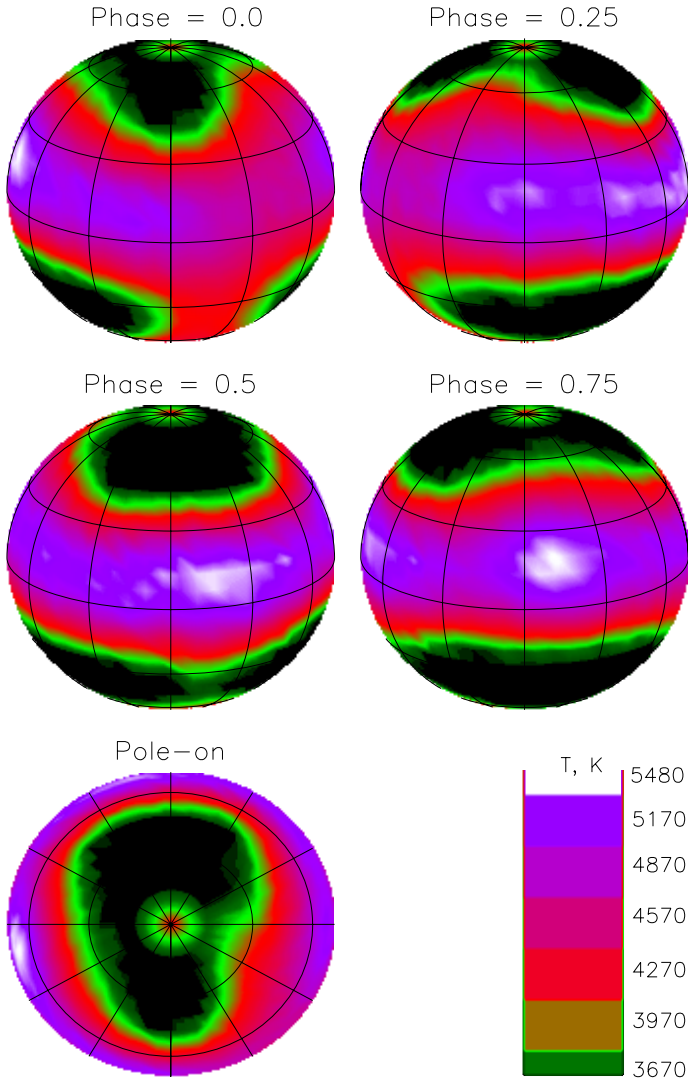Figure 3.11: Same as Fig. 3.10 but for log g = 2.5, ξ = 0.7 km/s, ζ = 3.0 km/s
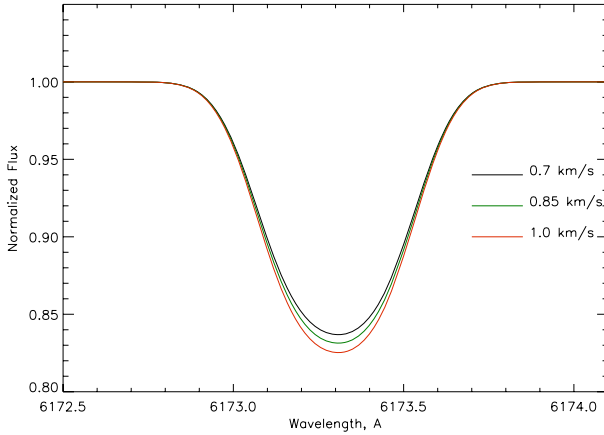
Figure 3.12: Same as Fig. 3.10 but for log g = 3.0.

Figure 3.13: Spectral line profiles of Fe I (6173.33Å) line calculated with $v \sin i = 27.5$ km/s calculated with 3 different values of the microturbulence. The red line represents the line profile calculated with $\xi = 1.0$ km/s, the green line with $\xi = 0.85$ km/s and the black line with $\xi = 0.7$ km/s
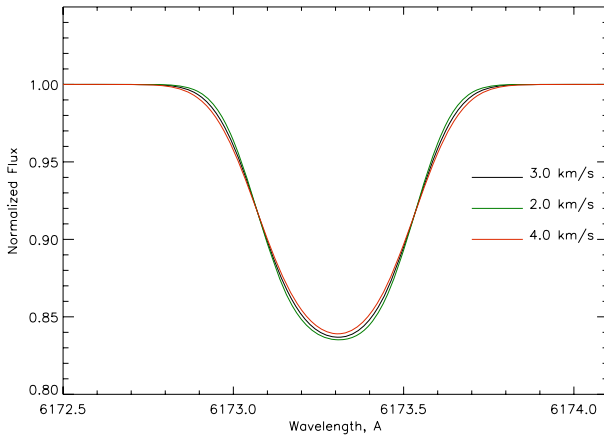
Figure 3.14: Spectral line profiles of Fe I (6173.33Å) line calculated with $v \sin i = 27.5$ km/s and 3 different values of the macroturbulence. The red line represents the line profile calculated with $\zeta = 4.0$ km/s, the green line with $\zeta = 2.0$ km/s and the black line with $\zeta = 3.0$ km/s
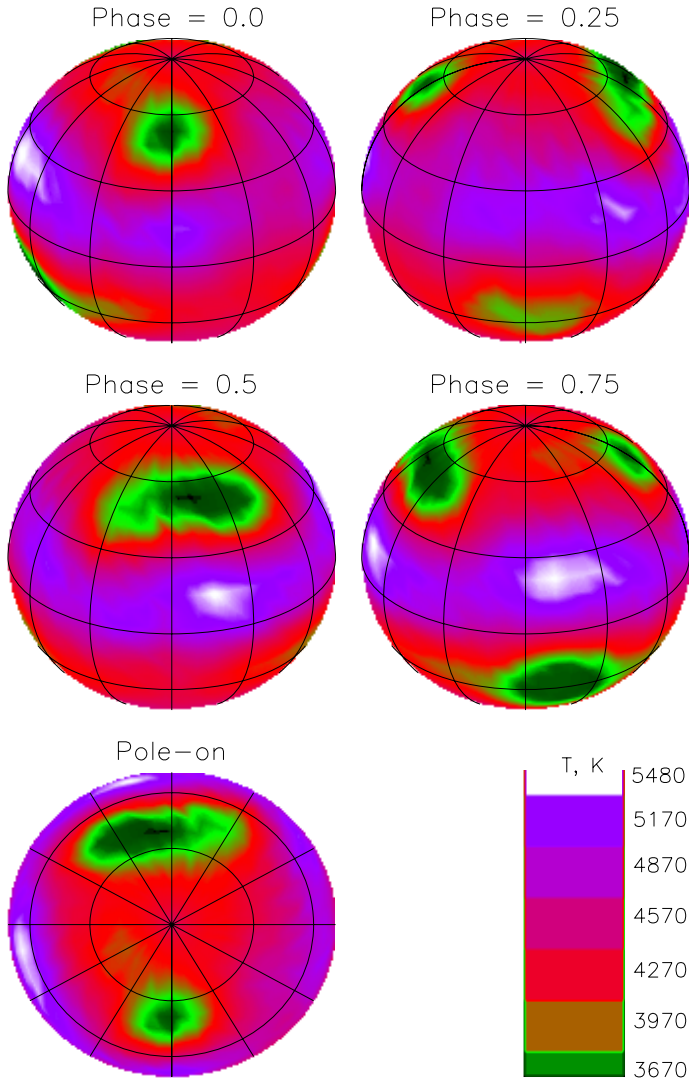
Figure 3.15: Reconstructed surface map of σ Gem for $\xi = 1.0$ km/s is shown in four orbital phases with a coordinate grid of 30° in both latitude and longitude. Plotted is the effective temperature distribution given by the colour scale, which is clarified by the bottom right panel.
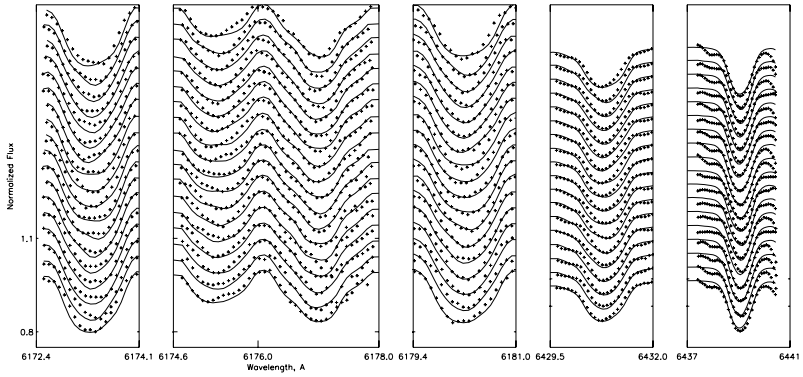
Figure 3.16: A fit to the observations calculated with $\xi = 1.0$ km/s. The observed and calculated line profiles are shown by pluses and lines, respectively.
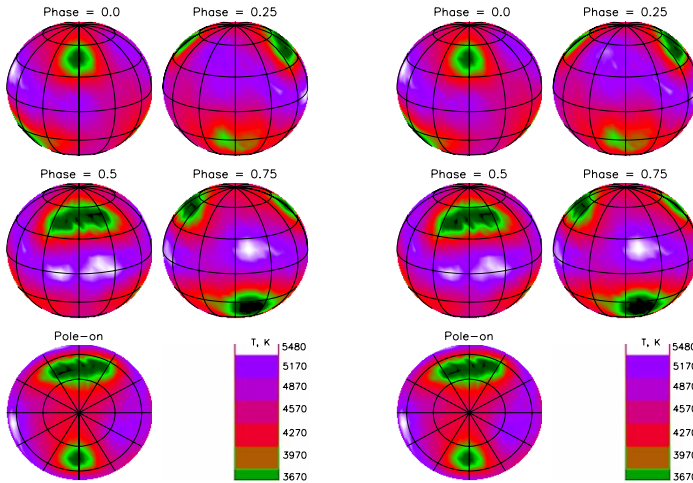
Figure 3.17: Reconstructed surface map of σ Gem for $\zeta = 0.25$ km/s in the scale of effective temperatures is shown in four orbital phases with a coordinate grid of 30° in both latitude and longitude.

Figure 3.18: Reconstructed surface map of σ Gem for $\zeta = 0.35$ km/s in the scale of effective temperatures is shown in four orbital phases with a coordinate grid of 30° in both latitude and longitude.

3.3.3 Effective temperature

The line strength is a function of three main parameters: temperature, electron pressure (or $\log g$, see Sec. 3.3.1) and atomic constants. Effective temperature is thus one of the most important variables which controls the line strength or equivalent width of a spectral line.

Effective temperature, T_{eff}, can be described in terms of the total flux per unit area radiated by the star Gray (1992):

$$\int_0^\infty \tilde{F}_\nu \, d\nu = \sigma T_{eff}^4 \,, \tag{3.4}$$

where $\tilde{F}_\nu$ is the flux emitted from the stellar surface and $\sigma = 5.67 \times 10^{-5}$ erg/(s cm^{2}deg^4). To determine the effective temperature from the absolute flux F_ν measured at the earth in practice, an integration over the frequency is needed:

$$\int_0^\infty F_\nu d\nu = (R/r)^2 \sigma T_{eff}^4 \,, \tag{3.5}$$

where R is the radius of a star and r is the distance to the star.

The strong influence of the temperature on the spectral line profiles comes from the equations of excitation-ionization processes (see Sec. 2.5.1). For example, the ratio of populations of atoms in two energy levels m and n, which is described by the excitation or so-called Boltzmann equation, depends exponentially on the temperature:

$$\frac{N_n}{N_m} = \frac{g_n}{g_m} \exp(-\frac{\Delta\chi}{kT}) \,, \tag{3.6}$$

where N_n and N_m are the numbers of excited atoms in a level n and m respectively, g_n and g_m are the statistical weights of the corresponding levels ($g = 2J + 1$ where J is the inner quantum number). $\Delta\chi = \chi_n - \chi_m$, where χ_i is the excitation potential of the i-th level (the excitation potential is the energy above the ground energy level).

The next process through which temperature influences the shape of spectral lines is ionization. To describe the degree of the ionization of the gas, the Saha equation is used. The ratio of ions to neutrals N_1/N_0 is:

$$P_e \frac{N_1}{N_0} = \frac{g_1}{g_0} \frac{2(2\pi mkT)^{3/2}}{h_3} \exp(-\frac{I}{kT}) \,, \tag{3.7}$$

where P_e is the number of free electrons per 1 cm^3, $\frac{g_1}{g_0}$ is the ratio of the statistical weights, m is the electron mass, h is Planck's constant and I is the ionization potential (the difference in energy between the ground level and the continuum).

Comparison of 3 synthetic spectral lines calculated with different effective temperatures is presented in Fig. 3.19. As an example for calculations I took the Fe I line (6173.33 Å). Profiles are calculated with the rotational velocity $v \sin i = 27.0$ km/s. Thus, the lines are broaded due to the rotation. As can be seen, a smaller effective temperature gives a deeper line. It is also possible to see that the equivalent width of lines is decreasing with the increasing temperature.
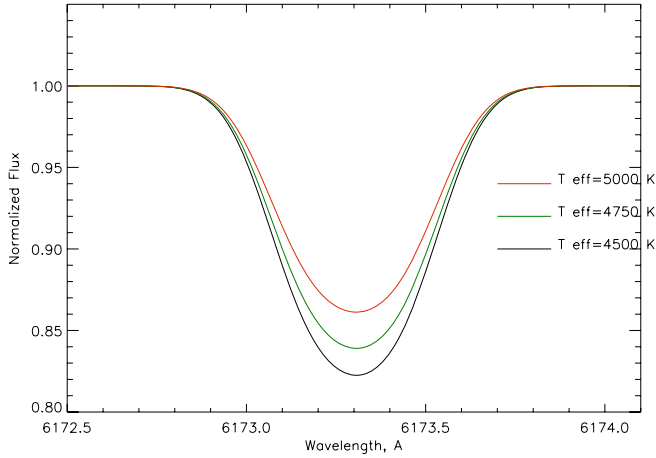
Figure 3.19: Spectral line profiles calculated with 3 different values of the effective temperature. The red line represented the line profile calculated with T_{eff} = 5000 K, the green line with T_{eff} = 4750 K and the black line with T_{eff} = 4500 K

To see how strong the influence of a wrongly chosen effective temperature on the reconstructed map could be, I made 2 test calculations with the effective temperatures which are 150 K out of the range of temperatures given in Table 3.7. Fits to the simulations are plotted in Fig. 3.20 for T_{eff} = 4380 K (standard deviation Δ = 0.00154) and in Fig. 3.21 for T_{eff} = 4880 K (standard deviation Δ = 0.00119). The corresponding surface maps of σ Gem in the scale of effective temperatures are shown in four orbital phases and pole-on projections with a coordinate grid of 30° in both latitude and longitude in Figs. 3.22 and 3.23. A wrong choice of the temperature results in different artificial features on a reconstructed stellar surface. The lower temperature (Fig. 3.22) causes a higher brightness of spots and a concentration of spots in a polar region. The map produced with a higher temperature (Fig. 3.23) has a less bright equatorial belt of spots.

In Table 3.7 the value of the effective temperature is given as 4630 ± 100 K. Standard deviations between the theoretical spectra and observations were calculated for 44 effective temperatures in the range between 4410 K and 4950 K. For the range between 4520 K and 4880 K a step of calculations is 10 K. Dependence of the standard deviation on the effective temperatures used for calculations is shown by the black line in Fig. 3.24, where each grid point where calculations are done is marked by a star. A non-linear least squares fit to the function Δ(T) gave a parabola (see blue line in Fig. 3.24) with the minimum standard deviation at about T_{eff} = 4750 K although this value is 20 K higher than the maximum number given by Kővári et al. (see Table 3.7), we will use it for later calculations, because it gives the minimum deviation of the calculated profiles from the observed once. The stellar surface map reconstructed with T_{eff} = 4750 K is
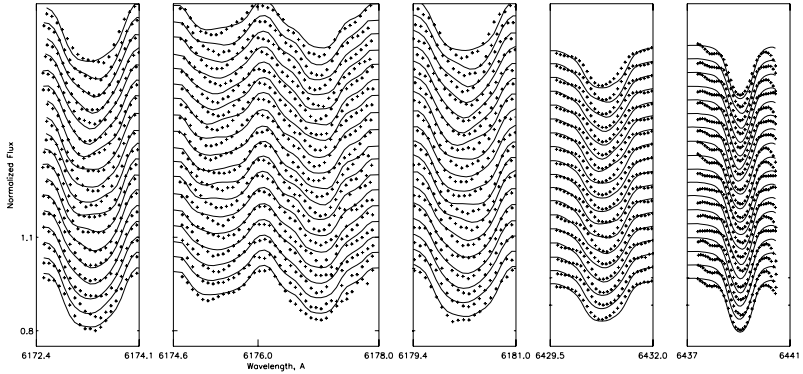
Figure 3.20: A fit calculated with T_{eff} = 4380 K to the observations. The observed and calculated line profiles are shown by pluses and lines, respectively.
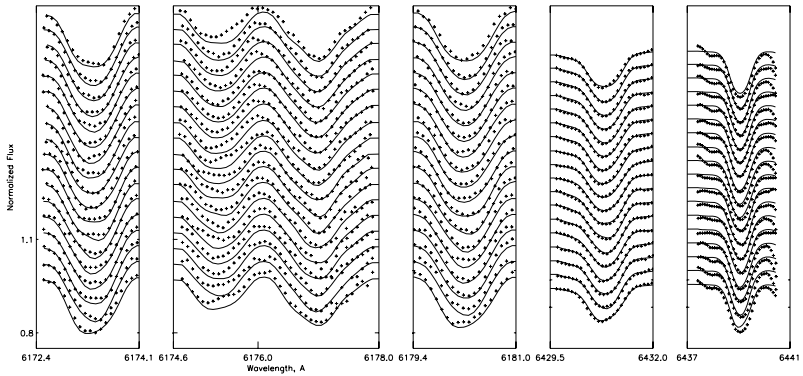

Figure 3.21: Same as Fig. 3.20 but with T_{eff} = 4880 K.

presented in Fig. 3.25 and fit to the observations is in Fig. 3.26. Calculations are done with $v \sin i$ = 26.7 km/s, inclination i = 60° and parameters, which were determined in the previous sections: $\log g$ = 2.5, ξ = 0.7 km/s, ζ = 3.0 km/s.
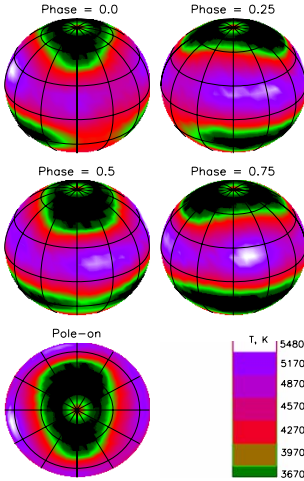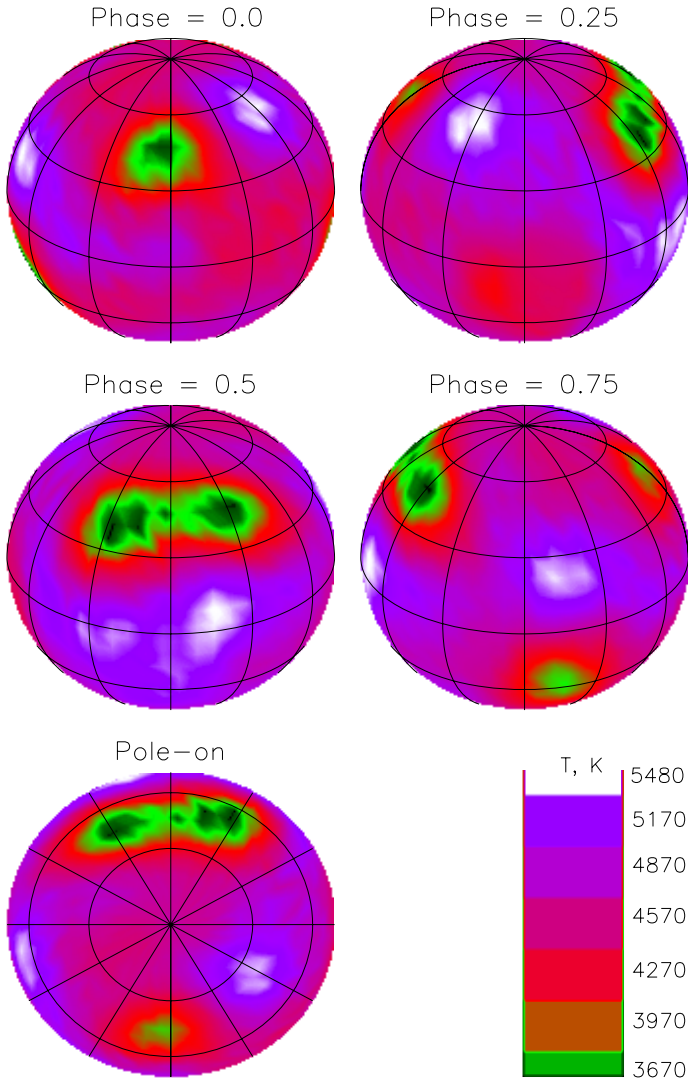
Figure 3.22: Reconstructed surface map of σ Gem for T_{eff} = 4380 K is shown in four orbital phases with a coordinate grid of 30° in both latitude and longitude. Plotted is the effective temperature distribution given by the colour scale, which is given by the bottom right panel.
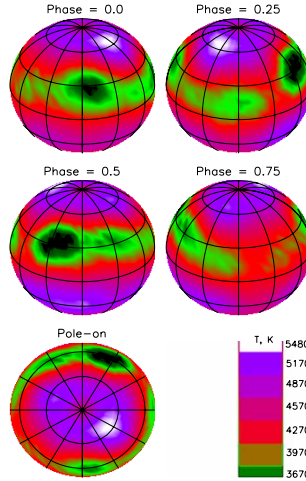
Figure 3.23: Reconstructed surface map of σ Gem for T_{eff} = 4880 K is shown in four orbital phases with a coordinate grid of 30° in both latitude and longitude. Plotted is the effective temperature distribution given by the colour scale, which is given by the bottom right panel.
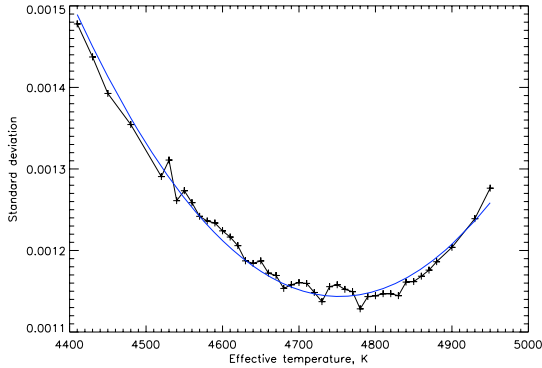
Figure 3.24: Dependence of the resulting standard deviation on the effective temperature (stars connected by black line) and fitted to it parabola (blue line).
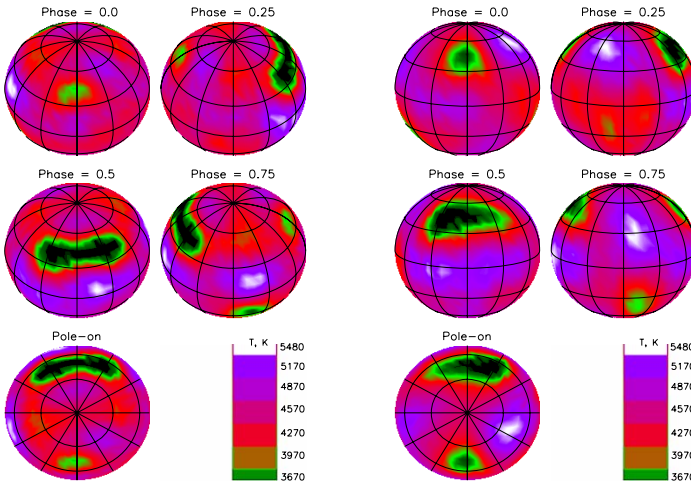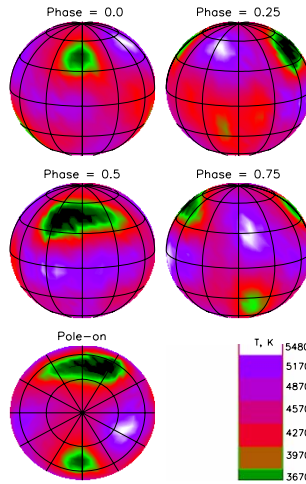
Figure 3.25: Same as Fig. 3.23 but with T_{eff} = 4750 K.
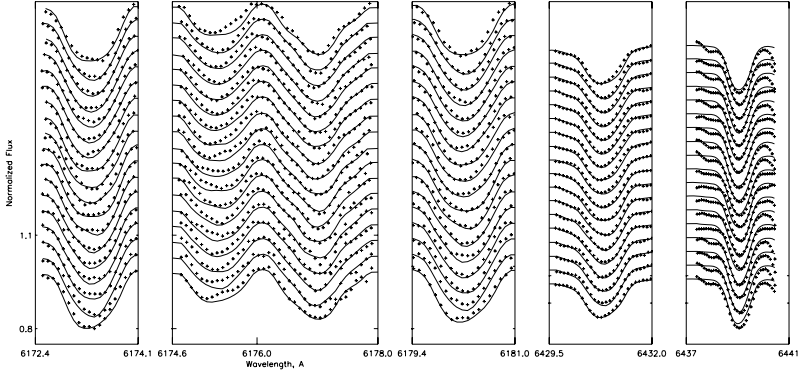
Figure 3.26: Same as Fig. 3.20 but with T_{eff} = 4750 K.

Figure 3.27: Reconstructed surface map of σ Gem for $i = 45°$ is shown in four orbital phases with a coordinate grid of 30° in both latitude and longitude. Plotted is the effective temperature distribution given by the colour scale, which is given by the bottom right panel.

Figure 3.28: Reconstructed surface map of σ Gem for $i = 75°$ is shown in four orbital phases with a coordinate grid of 30° in both latitude and longitude. Plotted is the effective temperature distribution given by the colour scale, which is given by the bottom right panel.

3.3.4   Inclination

Geometrical parameters which are important for the stellar surface reconstruction (i.e. the inclination, i, and the projected velocity, $v \sin i$) are described in the next 2 sections.

The inclination, i, is the angle between the normal to the orbital plane (i.e. the orbital axis) and the direction to the observer. Broadening due to the Doppler shift depends on this angle. Observed distortions in the spectral line profiles will reflect the inclination of the axis of rotation from the line of sight. There are some restrictions for the values of inclination for the stars which are candidates for Doppler Imaging: $20° < i < 70°$. For the detailed explanation see Sec. 2.3.

Inclination for Sigma Geminorum is known within the range between 45° and 75° (see Table 3.7). I calculated standard deviations for 9 values of inclination from 40° to 80° with a step of 5°. Dependence of the calculated Δ from the inclinations is plotted in Fig. 3.27. To demonstrate that the value of Δ does not change much with different inclinations, I plotted it in the same range of y-axis as in Fig. 3.29, where the dependence of standard deviations on the effective temperature is displayed. Thus, we conclude, that inclination within the determined range has almost no influence on the quality of the fit. It's an important result, because the inclination belongs to that group of parameters which are determined not very accurately.

The role of the inclination on the reconstruction is demonstrated by 2 maps calculated with boundary values of the inclination: $i = 45°$ in Fig. 3.27 and $i = 75°$ in Fig. 3.28. The corresponding fits to the observations are plotted in Fig. 3.30 for $i = 45°$ (standard deviation $\Delta = 0.001147$) and for $i = 75°$ in Fig. 3.31 ($\Delta = 0.001167$). Indeed, spots are at the same positions in both maps. The only difference in the reconstructed stellar surfaces is in the size of spots. This difference is not so big either even though the calculations were done with the difference in 30° in the inclination. The spots in the map calculated with $i = 75°$ (Fig. 3.28) are a bit bigger than in case of the smaller inclination (Fig. 3.27).
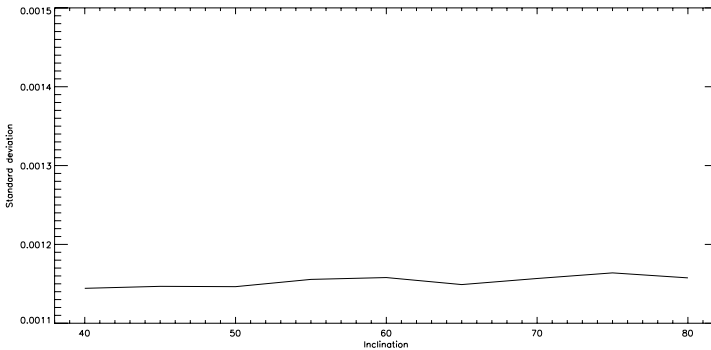

Figure 3.29: Dependence of the standard deviation on the inclination.

For further calculations I will use the inclination equal to 70°. The stellar surface map reconstructed with $i = 70°$ is presented in Fig. 3.32 and fit to the observations in Fig. 3.33.
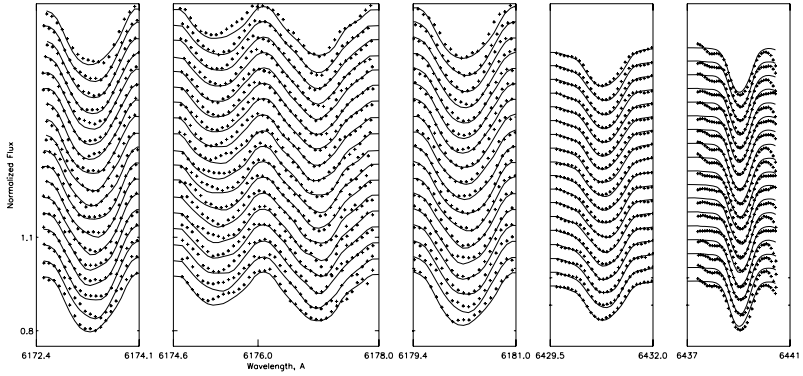
Figure 3.30: A fit to the observations calculated with $i = 45°$. The observed and calculated line profiles are shown by pluses and lines, respectively.

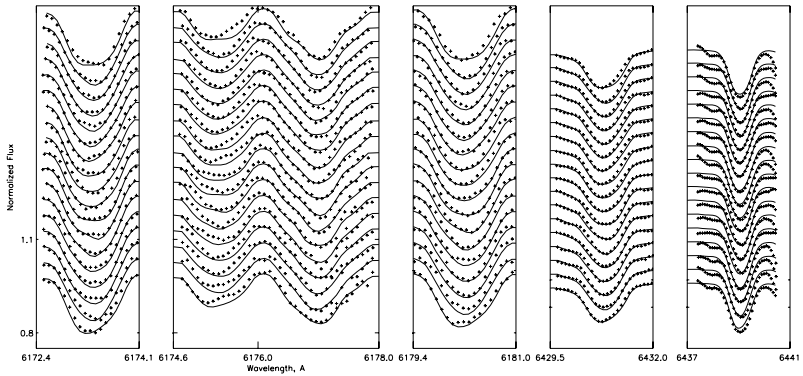Figure 3.31: Same as Fig. 3.30 but with $i = 75°$.

Calculations are done with $\log g = 2.5$, microturbulence $\xi = 0.7$ km/s, macroturbulence $\zeta = 3.0$ km/s, $T_{eff} = 4750$ K and $v \sin i = 26.7$ km/s which will be discussed later.
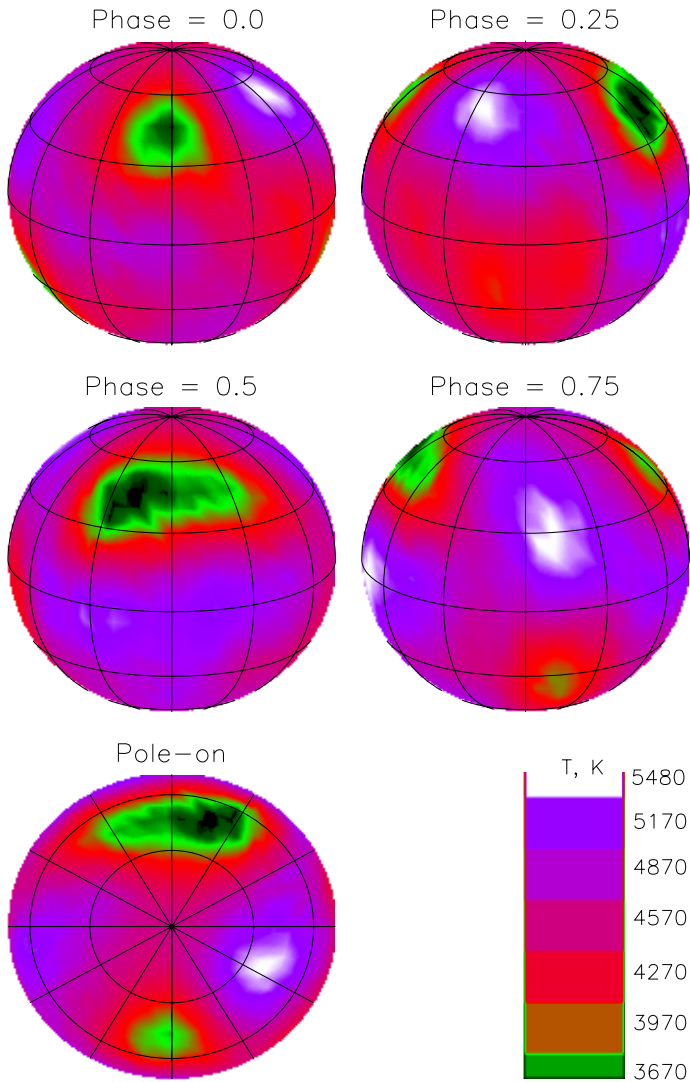
Phase = 0.0

Phase = 0.25

Phase = 0.5

Phase = 0.75

Pole−on

T, K

5480

5170

4870

4570

4270

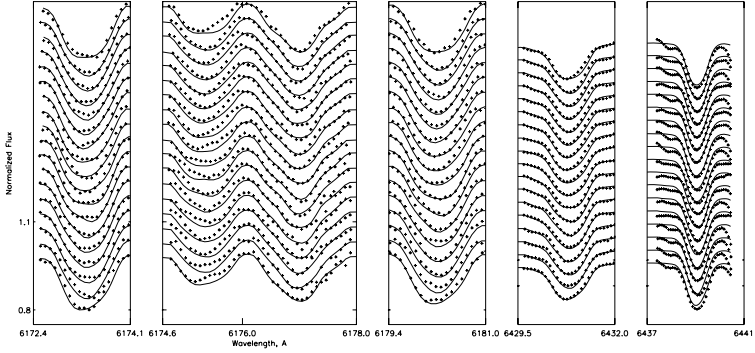3970

3670

Figure 3.32: Same as Fig. 3.28 but with $i = 70°$.

Figure 3.33: A fit to the observations calculated with $i = 70°$. The observed and calculated line profiles are shown by pluses and lines, respectively.
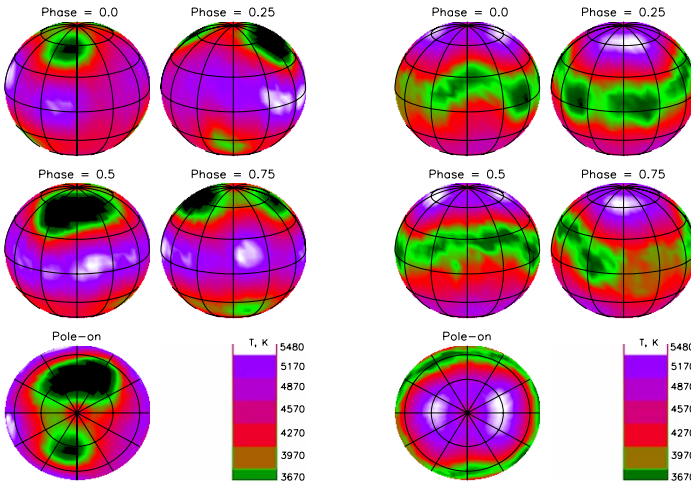

Figure 3.34: Reconstructed surface map of σ Gem for $v \sin i = 25.0$ km/s is shown in four orbital phases with a coordinate grid of 30° in both latitude and longitude. Plotted is the effective temperature distribution given by the colour scale, which is given by the bottom right panel.

Figure 3.35: Reconstructed surface map of σ Gem for $v \sin i = 30.0$ km/s is shown in four orbital phases with a coordinate grid of 30° in both latitude and longitude. Plotted is the effective temperature distribution given by the colour scale, which is given by the bottom right panel.
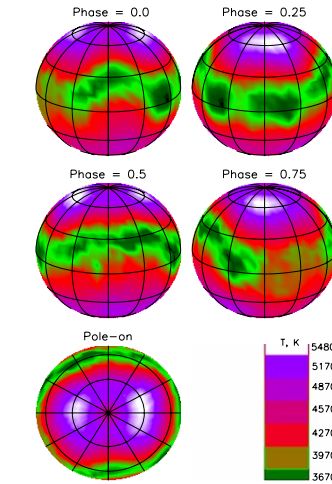
3.3.5 Rotational velocity

Rotation is the main contributor to the formation of magnetic fields in stellar atmospheres. Magnetic fields show up as flares and spots on the stellar surface (see Sec. 2.1). Stellar rotation is described by the projected equatorial velocity, $v \sin i$.

Influence of the rotational velocity on the continuum of the stellar spectra is negligibly small. At the same time, the shape of spectral lines strongly depends on the rotational velocity. The theoretical spectral line profiles calculated with $v \sin i = 10, 50$ and 100 km/s are presented in Fig. 2.4. It is clear that line profiles become shallower with the increasing projected rotational velocity $v \sin i$. The total area in the line after normalization (dividing by the continuum flux, F_c), i. e. the equivalent width W_λ, however, remains same. This fact can be easily explained. Each point of a star emits intensity I_λ, which does not depend on the rest of the star. A change in the rotational velocity shifts I_λ of each point, but does not change the total absorption in the line. Thus the total absorption in the line profile does not vary with $v \sin i$.

The projected velocity of Sigma Geminorum lies within the range 27.5 ± 1 km/s (see Table 3.7). To see an effect of a wrong $v \sin i$ on the results, I made 2 test calculations with intentionally low $v \sin i = 25.0$ km/s and high $v \sin i = 30.0$ km/s projected rotational velocities. Reconstructed maps are presented in Fig. 3.34 for $v \sin i = 25.0$ km/s and in Fig. 3.35 for $v \sin i = 30.0$ km/s and the corresponding fits to the observations are plotted in Fig. 3.38 for $v \sin i = 25.0$ km/s (standard deviation $\Delta = 0.0011477$) and for $v \sin i = 30.0$ km/s in Fig. 3.39 (standard deviation $\Delta = 0.001106$).
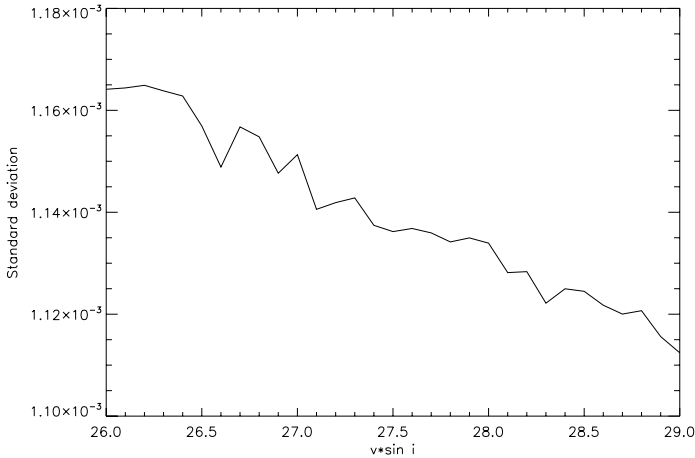

Figure 3.36: Dependence of the standard deviation on the projected rotational velocity in the range from $v \sin i = 26.0$ km/s to $v \sin i = 29.0$ km/s.

Comparing Figs. 3.34 and 3.35 one sees that the smaller value of $v \sin i = 25.0$ km/s results in dark spots close to the pole and some bright spots on the equator. The higher
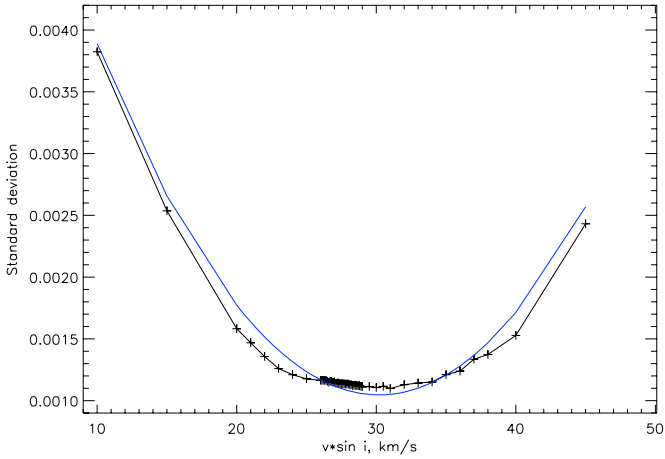
Figure 3.37: Dependence of the standard deviation on the projected rotational velocity $v \sin i$ (black line) and fitted to it parabola (blue line). Points where calculations were done are marked with stars.
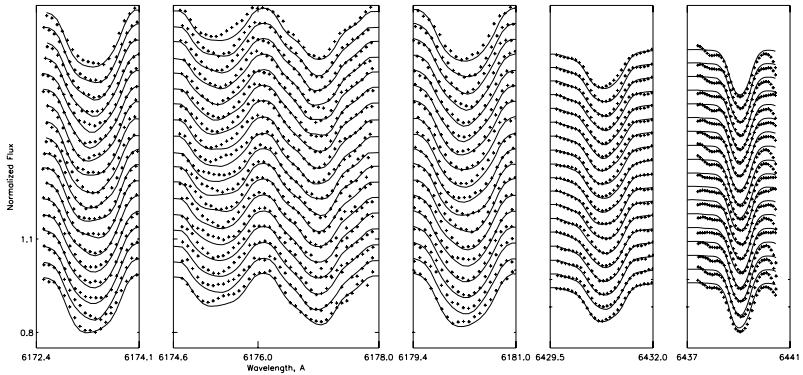

Figure 3.38: A fit to the observations calculated with $v \sin i = 25.0$ km/s. The observed and calculated line profiles are shown by pluses and lines, respectively.

value of $v \sin i = 30.0$ km/s leads to an equatorial belt of spots and some bright spots close to the equator. Thus, presence of any of this effects can be a sign of a wrongly chosen

projected rotational velocity.
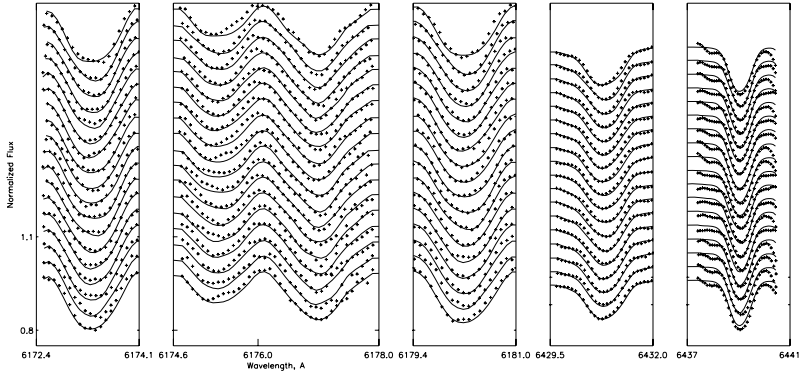
Figure 3.39: Same as Fig. 3.38 but for $v \sin i = 30.0$ km/s.
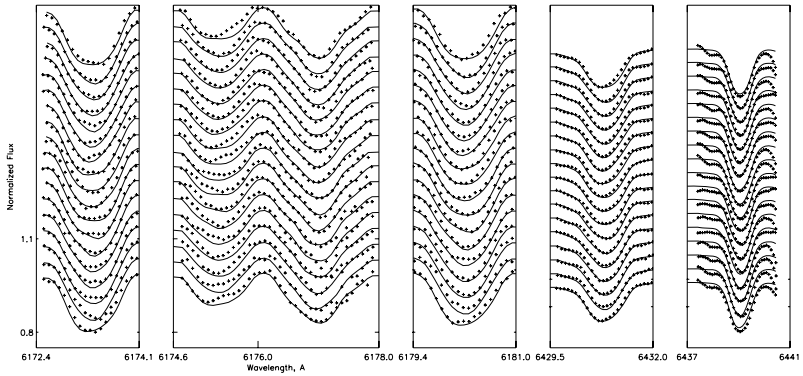
Figure 3.40: Same as Fig. 3.38 but for $v \sin i = 27.2$ km/s.

In order to see an effect of the projected rotational velocity on the results, I calculated standard deviations for 31 values of $v \sin i$ from 26.0 km/s to 29.0 km/s (which is 0.5 km/s out of the range specified in Table 3.7 from both sides) with a step of 0.1 km/s. This dependence is shown in Fig. 3.36. The difference between the maximum and minimum values of the standard deviations in this range is only 0.00005. After some additional

calculations with projected velocities down to 10 and up to 45 km/s and a non-linear least squares fit to the function $\Delta(v\sin i)$ we could get a parabola (see blue line in Fig. 3.37) with the minimum standard deviation $\Delta = 0.001047$ close to $v\sin i = 30$ km/s. The map reconstructed with $v\sin i = 30$ km/s is presented in Fig. 3.35. The map shows significant properties of the wrongly chosen big projected rotational velocity.

As seen from Fig. 3.36, the most stable set of solutions is within the range between $v\sin i = 27.1$ km/s and $v\sin i = 28.0$ km/s. The map reconstructed with $v\sin i = 27.2$ km/s shows a minimum amount of bright spots and dark small spots in the southern hemisphere. Thus I chose this value for $v\sin i$ for my future calculations. The map reconstructed with $v\sin i = 27.2$ km/s is presented in Fig. 3.41 and the corresponding fits to the observations are plotted in Fig. 3.40 (standard deviation $\Delta = 0.001142$).

It is necessary to say that there is a strong correlation between other parameters and the rotational velocity. If one of the fixed parameters is incorrect, then the deduced $v\sin i$ will also be incorrect. Thus, varying of the rotational velocity in order to find the best fit to the observations can be helpfully in case if there is a mistake in the choice of any other parameter.

3.4   Influence of the atomic lines selected for DI on the reconstructions.

To test the reliability of the results we made reconstructions with different sets of atomic lines. 6 atomic lines are chosen for the analysis of the observations from TBL (Fe I 6173 Å, Ni I 6175 Å, Ni I 6177 Å, Fe I 6180 Å and Fe I 6430 Å, Ca I 6439 Å) and only 4 for the observations from NOT (Fe I 6173 Å, Ni I 6175 Å, Ni I 6177 Å, Fe I 6180 Å) as was described in the Sec. 3.2.3. Information about these lines is given in Table 3.8.

Element and its ioniz. state	Wave-length, Å& potential	Exci-tation strength	Oscil-lator	Radiative broadening factor	Stark gamma factor	Van der Waals gamma	Lande factor
Fe I	6173.01	0.990	−6.97	4.057	−6.272	−7.878	2.82
Ni I	6175.36	4.089	−0.30	8.367	−4.888	−7.773	1.00
Ni I	6177.24	1.826	−3.53	7.634	−6.150	−7.833	0.64
Fe I	6180.21	2.727	−2.50	8.167	−6.092	−7.805	0.55
Fe I	6430.85	2.176	−1.80	8.217	−6.194	−7.704	1.24
Ca I	6439.08	2.526	0.20	7.649	−6.072	−7.569	1.12

Table 3.8: Atomic variables for 6 lines used in this work.

Using different atomic lines with different temperature sensitivity can help us to find out what are the general features for all reconstructed stellar surface maps. It is also possible to estimate uncertainties of the model or also in physical processes, because different lines may provide information on slightly different layers of the stellar photosphere. Different temperature sensitivity of 6 atomic lines is illustrated in Fig. 3.42, where we see the
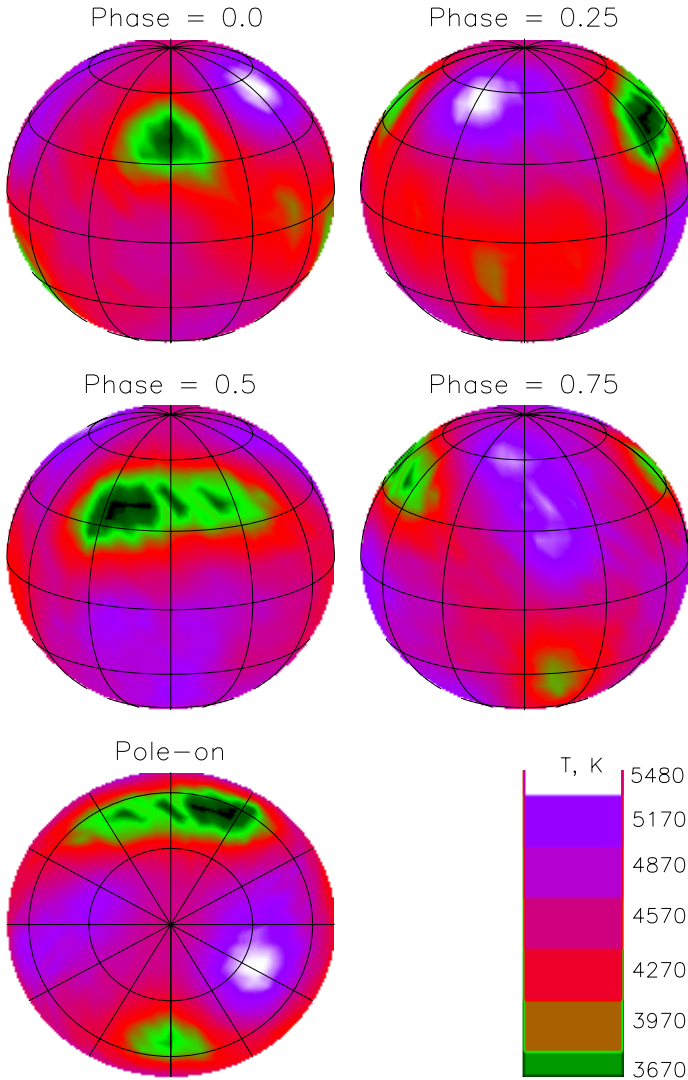
Figure 3.41: Same as Fig. 3.35 but with $v \sin i$ = 27.2 km/s.

dependence of the equivalent width of all lines on the effective temperature, T_{eff} within the range 3500 K to 6000 K. The behaviour of equivalent widths with temperature is different for different atomic lines, which are plotted in different colours.
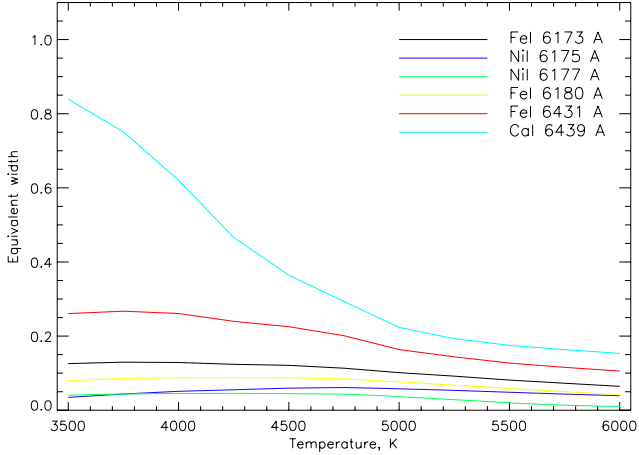

Figure 3.42: Dependance of the equivalent width of 6 atomic lines on the temperature. The black line represents the dependence calculated for Fe I (6173.01 Å), the dark blue line - for Ni I (6175.36 Å), the green line - for Ni I (6177.24 Å), the yellow line - for Fe I (6180.21 Å), the red line - for Fe I (6430.85 Å) and the light blue line - for Ca I (6439.08 Å).

To first order the Doppler Imaging code employed here should take into account the temperature dependence of the individual lines, so that in principles maps from all lines should be similar. However, second order effects remain. Such as the influence of temperature gradient, involved fine structure, changes in microturbulence or hidden blends. These will lead to some changes in the spot maps, whose magnitude needs to be empirically determined. As we see from Fig. 3.42, the widely used Ca I 6439 Å line displays a particularly large temperature dependence.

For this analysis I took the same epoch as in Sec. 3.3, i.e. 18 spectra observed with TBL in December 2001.

3.4.1   4 atomic lines: Fe I 6173 Å, Ni I 6175 Å, Ni I 6177 Å, Fe I 6180 Å

The first set of spectral line profiles which I used for my work was observed with NOT in December 2000. The wavelength region of files containing spectra is within the range from 6158.5 Å to 6199.1 Å. Thus, I could use only 4 atomic lines i.e. Fe I 6173 Å, Ni I 6175 Å, Ni I 6177 Å, Fe I 6180 Å for the reconstruction. Observations from TBL were not restricted to such a small range. Thus, it is possible to use some more lines for
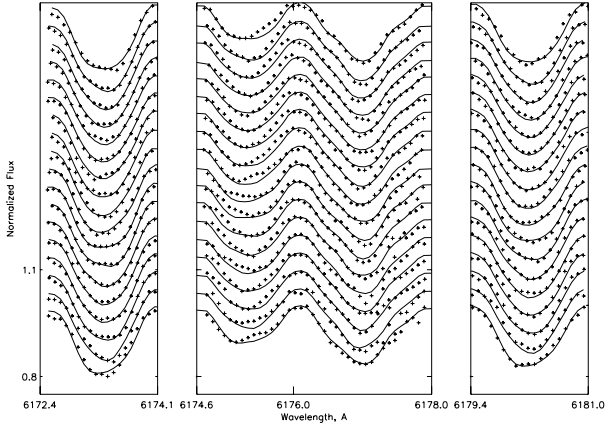
Figure 3.43: A fit to the observations calculated with $v \sin i$ = 26.5 km/s for 4 atomic lines(Fe I 6173 Å, Ni I 6175 Å, Ni I 6177 Å, Fe I 6180 Å). The observed and calculated line profiles are shown by pluses and lines, respectively.
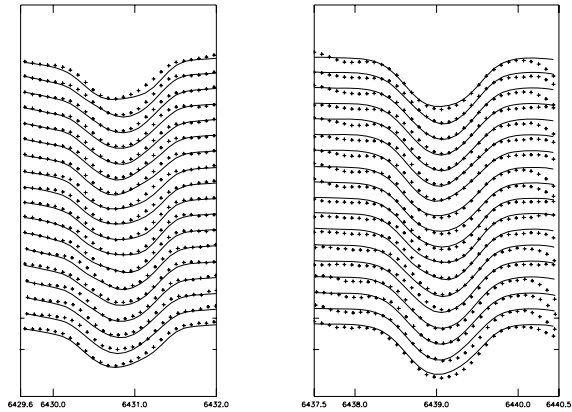

Figure 3.44: Same as Fig. 3.43 but calculated with 2 atomic lines (Fe I 6430.85 Å and Ca I 6439.08 Å) and $v \sin i$ = 27.2 km/s.

the Doppler Imaging. To be able to compare maps reconstructed with 4 lines with maps reconstructed with 6 lines (see Fig. 3.41), I made a test calculation for December 2001 with only 4 atomic lines, with $\log g = 2.5$, macroturbulence, $\zeta = 3.0$ km/s, microturbulence, $\xi = 0.7$ km/s, effective temperature, $T_{eff} = 4750$ K and inclination, $i = 70°$. The best standard deviation ($\Delta = 0.00057$) was achieved with projected rotational velocity, $v \sin i = 26.5$ km/s. The reconstructed map is presented in Fig. 3.45 and the corresponding fits to the observations are plotted in Fig. 3.43.

Compared to the map reconstructed with 6 atomic lines (Fig. 3.41) the map reconstructed with 4 atomic lines shows 2 main groups of spots which are at the same positions as in Fig. 3.41. At the same time the group of spots close to the 0 phase is shifted towards the north pole by a few degrees and the group of spots close to phase 0.5 is smaller on the map reconstructed with 4 atomic lines then on the map reconstructed with 6 atomic lines. It is also shifterd in longitude by $\approx 15°$.

3.4.2 2 atomic lines: Fe I 6430.85 Å and Ca I 6439.08 Å.

Many authors (Hatzes (1993), Kovári et al. (2001), Strassmeier et al. (2003)) based their imaging analysis on only 2 atomic lines, namely on Fe I 6430.85 Å and Ca I 6439.08 Å. Doppler Imaging needs more then 1 separate line for the reconstruction to avoid uncertainties in the solution due to the noise in one line.

If we compare Figs. 3.41 and 3.45 it is clear that some information about stellar spots which is present in the calculations with 6 lines is missing on the map reconstructed with 4 atomic lines . To see the role of Fe I 6430.85 Å and Ca I 6439.08 Å in the reconstructions I made a map of σ Geminorum with these 2 atomic lines. It is presented in Fig. 3.46 and the corresponding fits to the observations are plotted in Fig. 3.44. The calculations were done with the same parameters as in Sec. 3.4.1. The best fit to the observations with $\Delta = 0.00143$ is with $v \sin i = 27.2$ km/s as in the case with 6 lines (Sec. 3.3.5).

As we see from Fig. 3.46, the map reconstructed with Fe I 6430.85 Å and Ca I 6439.08 Å shows spots at the same positions as in Fig. 3.41 which is reconstructed with 6 atomic lines. Also, the size of spots on the last reconstruction is significantly, but not extremely bigger.

In order to compare 3 stellar surface maps of σ Geminorum reconstructed with different sets of atomic lines, I plotted all of their pole-on projections in Fig. 3.47. On the left-hand sight we see a reconstruction based on 4 atomic lines (see Sec. 3.4.1 and Fig. 3.45). The map reconstructed with only 2 atomic lines, which are described in this section (Fig. 3.46) is on the right-hand sight. The resulting map reconstructed with all 6 atomic lines (see Fig 3.41) is in the middle panel.

As it is clear from the Fig. 3.47 the main effect on the reconstructed stellar surface is given by Fe I 6430 Å and Ca I 6439 Å, i.e. those lines which have the highest values of the equivalent width (see the light blue and the red lines in Fig. 3.42).
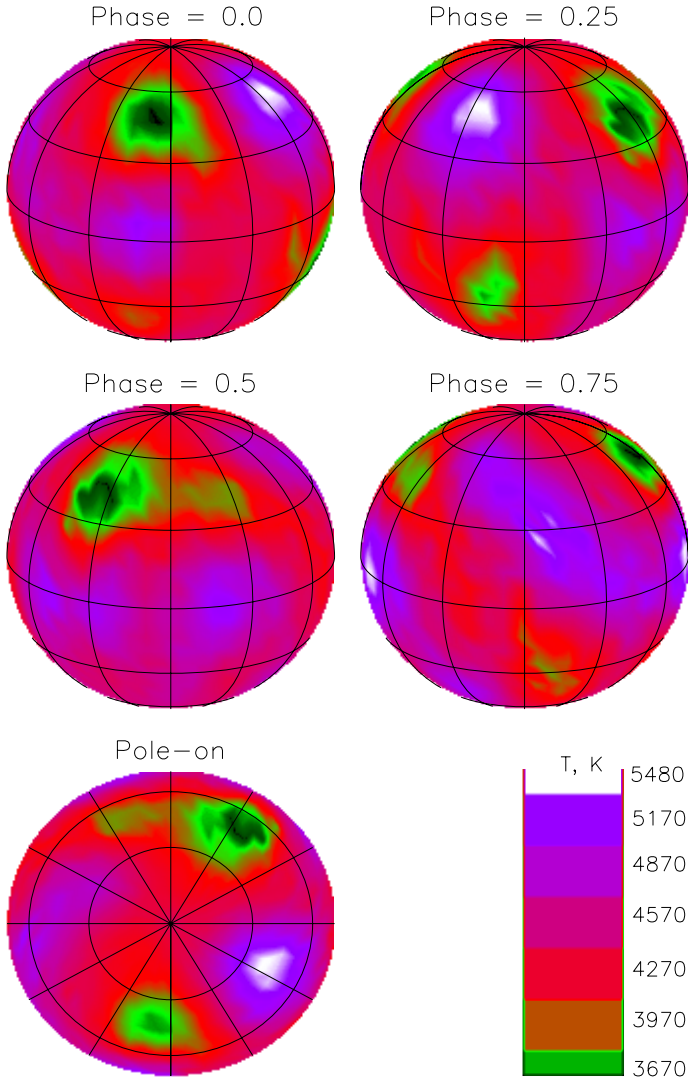
Figure 3.45: Reconstructed surface map of σ Gem with $v \sin i = 26.5$ km/s for 4 atomic lines (Fe I 6173 Å, Ni I 6175 Å, Ni I 6177 Å, Fe I 6180 Å) is shown at four orbital phases with a coordinate grid of 30° in both latitude and longitude. Plotted is the effective temperature distribution given by the colour scale, which is clarified by the bottom right panel.
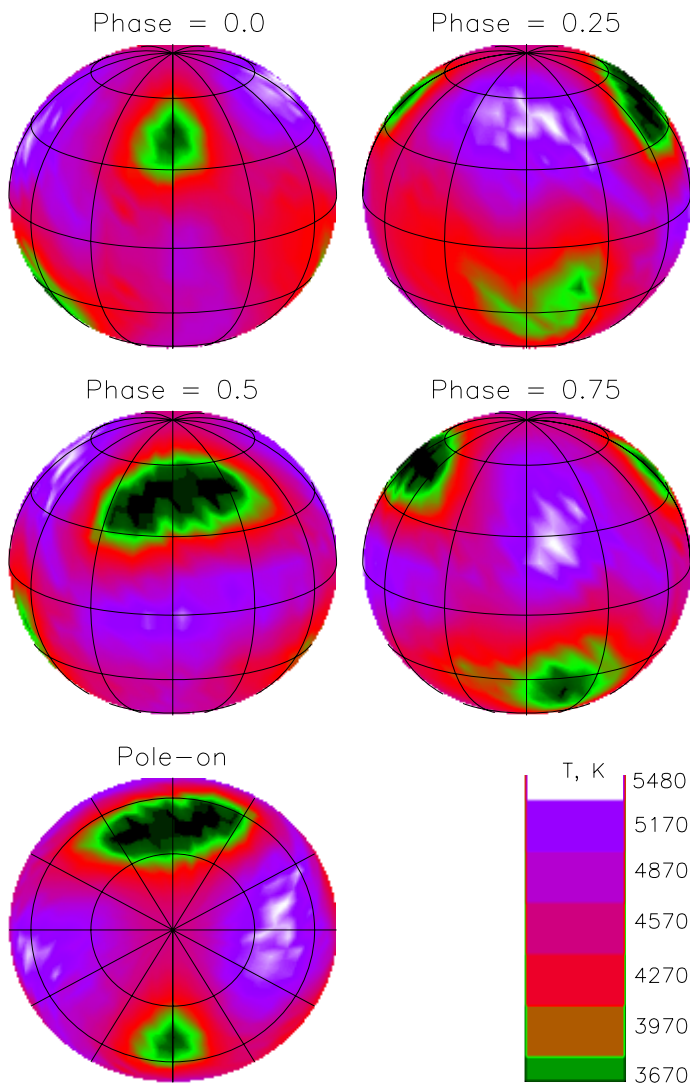
Figure 3.46: Same as Fig. 3.45 but calculated with 2 atomic lines (Fe I 6430.85 Å and Ca I 6439.08 Å) and $v \sin i$ = 27.2 km/s.

3.4.3   3 lines of Fe I

There are 3 lines of Fe I among the 6 atomic lines which I am using for Doppler imaging, i.e. Fe I 6173 Å, Fe I 6180 Å and Fe I 6430 Å. They are all have approximately the same values of the equivalent width and almost the same behaviour of it with the temperature (see the red, the black and the yellow lines in Fig. 3.42). The stellar surface reconstruction based on 3 lines of Fe I is presented in Fig. 3.49 and the corresponding fits to the observations are plotted in Fig. 3.48. The calculations were done with the same parameters as in Sec. 3.4.1. The best fit to the observations with $\Delta = 0.00070$ is with $v \sin i = 26.8$ km/s.

First of all, we see that the reconstructed map is noisy in the southern hemisphere. At the same time two group of spots (close to the 0 and 0.5 phases) are still present at the same position as at all other maps, but they have a smaller size then on the map reconstructed with 6 atomic lines.

3.4.4   2 lines of Ni I

Finally, we have 2 lines of Ni I (Ni I 6175 Å and Ni I 6177 Å)which have the smallest value of the equivalent width. These are the two lines (dark blue and light green) on the bottom of the Fig. 3.42. I reconstructed the stellar surface map using these Ni I lines which is presented in Fig. 3.51 and the corresponding fits to the observations are plotted in Fig. 3.50. The calculations were done with the same parameters as in Sec. 3.4.1. The best fit to the observations with $\Delta = 0.00052$ is with $v \sin i = 26.5$ km/s as for the reconstruction with 4 atomic lines (see Sec. 3.4.1).

The map reconstructed with 2 lines of Ni I map shows the same 2 group of spots at the same positions. One dark spot in the group which is close to 0.5 phase is the same

4 atomic lines   6 atomic lines   2 atomic lines

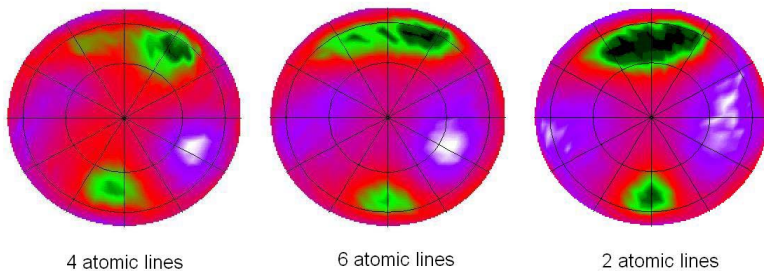Figure 3.47: The pole-on projections of the reconstructed surface maps of σ Gem with different sets of atomic lines. Reconstruction with Fe I 6173 Å, Ni I 6175 Å, Ni I 6177 Å, Fe I 6180 Å is on the left-hand sight, with Fe I 6430 Å, Ca I 6439 Å is on the right-hand sight and with all 6 atomic lines is in the middle. Descriptions to each of these reconstructions are given in Figs. 3.45, 3.41, 3.46.
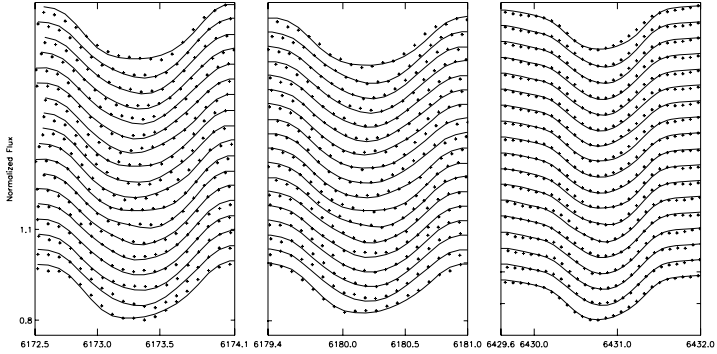
Figure 3.48: Same as Fig. 3.43 but calculated with 3 lines of Fe I (Fe I 6430.85 Å, Fe I 6180 Å and Fe I 6430 Å) and $v \sin i$ = 26.8 km/s.

as on the Fig. 3.44 (the reconstruction with 3 lines of Fe I), but it differs from the Figs. 3.41 (reconstruction with all 6 atomic lines) and 3.45 (reconstruction with 4 atomic lines), where this one big spot is on the opposite site of the second group of spots.

3.4.5   Doppler Imaging with Mean Line Profile.

Doppler Imaging was originally applied to individual line profiles, and it is still the most-used way of its utilization. The idea to use the so-called 'least-squares deconvolution' (LSD) technique for stellar surface reconstruction was proposed by Donati and Collier Cameron (1997).With this technique 'mean' polarized and unpolarized line profile can be found from all available spectral lines. The advantage of the LSD technique is that the signal summarized from a number of spectral lines has a higher effective S/N ratio. A mean line profile extracted from many individual line profiles gives a high precision in the definition of contributions to the line profiles such as the influence of blending lines (Wade et al. 2000b).

The basic assumption underlying this technique is that all spectral lines contain the same information. It means that all spectral features in one observed spectrum are assumed to be identical in shape. The only difference is in the amplitude, which can be derived from the known scaling factor (Wade et al. 2000a). Thus the spectra can be represented as a convolution of a 'mean line profile' with a sum of Dirac functions whose positions and amplitudes correspond to the wavelength and weight of each spectral line. Basic principles of the least squares deconvolution technique are described in Donati et al. (1997).

There is also an option to use different line-masks, in order to derive the LSD-profile only from lines with predetermined properties, e.g. different excitation potentials, different wavelength domains or produced by different elements.
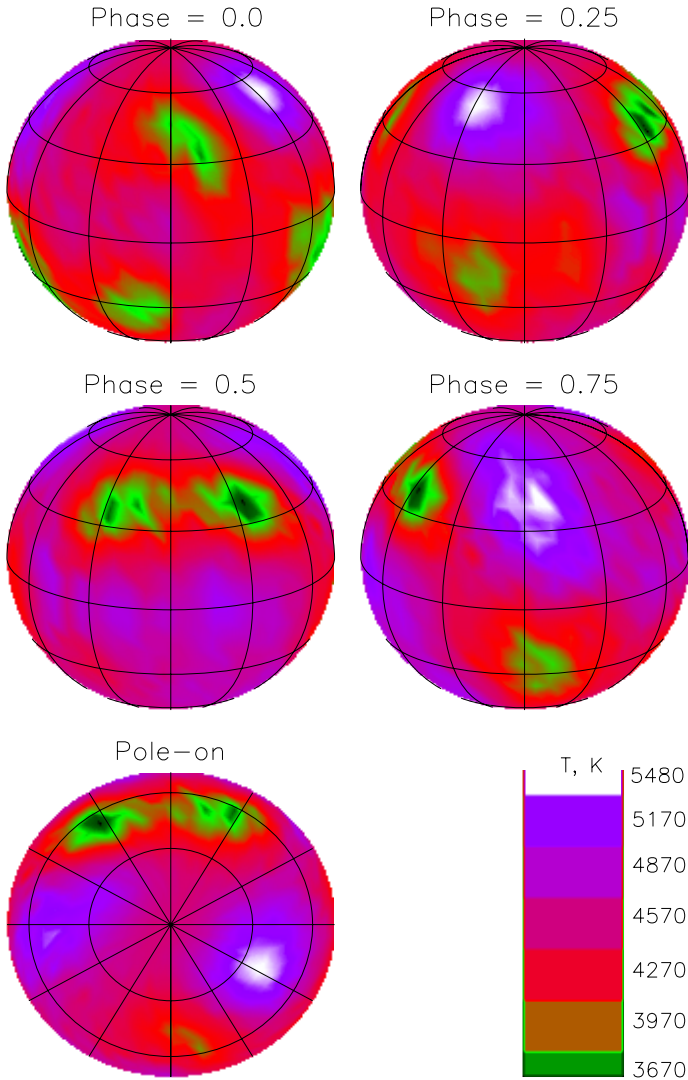
Figure 3.49: Same as Fig. 3.44 but calculated with 3 lines of Fe I (Fe I 6430.85 Å, Fe I 6180 Å and Fe I 6430 Å) and $v \sin i = 26.8$ km/s.
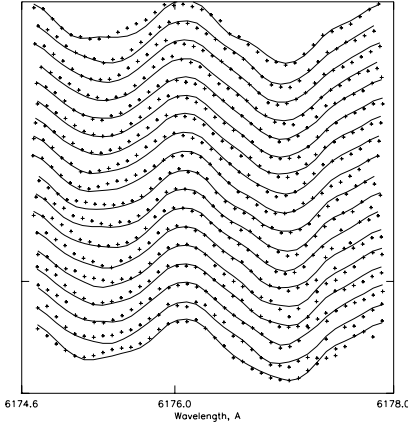
Figure 3.50: Same as Fig. 3.43 but calculated with 2 lines of Ni I (Ni I 6175 Å and Ni I 6177 Å) and $v \sin i = 26.5$ km/s.

In order to compare a map reconstructed using several individual lines with that based on the mean line profiles, I also made calculations for the mean line profiles obtained for 18 spectra observed in December 2001 with the TBL. These mean profiles were computed by P. Petit using the LSD technique. They were extracted from 808 Fe I lines within the spectral range 4489 - 5733 Å. Atomic parameters (ionization state, wavelength, excitation potential, microturbulence, oscillator strength, radiative broadening, Stark gamma factor, Van der Waals gamma factor, Lande factor) for the set of employed Fe I lines is taken from the VALD database (Piskunov et al. 1995). To get the atomic parameters of the mean line profile needed for the calculation of a set of synthetic line profiles, I found the mean value of each parameter for the selected lines taking into account their weights, w, (i.e. the line depth and thus a measure of the contribution of this individual line on the calculated mean line profile) using the following equation:

$$X_{mean} = \sum_{i=1}^{n}(X_i \times w_i)/n, \tag{3.8}$$

where X_{mean} is the mean value of the calculated parameter, X_i is the value of this parameter for the n-th line, w_i is its weight and n is the number of lines. The weight of each spectral line, w, is calculated from equation:

$$w = g\lambda d, \tag{3.9}$$

where g is the magnetic sensitivity (Lande factor), λ is the wavelength of the line center and d is the local line central depth (Donati et al. 1997). The list of selected Fe I lines and their weights provided by P. Petit can be found in Appendix A.
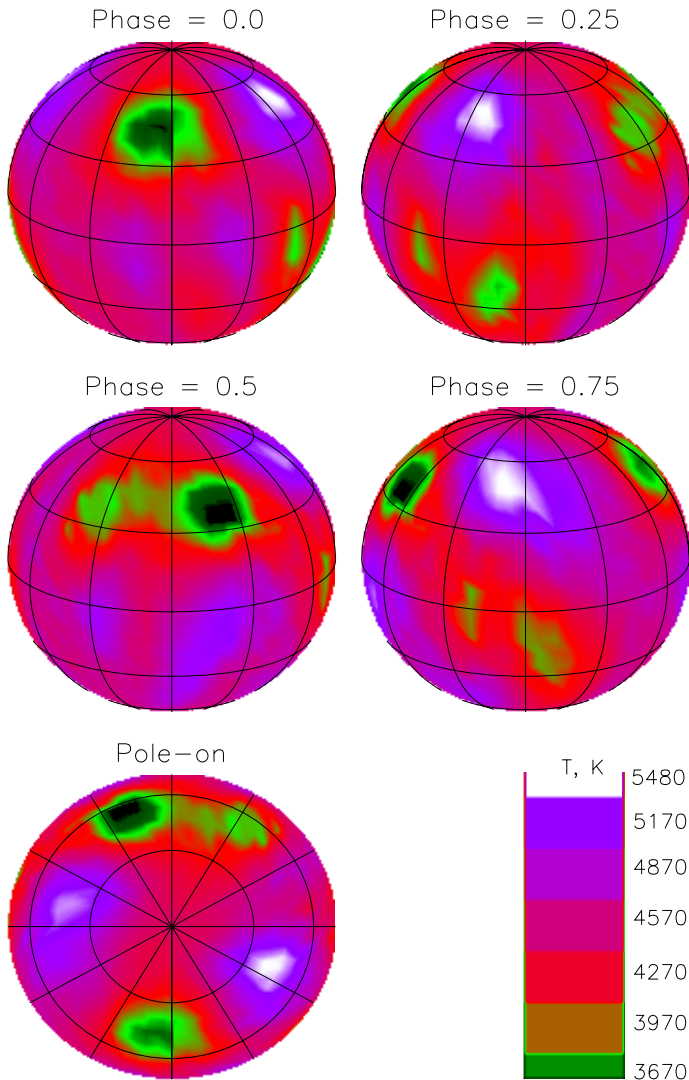
67

Figure 3.51: Same as Fig. 3.44 but calculated with 3 lines of Ni I (Ni I 6175 Å and Ni I 6177 Å) and $v \sin i$ = 26.5 km/s.

Element and its ioniz. state	Wave-length, Å& potential	Exci-tation strength	Oscil-lator	Radiative broadening factor	Stark gamma factor	Van der Waals gamma	Lande factor
MLP	5508.1	3.2629	-2.063	7.778	-5.669	-7.585	1.477

Table 3.9: Atomic parameters for the synthetic Mean Line Profile.

Atomic parameters for the synthetic mean line profile calculated with Eq. 3.8 are listed in Table 3.9. The mean line profile for December 02, 2001 calculated in this way from 808 Fe I lines is compared to LSD profile obtained by P. Petit in Fig. 3.52. The wings of the LSD profile obtained from observed lines (the black line in Fig. 3.52) are extended compared to the synthetic line profile. They are probably residuals of blends and are, of course, absent in the computed profiles.

A map reconstructed with the LSD profiles of σ Gem presented in Fig. 3.54 and the corresponding fits to the observations are plotted in Fig. 3.53. The calculations were done with the same parameters as in Sec. 3.4.1. The best fit to the observations with $\Delta = 0.00033$ was obtained with $v \sin i = 27.2$ km/s, as for the reconstruction with 6 atomic lines (see Sec. 3.4.1) and with 2 Fe I lines (see Sec.3.4.2).

The surface of σ Gem reconstructed with the LSD-profile shows 2 groups of spots.
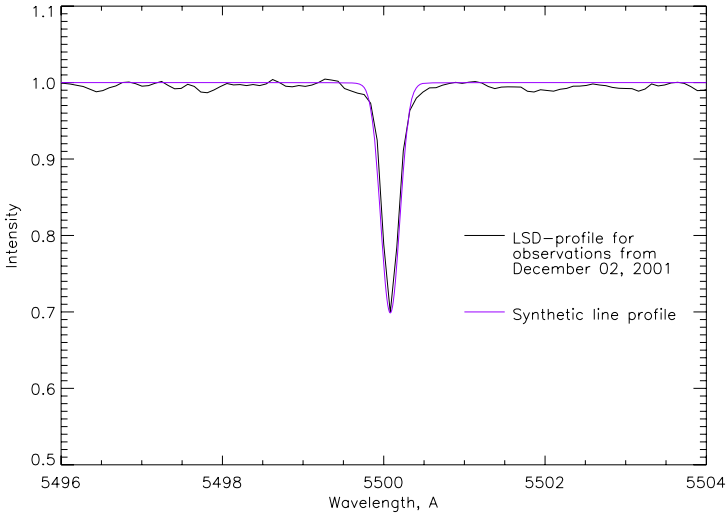
Figure 3.52: Calculated mean line profile (blue line) and LSD profile for December 02, 2001 calculated from 808 Fe I lines (black line).

5499.2   5501.0
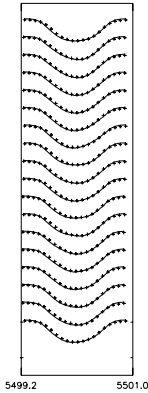
Figure 3.53: Same as Fig. 3.43 but calculated with LSD-profiles and $v \sin i = 27.2$ km/s.

The smaller group is at phase 0 and the bigger one is at phase 0.5. The result is similar to the maps reconstructed in all previous cases with different sets of lines (see Figs. 3.41, 3.45, 3.46, 3.49 and 3.51).

For the bigger group of spots close to phase 0.5, we see the same features as on the map reconstructed with 3 lines of Fe I (See Fig. 3.49) and with 2 lines of Ni I (see Fig. 3.51). This group is mainly composed of 2 spots: the smaller spot is centred at a somewhat earlier phase while the bigger spot is present at a later phase. At the same time, it differs from the map reconstructed with 4 atomic lines (see Fig. 3.45) and with 6 atomic lines (see Fig. 3.41) where the smaller spot is at the later phase and bigger spot is at the earlier phase. The stellar surface reconstructed with 2 atomic lines of Fe I and Ca I shows one big spot at phase 0.5, with the 2 spots being indiscernible.

Figure 3.54: Same as Fig. 3.44 but calculated with LSD-profiles and $v \sin i = 27.2$ km/s.
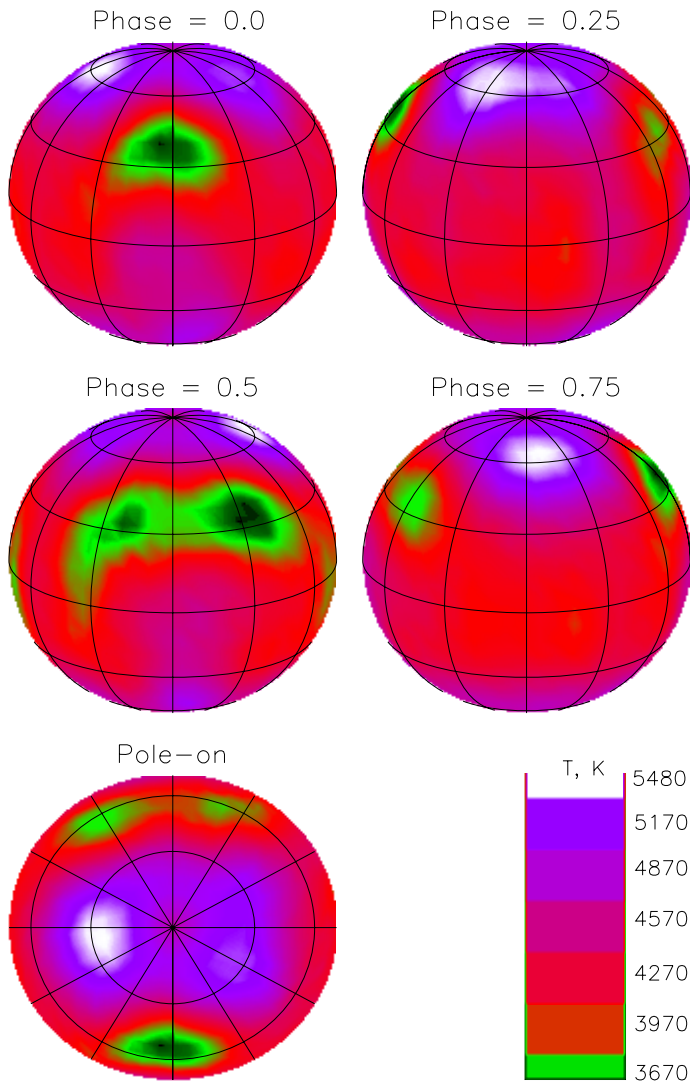
3.5   Summary and conclusions

1. I analysed influence of different physical and geometrical parameters of a star on reconstructed maps of the stellar surface. I found that such parameters as microturbulence and macroturbulence do not have a big influence on the reconstructed map within a reasonable range. Varying surface gravity and inclination leads to a small, but in some cases noticeable difference in the final results. For example, a high value of $\log g$ is responsible for the appearance of one big dark spot in the pole's regions and spots on the maps reconstructed with a much higher inclination are enlarged in the longitudinal direction.

   At the same time, reconstructed maps are very sensitive to the choice of the effective temperature and the rotational velocity. A comparison of different maps, reconstructed with wrong parameters, shows the following effects:

   - low T_{eff} or low $v \sin i$ produce a very contrast dark polar cap and some bright spots on the equator;
   - high T_{eff} or high $v \sin i$ produce an equatorial belt of dark spots and some bright spots close to the pole.

2. The best set of parameters for Sigma Geminorum which are necessary for Doppler Imaging has been found from the minimal standard deviation Δ. Observations from December 2001 taken at the TBL were chosen for the analysis. These parameters are listed in Table 3.8 and are used for later work.

Parameter	Adopted value
$\log g$	2.5
Macroturbulence, ζ	3.0 km/s
Microturbulence, ξ	0.7 km/s
Effective temperature, T_{eff}	4750 K
Inclination, i	70°
Projected rotational velocity, $v \sin i$	27.2 km/s

Table 3.10: Adopted astrophysical parameters of Sigma Geminorum.

   All analysed parameters, except for the effective temperature, are within the range, determined by other authors. T_{eff} is 30 K higher then the maximum limit for the effective temperature reported by Kovári et al. (2001).

3. One of the main conclusion about the reconstructions made with different sets of atomic lines and, the most important, with the Mean Line Profile is that all maps of σ Gem looks similar. Reconstructions based on 6 atomic lines (Fe I 6173 Å, Ni I 6175 Å, Ni I 6177 Å, Fe I 6180 Å, Fe I 6430 Å and Ca I 6439 Å), on 4 atomic lines (Fe I 6173 Å, Ni I 6175 Å, Ni I 6177 Å and Fe I 6180 Å), on 2 atomic lines (Fe I 6430 Å and Ca I 6439 Å), on 3 lines of Fe I, on 2 lines of Ni I and on LSD-profiles show 2 group of spots approximately at the same longitudinal positions close to phase 0 and phase 0.5.

4. Reconstructions of σ Gem surface from November 1996 - January 1997 made by Kovári et al. (2001) show a strong belt of spots instead of separate groups of spots on the maps reconstructed in this work. At the same time our spots exhibit the same latitudes grouped at $+40°$ as in his work.

5. Maps reconstructed with Fe I line (6430 Å) and with Ca I (6439 Å) in the work of Kovári et al. (2001) showed a good agreement between each other. The map reconstructed with Fe I line is more detailed because the iron line has a smaller equivalent width and provides a higher surface resolution than the map reconstructed with Ca I line. In our case lines of Fe I 6173 Å, Ni I 6175 Å, Ni I 6177 Å and Fe I 6180 Å have smaller equivalent widths than atomic lines of Fe I 6430 Å and Ca I 6439 Å (see Fig. 3.42). We observe the same effect as Kovári et al. (2001) on the map reconstructed with 4 atomic lines (see Fig. 3.45) and with 2 atomic lines (see Fig. 3.46). Map reconstructed with 2 atomic lines which have higher equivalent widths is more smoothed and has less details.

6. The difference between our reconstructions and reconstructions of Kovári et al. (2001) based on one line of Fe I (6430 Å) and on one line of Ca I (6439 Å) can be explained only due to use of different DI techniques.

4 Results of Surface Imaging of σ Gem for the period of 1998-2001.

4 surface images of σ Gem reconstructed for four different epochs December 2000 (observations with NOT) and February 1998, February 2000 and December 2001 (observations with TBL) are presented in this chapter. Reconstructions for February 1998, February 2000 and December 2001 are done for 4 atomic lines (Fe I 6173 Å, Ni I 6175 Å, Ni I 6177 Å, Fe I 6180 Å) and for 6 atomic lines (previous 4 lines and Fe I 6430 Å, Ca I 6439 Å). Reconstruction for December 2000 are done only with 4 atomic lines (see Sec. 3.2.3).

4.1 February 1998

4.1.1 Reconstruction with 4 atomic lines

The Doppler Imaging technique was applied to 15 spectra of σ Gem observed with TBL in February 1998. Fig. 4.3 shows the resulting map reconstructed with 4 atomic lines Fe I 6173 Å, Ni I 6175 Å, Ni I 6177 Å and Fe I 6180 Å. The calculations were done with the same physical parameters as in Sec. 3.4.1. The best standard deviation (Δ = 0.00055) was achieved with projected rotational velocity, $v \sin i$ = 26.5 km/s as for the reconstruction with the same 4 atomic lines for December 2001 (see Sec. 3.4.1). The corresponding fits to the observations are plotted in Fig. 4.1. A histogram showing the temperature distribution over the stellar area for for February 1998 with 4 atomic lines is presented in Fig. 4.2.

4.1.2 Reconstruction with 6 atomic lines

Figure 4.6 shows the resulting map of the stellar surface reconstructed with 4 atomic lines Fe I 6173 Å, Ni I 6175 Å, Ni I 6177 Å, Fe I 6180 Å, Fe I 6430 Å and Ca I 6439 Å for February 1998. The calculations were done with the same physical parameters as in Sec. 3.4.1. The best standard deviation (Δ = 0.0014) was achieved with projected rotational velocity, $v \sin i$ = 27.2 km/s as for the reconstruction with the same 6 lines for December 2001 (see Sec. 3.3.5). The corresponding fits to the observations are plotted in Fig. 4.4. A histogram showing the temperature distribution over the stellar area for for February 1998 with 6 atomic lines is presented in Fig. 4.25.

Both maps of stellar surface reconstructed with 4 (Fig. 4.3) and 6 (Fig. 4.6) atomic lines show 3 separate spots. 2 small spots are close to the phases 0.13, 0.25 and the bigger

spot close to the phase 0.7. Spots on the map reconstructed with 4 lines are a bit more elongated in the vertical direction. The spot close to the 0.7 phase is bigger on the map reconstructed with 4 atomic lines.

Figure 4.1: A fit to the observations from February 1998 calculated with $v \sin i =$ 26.5 km/s for 4 atomic lines(Fe I 6173 Å, Ni I 6175 Å, Ni I 6177 Å, Fe I 6180 Å). The observed and calculated line profiles are shown by pluses and lines, respectively.

Figure 4.2: Temperature distribution over stellar area for map reconstructed with 4 atomic lines for February 1998.

Figure 4.3: Reconstructed surface map of σ Gem for February 1998 with $v \sin i =$ 26.5 km/s for 4 atomic lines (Fe I 6173 Å, Ni I 6175 Å, Ni I 6177 Å, Fe I 6180 Å) is shown at four orbital phases with a coordinate grid of 30° in both latitude and longitude. Plotted is the effective temperature distribution given by the colour scale, which is clarified by the bottom right panel.
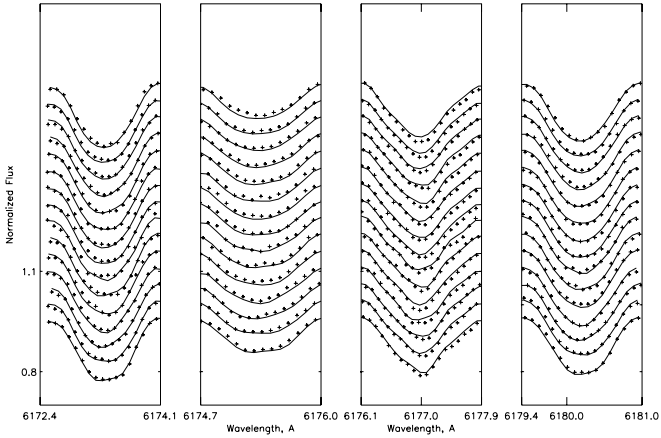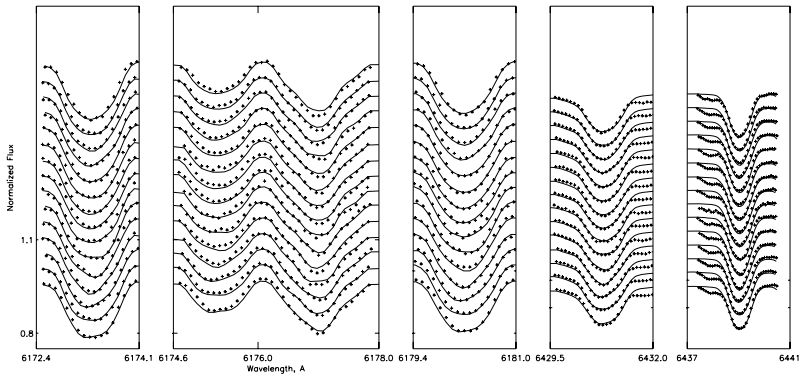
Figure 4.4: A fit to the observations from February 1998 calculated with $v \sin i =$ 27.2 km/s for 6 atomic lines(Fe I 6173 Å, Ni I 6175 Å, Ni I 6177 Å, Fe I 6180 Å, Fe I 6430 Å and Ca I 6439 Å). The observed and calculated line profiles are shown by pluses and lines, respectively.
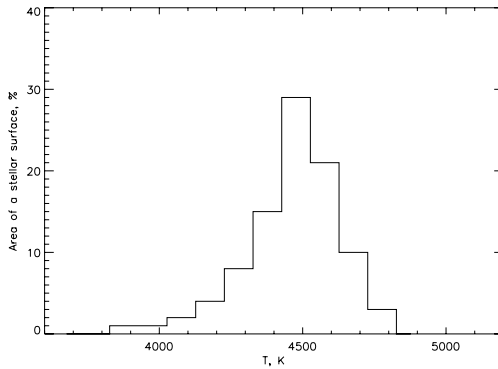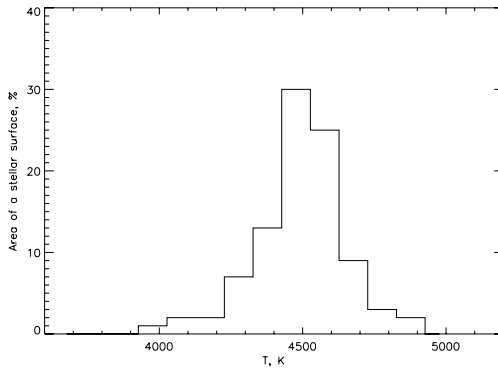

Figure 4.5: Temperature distribution over stellar area for map reconstructed with 6 atomic lines for February 1998.
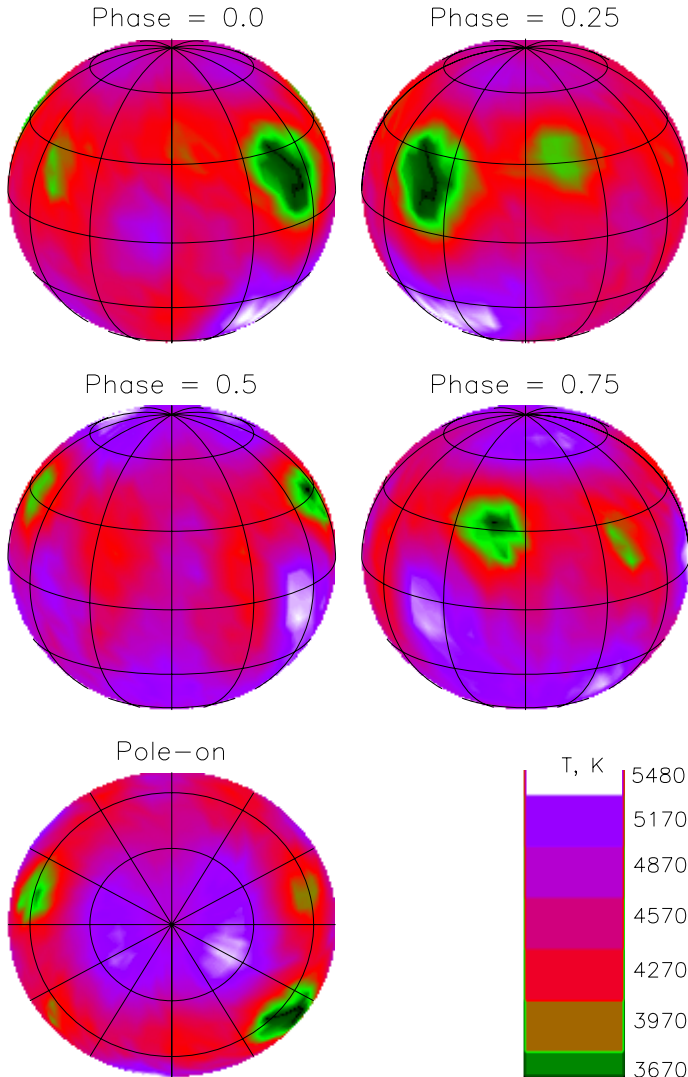
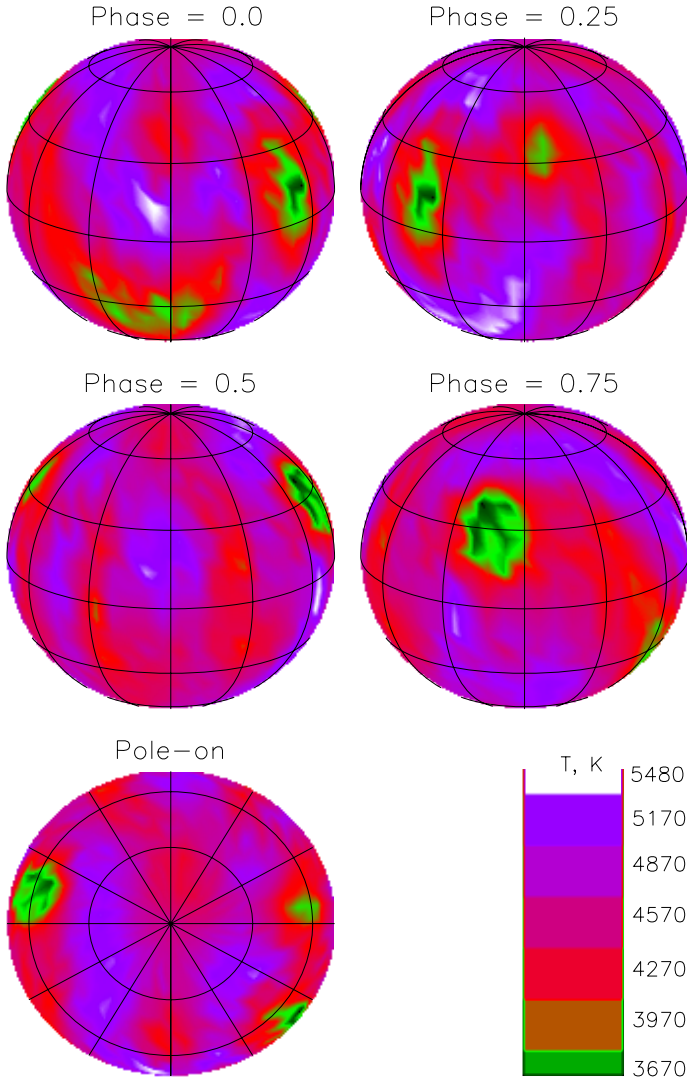Figure 4.6: Reconstructed surface map of σ Gem for February 1998 with $v \sin i =$ 27.2 km/s for 6 atomic lines (Fe I 6173 Å, Ni I 6175 Å, Ni I 6177 Å, Fe I 6180 Å, Fe I 6430 Å and Ca I 6439 Å) is shown at four orbital phases with a coordinate grid of 30° in both latitude and longitude. Plotted is the effective temperature distribution given by the colour scale, which is clarified by the bottom right panel.

4.2 February 2000

4.2.1 Reconstruction with 4 atomic lines

I have 18 spectra observed on TBL in the period between the 02.02.2000 and 08.03.2000. Fig. 4.11 shows the resulting map of σ Gem reconstructed with 4 atomic lines Fe I 6173 Å, Ni I 6175 Å, Ni I 6177 Å and Fe I 6180 Å. The calculations were done with the same physical parameters as in Sec. 3.4.1. The best standard deviation ($\Delta = 0.00045$) was achieved with projected rotational velocity, $v \sin i = 26.5$ km/s as for the reconstruction with the same 4 atomic lines for December 2001 (see Sec. 3.4.1) and for the reconstruction with 4 atomic lines for February 1998 (see Sec. 4.1.1). The corresponding fits to the observations are plotted in Fig. 4.7.

A histogram showing the temperature distribution over the stellar area for for February 2000 with 4 atomic lines is presented in Fig. 4.9.

4.2.2 Reconstruction with 6 atomic lines

Fig. 4.10 shows the surface of σ Gem reconstructed with 4 atomic lines Fe I 6173 Å, Ni I 6175 Å, Ni I 6177 Å, Fe I 6180 Å, Fe I 6430 Å and Ca I 6439 Å for February 1998. The calculations were done with the same physical parameters as in Sec. 3.4.1. The best

Figure 4.7: A fit to the observations from February 2000 calculated with $v \sin i = 26.5$ km/s for 4 atomic lines(Fe I 6173 Å, Ni I 6175 Å, Ni I 6177 Å, Fe I 6180 Å). The observed and calculated line profiles are shown by pluses and lines, respectively.
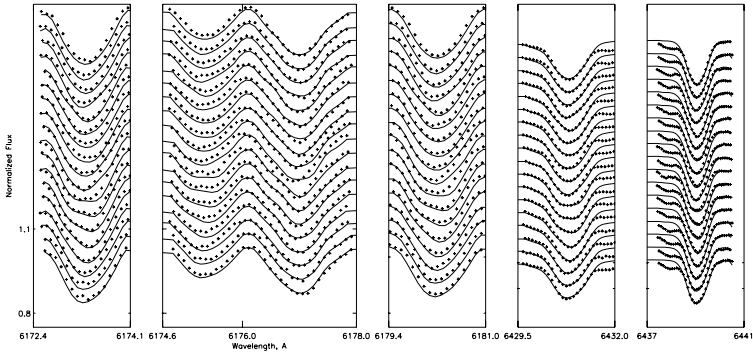
Figure 4.8: A fit to the observations from February 2000 calculated with $v \sin i = 27.5$ km/s for 6 atomic lines(Fe I 6173 Å, Ni I 6175 Å, Ni I 6177 Å, Fe I 6180 Å, Fe I 6430 Å and Ca I 6439 Å). The observed and calculated line profiles are shown by pluses and lines, respectively.
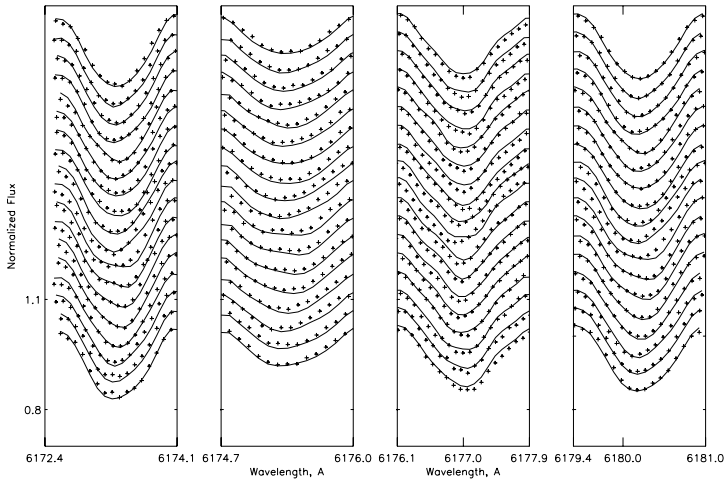
standard deviation ($\Delta = 0.0012$) was achieved with projected rotational velocity, $v \sin i = 27.5$ km/s which is 0.3 km/s higher then for the reconstruction with the same 6 lines for February 1998 (Sec. 4.1.2) and December 2001 (see Sec. 3.3.5). The corresponding fits to the observations are plotted in Fig. 4.8.

A histogram showing the temperature distribution over the stellar area for for February 2000 with 6 atomic lines is presented in Fig. 4.10.

There are 3 spots which are at the same positions on both maps reconstructed with 4 (See Fig. 4.11) and 6 (See Fig. 4.12) atomic lines: close to the phases 0.1, 0.25 and 0.8. The main difference between the maps reconstructed with 4 and 6 atomic lines is the level of noise in the southern hemisphere. It is clear that on the map reconstructed with 6 atomic lines it is almost absent. There is a big spot in the southern hemisphere close to the phase 0.6 on the map reconstructed with 4 lines. This spot could be produced by the small level of signal-to-noise in the observed set of spectra. Using a bigger number of spectral lines for the spectroscopic imaging analysis can help to reduce the noise level. The sizes of two spots at phases 0.1 and 0.25 are comparable on the both stellar surface reconstructions. The spot close to phase 0.8 is much bigger on the map reconstructed with 6 atomic lines than on the map of σ Gem reconstructed with 6 atomic lines.
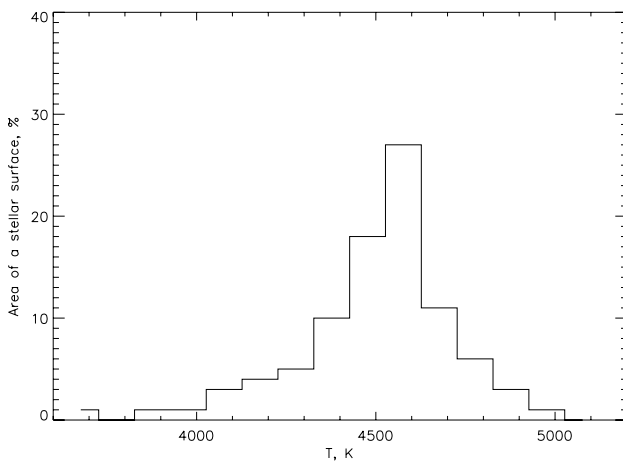
Figure 4.9: Temperature distribution over stellar area for map reconstructed with 4 atomic lines for February 2000.

Figure 4.10: Temperature distribution over stellar area for map reconstructed with 6 atomic lines for February 2000.

Figure 4.11: Reconstructed surface map of σ Gem for February 2000 with $v \sin i =$ 26.5 km/s for 4 atomic lines (Fe I 6173 Å, Ni I 6175 Å, Ni I 6177 Å, Fe I 6180 Å) is shown at four orbital phases with a coordinate grid of 30° in both latitude and longitude. Plotted is the effective temperature distribution given by the colour scale, which is clarified by the bottom right panel.
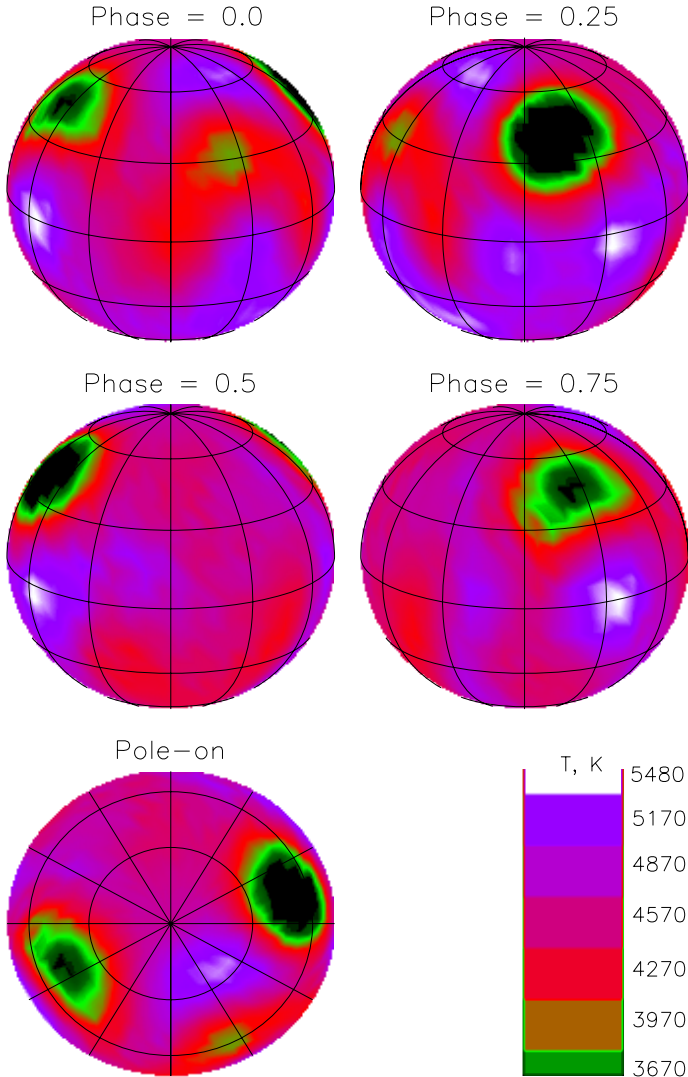
Figure 4.12: Reconstructed surface map of σ Gem for February 2000 with $v \sin i$ = 27.5 km/s for 6 atomic lines (Fe I 6173 Å, Ni I 6175 Å, Ni I 6177 Å, Fe I 6180 Å, Fe I 6430 Å and Ca I 6439 Å) is shown at four orbital phases with a coordinate grid of 30° in both latitude and longitude. Plotted is the effective temperature distribution given by the colour scale, which is clarified by the bottom right panel.

4.3 December 2000

4.3.1 Reconstruction with 4 atomic lines

19 spectra of σ Gem observed with the NOT in December 2000 are used for the Doppler Imaging reconstruction in my work. In this case data with only 4 atomic lines were available to me for a stellar surface reconstruction (see Sec. 3.2.3). A map reconstructed with Fe I 6173 Å, Ni I 6175 Å, Ni I 6177 Å, and Fe I 6180 Å is presented in Fig. 4.15 and the corresponding fits to the observations are plotted in Fig. 4.13. The calculations were done with the same parameters as in Sec. 3.4.1. The best fit to the observations with $\Delta = 0.00045$ was obtained with $v \sin i = 26.5$ km/s as for the reconstruction with the same 4 atomic lines for December 2001 (see Sec. 3.4.1), for February 1998 (see Sec. 4.1.1) and for February 2000 (see Sec. 4.2.1).

A histogram showing the temperature distribution over the stellar area for December 2000 is presented in Fig. 4.14.
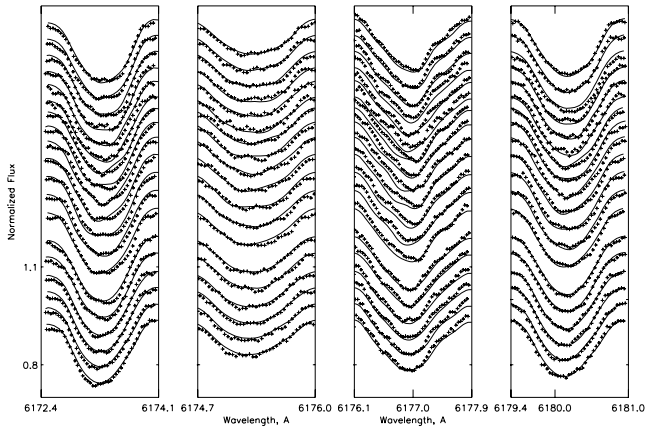
Figure 4.13: A fit to the observations from December 2000 calculated with $v \sin i = 26.5$ km/s for 4 atomic lines(Fe I 6173 Å, Ni I 6175 Å, Ni I 6177 Å, Fe I 6180 Å). The observed and calculated line profiles are shown by pluses and lines, respectively.

4.4 December 2001

Detailed Doppler imaging analysis of 18 spectra observed on TBL in December 2001 are shown in Sec. 3.3 and Sec. 3.4. A map reconstructed with 4 atomic lines is presented in Fig. 3.45 and the corresponding fits to the observations are plotted in Fig. 3.43. A map
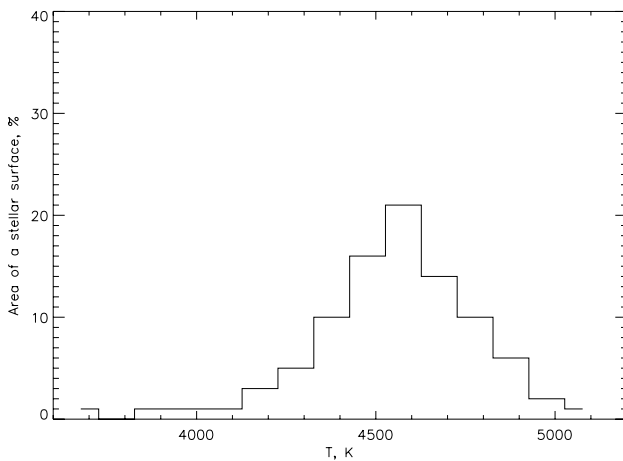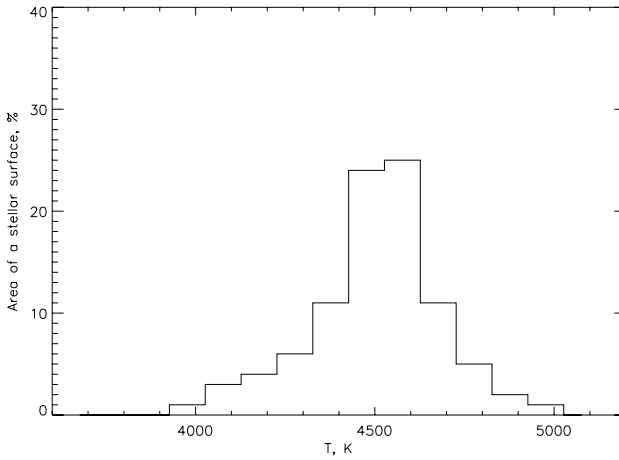
Figure 4.14: Temperature distribution over stellar area for map reconstructed with 4 atomic lines for December 2000.

reconstructed with 6 atomic lines is presented in Fig. 3.41 and the corresponding fits to the observations are plotted in Fig. 3.40.

A histogram showing the temperature distribution over the stellar area for for December 2001 with 4 atomic lines is presented in Fig. 4.16. A histogram showing the temperature distribution over the stellar area for for December 2001 with 6 atomic lines is presented in Fig. 4.17.
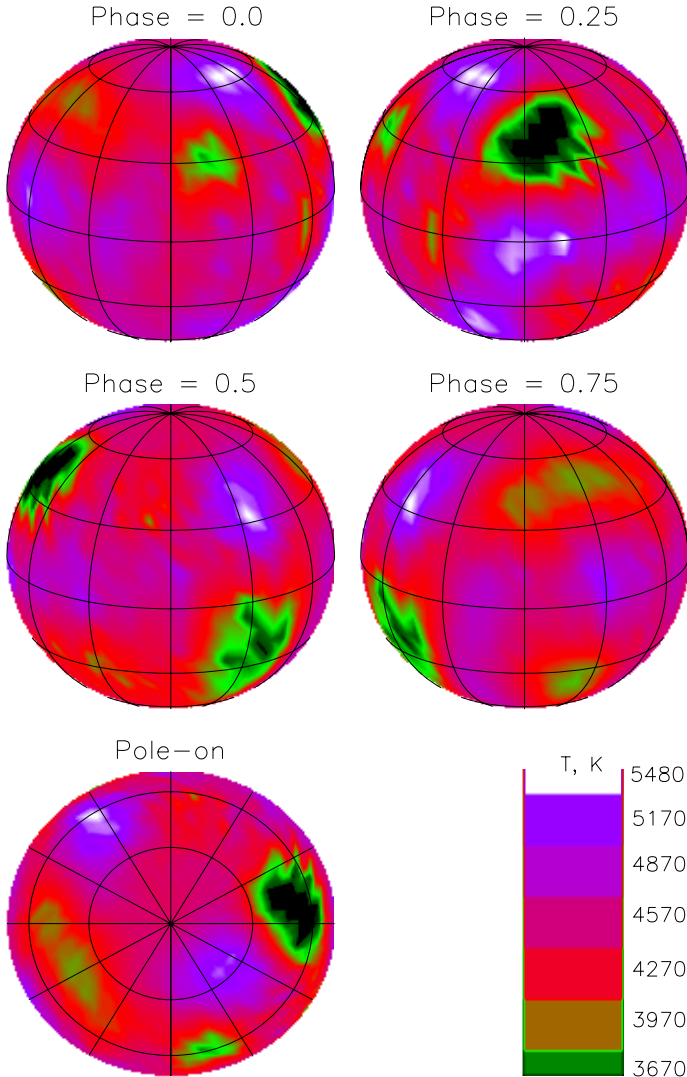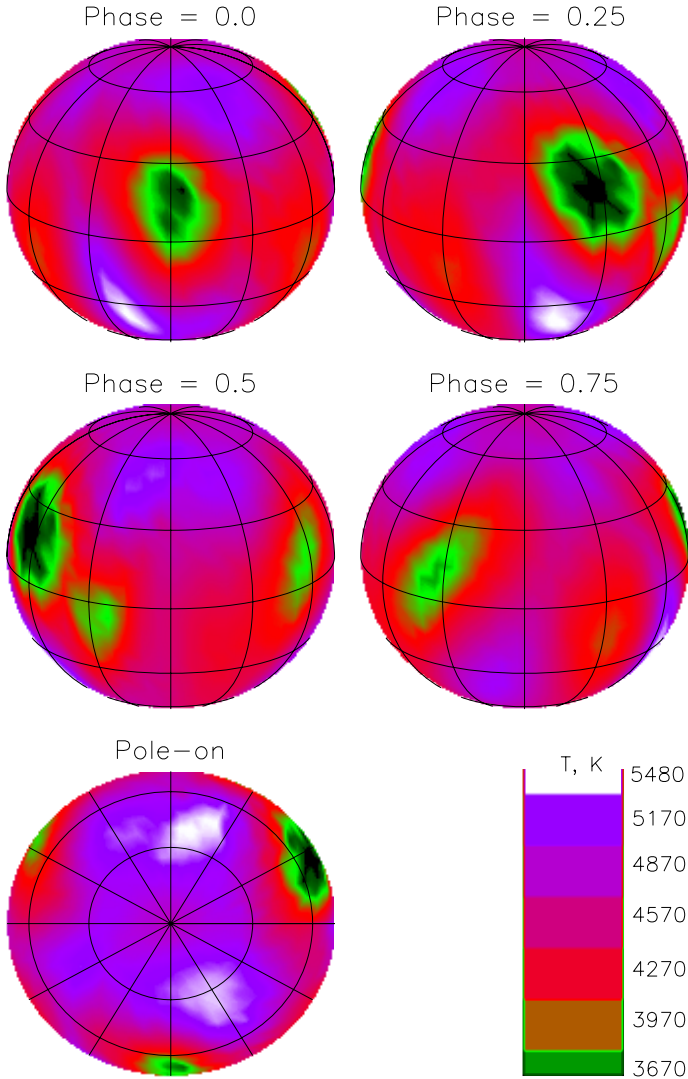
Figure 4.15: Reconstructed surface map of σ Gem for December 2000 with $v \sin i$ = 26.5 km/s for 4 atomic lines (Fe I 6173 Å, Ni I 6175 Å, Ni I 6177 Å, Fe I 6180 Å) is shown at four orbital phases with a coordinate grid of 30° in both latitude and longitude. Plotted is the effective temperature distribution given by the colour scale, which is clarified by the bottom right panel.
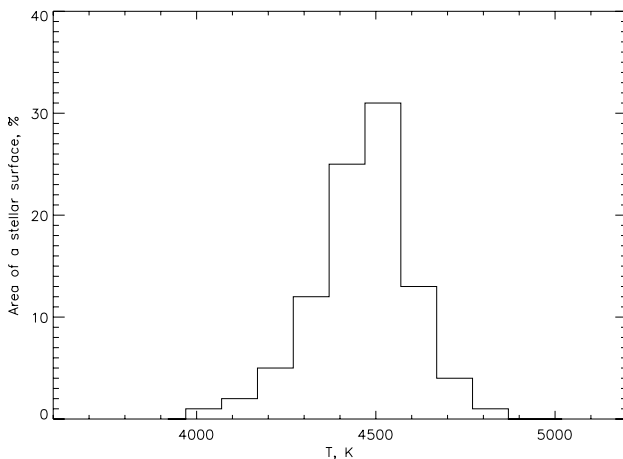
Figure 4.16: Temperature distribution over stellar area for map reconstructed with 4 atomic lines for December 2001.
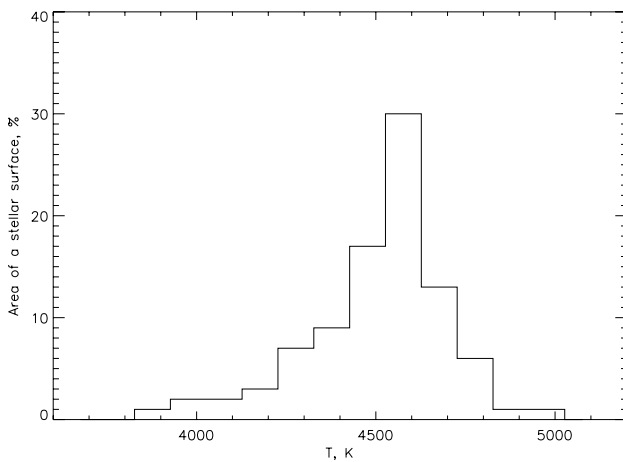
Figure 4.17: Temperature distribution over stellar area for map reconstructed with 6 atomic lines for December 2001.

4.5   The evolution of spots during 1998 - 2001

The pole-on projections of 4 stellar surface maps of Sigma Geminorum reconstructed with 4 atomic lines (Fe I 6173 Å, Ni I 6175 Å, Ni I 6177 Å, Fe I 6180 Å) is presented in Fig. 4.19. We see 3 groups of spots on the maps reconstructed from February 1998, February 2000 and December 2000. There are only 2 group of spots on the map reconstructed from December 2001.

   The most reliable information which we can get from the Doppler images is the positions of spots and, in particular, their longitudes (see the comparison of different stellar surface maps reconstructed with different physical parameters and based on different sets of atomic lines in Chapter 3). To see how spots change their longitudinal positions see Fig. 4.18, where longitudes of spot groups are plotted versus time. The zero-point on the x-axis represents January, 1998. The zero-point on the y-axis represents the central meridian (in our case it is the meridian which was observed as a central one at the zero-phase, $P_0 = 2\,450\,388.36853$, taken from Kovári et al. (2001) (see Sec. 3.2.3)). I assume that spots located roughly at same longitude are the same, although it may also be that fresh flux (new spots) appeared near the same longitude. There is a possibility that 2 spots which were observed in February 1998, February 2000 and December 2000 and marked with blue and light green colours on Fig. 4.18 merged in one group of spots as was reconstructed for December 2001.

Figure 4.18: Longitudinal spot migration during the period of February 1998 - December 2001. The zero-point on the x-axis represents January 1998. Positions of different spots are marked with different colours.
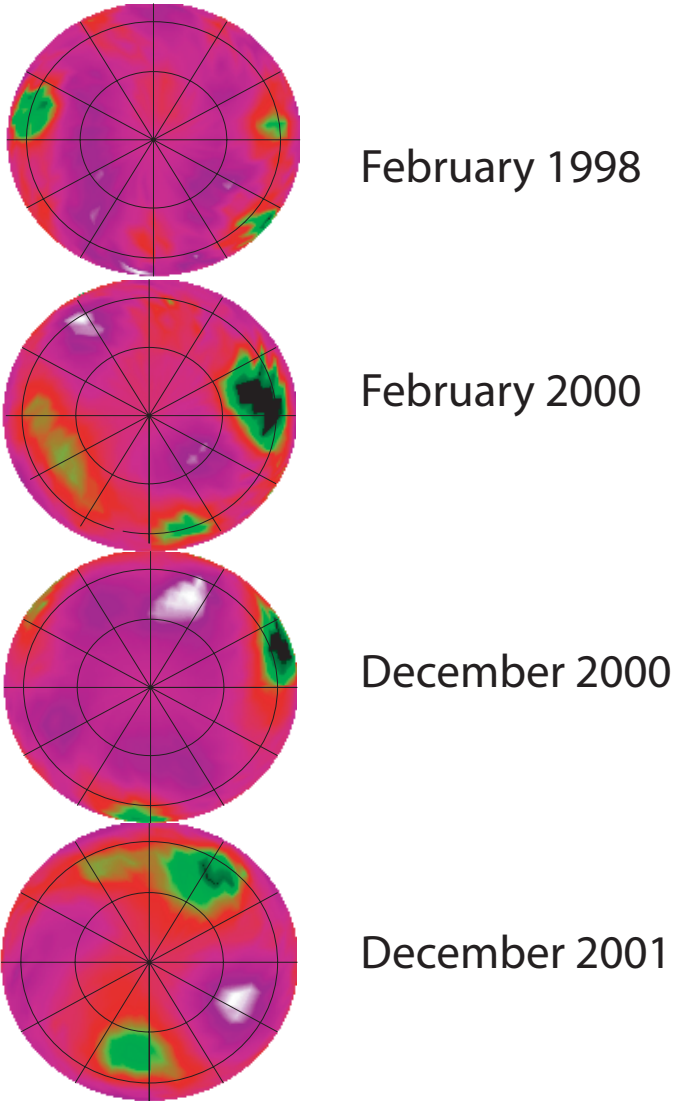
Figure 4.19: The pole-on projections of the reconstructed surface maps of σ Gem for 4 sets of observations (February 1998, February 2000, December 2000 and December 2001). Reconstructions were done with 4 atomic lines Fe I 6173 Å, Ni I 6175 Å, Ni I 6177 Å, Fe I 6180 Å. Descriptions to each of these reconstructions are given in Figs. 4.3, 4.7, 4.10, 3.45.

Latitudinal migration of spots plotted versus time is presented in Fig. 4.20. The zero-point on the x-axis represents January 1998. All group of spots exhibit low latitudes mainly between 0° and +50°. The minimal spot latitude -5° is present on the map reconstructed with observations from NOT in December 2000. The maximal spot latitude +60° is present on the map reconstructed with TBL observations from February 2000.

None of the reconstructed maps showed high latitude spots or polar spots. This result is in agreement with the all earlier published stellar surface reconstructions of σ Gem from 1991-1992 (Hatzes 1993) and from November 1996 - January 1997 (Kovári et al. (2001) and Strassmeier et al. (2003)).
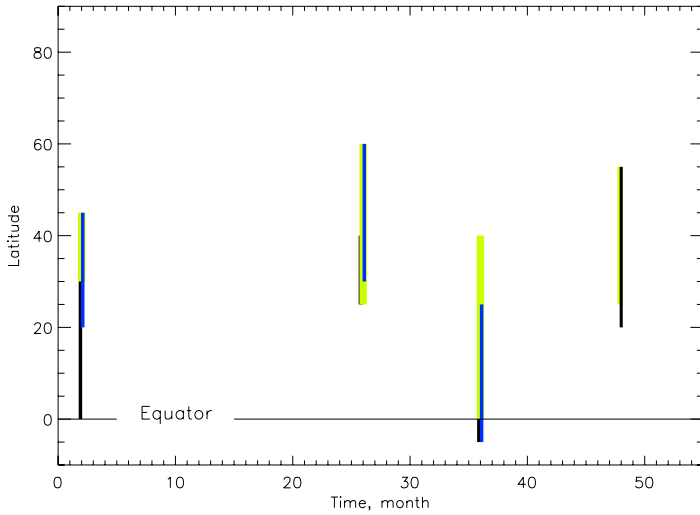
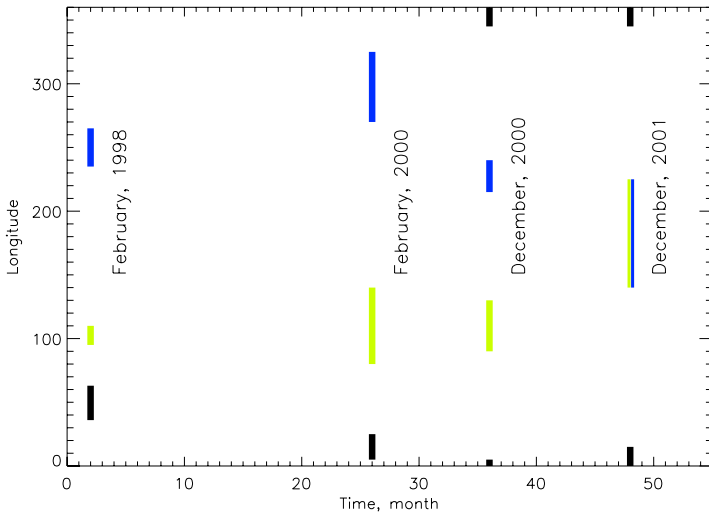Figure 4.20: Latitudinal spot migration during the period of February 1998 - December 2001. The zero-point on the x-axis represents January, 1998. Positions of different spots are marked with different colours.

4.6   Summary and conclusions

1. I reconstructed 4 maps of σ Gem which show the temperature distribution over the stellar surface for February 1998, February 2000, December 2000 and December 2001 (Fig. 4.19). All maps show 2 or 3 groups of spots which exhibit low latitudes from 0° till +50°. There are no high latitude or even polar spots on the reconstructed maps.

Author	Years of observations	Result of stellar surface reconstruction
Photometric imaging		
Fried et al. (1983)	1976 - 1981	The light curve has shown two minima, separated by roughly a half cycle.
Jetsu (1996)	1976 - 1992	Two active longitudes separated by 180°.
Henry et al. (1995)	1977 - 1992	Nearly all solutions fit to two spots separated by 0.47 of the phase.
Strassmeier et al. (1988)	1981 - 1986	At least 2 spots or spot groups.
Zhang and Zhang (1999)	1993 - 1994	Probable presence of 2 cool spots separated by 0.3 of the phase.
Kovári et al. (2001)	1996 - 1997	Presence of 3 spots. Cool regions do not reach latitudes higher than $\approx 60°$.
Spectroscopic imaging		
Hatzes (1993)	1991 - 1992	Reconstructions with 5 spots grouped at a latitude +55°.
Kovári et al. (2001)	1996 - 1997	Maps show a belt of spots at approximately +45° latitude and a width of 30°.
Strassmeier et al. (2003)	1996 - 1997	Spot groups along a band at $\approx 45°$ and width $\approx 30°$ or centered at the equator.
This study	1998 - 2001	3 maps with three and 1 map with 2 spot groups mainly between 0° and +50°.

Table 4.1: Comparison of surface reconstructions of σ Gem made by different authors and based different methods and on observations from different years.

2. Comparison of 4 maps shows clear confirmation for spots evolution on times scales at least several months between 2 consistent observations. This evolution of spots

on the stellar surface can be seen in Figs. 4.18, 4.20, where longitudinal and latitudinal migrations of spots during the investigated period are shown.

3. In order to compare results of our reconstructions with both photometric and spectroscopic imaging made by other authors, I put short extracts from their results in Table 4.1. Our results are in a good agreement with both photometric and spectroscopic imaging. There two groups of spots separated by $\approx 180°$ on the map of σ Gem for December 2001 as was reported by Fried et al. (1983), Jetsu (1996), Henry et al. (1995), Strassmeier et al. (1988) and Kovári et al. (2001). There are 3 groups of spots on the maps reconstructed for February 1998, February 2000 and December 2000 as was presented in the work of Kovári et al. (2001). All spot groups on the reconstructed maps in this work are on the low latitudes between 0° and +50°. There are now high latitudinal or polar spots. Hatzes (1993), Kovári et al. (2001) and Strassmeier et al. (2003) reported about approximately the same low latitude spots for Sigma Geminorum.

5 Summary and outlook

- Tests with different spectral lines and different techniques (including comparison with literature results) show that σ Gem has multiple low-latitude spots. On the visible hemisphere there are 2-3 spot groups located in general below a latitude of 45°. There is no sign of a polar or high-latitude spot, as present on more rapidly rotating stars. This may have to do with the relatively slow rotation of sigma-Gem ($P_{rot} \approx 19.6$ days), which would mean that the Coriolis force is not as strong as on more rapid rotators. These results are robust and are found using different spectral lines, including the use of the LSD line profile.

- Except for a single feature, which may be present on two or maybe (with some migration) even three images, no other spot survives at the same position between 2 images. This implies that the average lifetime of the starspots on σ Gem is lower than approximately a year (unless the spots migrate by a very significant amount).

- In general there is a stronger, larger spot with a weaker (or more than one) spot approximately 180° from it. There is an indication that the longitude of the dominant spot may have flipped by approximately 180° between February 1998 and 2000 (see Fig. 4.19). This is the first sign of a flip-flop of activity on this star. The "flip-flop" phenomenon has been found mainly on very active, very rapidly rotating stars and typically shows the relatively sudden jump of large activity from one longitude of the star to the opposite hemisphere. These jumps happen periodically, with a period of typically 3-4 years. See Berdyugina and Tuominen (1998) and Berdyugina (2005).

- Temperature histograms are relatively symmetric, with a longer tail towards lower temperatures (starsspots) than to higher temperatures (stellar faculae). These histograms evolve slowly, suggesting that any activity cycle of this star is either much longer than the period of time observed, or is not very strong (i.e. the difference between activity maximum and minimum is small).

- There is no evidence of bands of low-lying starspots, as found by Kovári et al. (2001). This finding is in agreement with that of Hatzes (1993) and Strassmeier et al. (2003) in the literature.

- There is a strong need for longer time series, i.e. the continuing observation of this star in order to confirm that it really possesses a flip-flop cycle and to determine the length of this cycle. In addition a longer data base might reveal if there is a significant activity cycle of this star.

A The list of Fe I lines and their weights used for extracting of LSD-profile

The list of 808 of Fe I lines with their wavelength (λ) and weights is presented in the following Table. Values of weights are provided by Pascal Petit.

λ, Å	w	λ, Å	w	λ, Å	w	λ, Å	w
4489.7393	1.490	4737.5933	0.500	5016.4761	2.678	5326.1401	0.661
4490.0830	1.156	4737.6348	1.260	5018.4199	0.954	5328.0376	1.271
4490.4990	0.476	4740.3398	2.508	5019.7319	1.470	5328.5308	1.353
4490.7622	0.585	4741.0688	2.562	5020.8159	0.772	5329.9873	0.578
4490.8081	0.526	4741.5288	2.714	5021.6753	1.126	5332.6631	0.399
4492.6768	0.334	4744.6357	1.842	5021.9331	4.226	5332.8994	1.644
4493.3711	0.874	4744.9399	0.998	5022.2358	1.178	5333.1421	0.577
4494.4697	0.474	4745.1279	1.060	5025.0801	0.262	5333.7656	0.490
4494.5630	1.135	4745.7998	1.293	5027.1201	1.780	5339.4033	1.284
4495.3892	0.657	4749.5928	0.219	5027.2261	1.982	5339.9277	1.588
4495.4238	0.598	4749.9482	1.093	5027.7559	1.158	5341.0229	1.024
4495.5659	1.189	4757.5820	2.240	5028.1260	1.596	5349.7334	2.498
4495.9531	1.168	4760.0679	2.676	5029.6211	2.282	5353.3730	2.806
4496.2710	0.366	4765.4800	1.968	5030.7793	1.588	5361.6216	1.668
4498.5332	0.719	4766.8647	1.986	5031.0391	1.850	5365.3960	1.798
4498.5933	0.662	4768.3193	1.232	5031.0391	1.850	5369.9580	1.111
4502.5908	1.178	4768.3970	1.656	5031.2129	1.452	5371.4302	0.710
4504.8301	0.591	4769.1030	1.412	5031.9150	1.574	5371.4893	0.683
4509.3052	0.239	4771.6958	2.476	5036.9219	2.298	5371.5962	0.988
4510.8208	1.007	4772.8032	1.404	5039.2500	1.436	5379.5742	1.020
4511.0420	0.481	4772.8301	1.312	5040.2520	0.289	5382.4736	0.950
4513.7139	0.543	4776.0688	1.266	5040.8530	0.647	5383.3691	1.158
4514.1841	1.031	4776.3613	1.522	5040.9009	0.377	5386.3350	0.885
4515.1650	1.124	4779.4429	1.342	5041.0708	1.606	5386.9590	0.730
4516.2720	0.753	4780.8110	1.406	5041.7271	0.325	5389.4785	0.952
4516.4492	0.446	4785.7212	0.921	5041.7549	1.126	5391.4609	1.312

Continued on the next page...

λ, Å	w	λ, Å	w	λ, Å	w	λ, Å	w
4517.5259	0.854	4785.9570	1.397	5041.8467	1.042	5393.1670	1.576
4517.6001	0.521	4786.8062	1.150	5044.2100	1.657	5397.1270	1.830
4518.4321	0.519	4787.8271	1.427	5048.1689	0.386	5397.1929	1.420
4518.5771	1.755	4789.6553	0.938	5048.4331	1.271	5397.6191	0.688
4520.2451	0.628	4790.7461	0.692	5049.8188	1.196	5398.2769	1.530
4523.4009	1.612	4791.2500	0.614	5051.2759	1.452	5400.5020	2.282
4523.9268	0.800	4793.9609	0.538	5051.6338	1.447	5400.6563	0.636
4525.1411	1.254	4794.3550	0.972	5052.9658	0.584	5401.2642	1.532
4525.1411	1.254	4795.1030	0.258	5054.6421	1.033	5403.8179	1.482
4525.8633	2.236	4798.2651	1.820	5055.9932	2.134	5404.1118	1.434
4526.5620	2.376	4798.7310	1.922	5056.8413	1.978	5404.1494	1.310
4527.7827	2.130	4799.4063	2.050	5057.4980	2.208	5405.3477	1.920
4528.6128	2.366	4799.7690	0.782	5058.0342	1.524	5405.7739	1.722
4528.7568	0.870	4800.1279	3.192	5058.4961	1.332	5406.3320	1.954
4528.8149	1.040	4800.6479	2.282	5060.0493	0.450	5406.7700	1.172
4531.1470	2.508	4802.8760	0.912	5060.0781	1.486	5407.3809	1.648
4531.5820	0.786	4802.8760	0.912	5064.5811	0.720	5407.4780	1.268
4531.6250	0.992	4802.8809	1.356	5064.9551	1.262	5409.1333	2.496
4531.6353	0.466	4802.8809	1.356	5065.0142	1.176	5410.9102	1.970
4533.1299	1.262	4804.5171	1.284	5065.1943	1.604	5417.1055	1.696
4533.9609	1.834	4804.5942	0.516	5067.1509	2.276	5421.8486	0.812
4536.4883	0.362	4807.7080	2.246	5068.7651	3.518	5423.7402	0.883
4537.6709	1.322	4808.1470	2.036	5069.4219	1.238	5424.0693	1.250
4538.7490	2.014	4809.1367	1.196	5072.0762	1.428	5428.6987	0.426
4538.9458	1.246	4809.9399	1.314	5072.6680	2.464	5429.4189	0.390
4539.6909	1.288	4813.1162	1.534	5074.7480	2.010	5429.5039	1.125
4540.6582	0.426	4815.2310	2.124	5075.1689	2.964	5429.6963	1.580
4541.3159	2.184	4816.6680	1.276	5076.2617	1.050	5429.8271	0.582
4541.9429	1.460	4817.7778	0.836	5078.9717	3.764	5432.9463	0.429
4542.4111	1.656	4820.9990	1.704	5079.2241	2.970	5436.2969	0.946
4542.6973	0.598	4823.2300	1.154	5079.7393	3.196	5437.0830	0.039
4546.6802	0.512	4824.1670	0.686	5083.3379	1.340	5445.0420	1.234
4547.0171	2.132	4826.5649	0.795	5084.5459	0.854	5446.5747	0.276
4547.8462	1.832	4832.7280	0.858	5094.9648	0.666	5446.8706	1.122
4549.4629	1.138	4834.5059	1.287	5096.4067	0.838	5446.9160	0.764
4551.6489	2.054	4835.8691	1.107	5096.9980	1.207	5448.2690	1.776
4553.4839	1.444	4837.9409	1.358	5098.5698	1.399	5452.0923	0.792
4554.4512	1.204	4838.0889	1.600	5098.6992	1.517	5455.4414	2.704
4555.7500	0.337	4838.5127	2.632	5099.0752	0.768	5455.6094	1.710
4556.0879	0.545	4839.5449	1.898	5100.9009	1.420	5461.5503	2.110
4556.1260	0.801	4839.7661	1.106	5102.6489	2.194	5462.9531	1.554

λ, Å	w	λ, Å	w	λ, Å	w	λ, Å	w
4556.9248	0.713	4840.3218	2.160	5104.0288	2.462	5464.2778	1.724
4560.0879	0.503	4840.8940	2.706	5104.4360	0.914	5466.9873	2.136
4560.2593	1.177	4842.7881	1.206	5107.4458	2.146	5466.9873	2.136
4564.8237	1.170	4843.1440	2.686	5107.6411	3.182	5472.7100	2.230
4565.3120	1.720	4843.3857	1.434	5109.6499	1.778	5473.1641	0.946
4565.3550	1.096	4844.0132	1.656	5110.3569	1.034	5473.9004	1.405
4565.6631	3.388	4844.0801	0.818	5110.4131	1.864	5476.2871	0.996
4566.5142	1.656	4845.6470	0.568	5113.2510	1.520	5476.5630	1.489
4566.9917	1.016	4845.6470	0.568	5115.7759	1.436	5478.4561	1.089
4568.7642	3.606	4845.6499	1.578	5121.6411	1.784	5480.8643	1.292
4568.8408	1.262	4845.6499	1.578	5125.1123	2.588	5481.2422	1.229
4571.4370	2.236	4847.7153	1.844	5125.8359	0.942	5481.4380	1.534
4572.8604	2.060	4848.2041	2.772	5126.1919	2.022	5482.2651	0.583
4573.3882	1.816	4848.8823	3.566	5127.3579	3.206	5483.0981	1.511
4574.2148	3.106	4849.6680	2.086	5127.6812	1.892	5487.1440	0.720
4574.7173	2.688	4851.8691	1.704	5129.6299	0.969	5487.4810	0.544
4575.7817	1.574	4854.8760	1.510	5131.4697	2.438	5487.7632	0.732
4576.5200	1.032	4855.6719	2.704	5131.4697	2.438	5487.7666	0.478
4579.8208	2.656	4858.2412	0.228	5136.0908	0.222	5492.0728	0.696
4580.4600	2.420	4859.1191	2.098	5139.2510	1.875	5493.3242	0.447
4580.5752	1.354	4859.7407	1.512	5139.4624	1.788	5493.4966	1.300
4581.5068	1.708	4860.9771	2.174	5141.7388	1.020	5494.4609	0.392
4581.5068	1.708	4862.5947	0.786	5142.4932	0.456	5497.5156	2.596
4582.9399	2.432	4867.5283	1.850	5142.5420	0.698	5501.4644	4.326
4583.7212	2.460	4868.3730	1.813	5142.9272	1.654	5505.7471	1.316
4584.7148	2.660	4869.4619	1.023	5143.7217	0.305	5505.8818	2.642
4586.9917	1.660	4870.0371	0.613	5145.0938	1.730	5506.7778	4.610
4587.1279	1.770	4871.3174	1.034	5145.7271	0.783	5512.2539	1.868
4587.7158	0.990	4871.9282	1.198	5148.0361	2.206	5512.3970	1.552
4592.6509	1.128	4872.1357	2.297	5148.2251	2.370	5513.3916	1.604
4594.9409	1.562	4873.7520	0.749	5150.1973	1.830	5521.1230	0.328
4595.2080	0.744	4875.8750	1.356	5150.8379	3.244	5521.2842	1.662
4595.3579	1.256	4876.1870	0.581	5151.9097	3.236	5522.4468	2.464
4596.0601	1.243	4877.6050	0.667	5154.1011	2.206	5524.2490	1.472
4596.4141	0.558	4878.2080	2.992	5164.1382	1.586	5529.1606	0.348
4597.0566	0.224	4880.5220	2.120	5164.5532	1.750	5532.7432	0.268
4598.1182	0.662	4881.7183	1.064	5164.6919	0.606	5532.8589	0.164
4598.3242	0.617	4881.7339	1.086	5164.9160	0.588	5534.6621	0.780
4598.7451	0.669	4882.1440	1.786	5165.4072	2.552	5535.4170	0.871
4600.9321	1.718	4885.4302	1.588	5166.2813	3.922	5535.4170	0.871
4601.3062	2.260	4886.1812	0.604	5167.4873	2.532	5536.5830	0.935

λ, Å	w	λ, Å	w	λ, Å	w	λ, Å	w
4601.3062	2.260	4886.3262	2.834	5167.7197	1.642	5539.2842	0.979
4602.0000	1.902	4887.1909	1.852	5168.8970	3.562	5543.1470	1.348
4602.9399	3.422	4887.3662	1.468	5169.2964	2.192	5543.9365	1.433
4603.3428	2.084	4888.6318	2.834	5171.5947	1.544	5546.9912	0.771
4603.9521	1.790	4889.0000	1.588	5171.6743	0.672	5549.5508	0.910
4604.8511	0.868	4889.1021	2.470	5172.2041	0.802	5551.7769	0.754
4605.0933	2.306	4890.7539	3.578	5175.7129	0.707	5553.2202	1.033
4605.9829	2.402	4891.4922	2.262	5177.2339	0.773	5553.5791	0.889
4607.6470	2.234	4893.6953	1.498	5184.1719	0.673	5555.1230	1.408
4607.6470	2.234	4896.4380	2.284	5184.2578	0.443	5557.9058	0.640
4611.1851	2.372	4903.3081	4.476	5184.2651	0.860	5557.9775	2.040
4611.2837	1.436	4905.1338	2.192	5187.9141	0.863	5560.2070	1.424
4611.2891	0.522	4905.2178	1.726	5191.4551	2.095	5562.1167	1.916
4611.2891	0.522	4907.7329	1.322	5192.3433	1.940	5562.7061	2.814
4611.3481	0.702	4908.0288	1.100	5194.9409	1.194	5563.5991	2.244
4613.2041	0.012	4909.3838	1.194	5195.4683	1.908	5563.6729	0.972
4614.2051	1.026	4910.0151	1.140	5196.0771	2.094	5563.6934	0.426
4618.7568	2.620	4910.3252	0.722	5198.7109	3.126	5565.7036	2.006
4619.2871	3.056	4910.5620	1.195	5202.2510	1.346	5567.2939	0.554
4625.0439	1.702	4911.7788	1.087	5202.3350	2.018	5567.3921	1.450
4625.0972	0.926	4912.4980	0.927	5204.5820	3.850	5568.0718	1.696
4627.5479	2.512	4915.8481	0.889	5206.8013	1.958	5568.8672	0.616
4630.1211	1.389	4917.2290	1.176	5207.9390	1.506	5569.6182	1.604
4630.7754	0.852	4918.9541	0.643	5208.5933	3.052	5572.8413	2.180
4632.8179	1.358	4918.9932	0.926	5209.8838	1.066	5573.1001	2.108
4632.9111	0.800	4920.5020	1.229	5213.8047	1.498	5581.9014	0.321
4633.0469	1.036	4924.7700	2.632	5215.1787	3.034	5583.9678	0.659
4633.7549	0.646	4925.2813	2.552	5216.2739	1.488	5584.2627	0.931
4635.5498	0.343	4927.4170	1.086	5217.3887	3.012	5584.7637	0.260
4635.6162	0.855	4930.3149	1.758	5217.9189	1.458	5585.6372	1.741
4635.8457	1.844	4932.9819	0.982	5221.4312	3.748	5586.7559	1.243
4637.5029	1.348	4933.2930	1.264	5222.3936	0.941	5587.5732	0.888
4638.0088	3.012	4933.3340	1.318	5223.1875	0.383	5592.2310	0.530
4643.4629	3.256	4934.0059	0.928	5224.3013	0.492	5594.6538	0.908
4647.4326	2.268	4934.0820	1.108	5225.5249	2.435	5600.2256	1.000
4649.8198	1.228	4937.2891	1.248	5226.8623	1.498	5600.2256	1.000
4653.3721	1.570	4938.1748	1.086	5226.8950	0.513	5602.7666	1.364
4653.4321	0.616	4938.8130	3.998	5227.1504	0.540	5602.9448	0.786
4653.4878	1.808	4939.2378	2.260	5227.1885	0.580	5608.9741	0.834
4654.4971	3.342	4939.2378	2.260	5229.8447	0.862	5615.2988	2.152
4654.6089	1.668	4939.6860	3.096	5229.8799	0.772	5615.6191	1.028

λ, Å	w	λ, Å	w	λ, Å	w	λ, Å	w
4654.6289	1.410	4942.4570	1.056	5232.9390	1.367	5615.6440	1.894
4657.5850	2.344	4942.5898	0.426	5235.3887	1.168	5618.6309	2.226
4658.2939	1.260	4945.6357	1.250	5236.2051	0.296	5619.2241	1.710
4661.9697	2.546	4946.3779	1.392	5236.3813	0.785	5620.4907	2.140
4663.1782	1.27	4946.3848	1.700	5240.3569	0.454	5624.5420	2.646
4664.7070	1.164	4949.6772	1.138	5241.9033	1.015	5635.8242	0.448
4667.4531	1.303	4950.1040	1.331	5242.4907	0.985	5636.6963	0.785
4668.0669	0.803	4952.6040	0.340	5243.7734	2.306	5637.1089	0.146
4668.1318	0.517	4952.6387	0.780	5245.6182	2.202	5638.2617	1.050
4669.1719	1.689	4957.2979	1.628	5247.0488	4.298	5641.4360	0.807
4672.8291	0.134	4957.5972	0.730	5249.1055	1.330	5643.9229	1.129
4673.1631	1.325	4957.6763	0.735	5250.2080	6.462	5649.6299	0.533
4673.2710	1.612	4961.9150	0.497	5250.6450	3.072	5650.7036	0.784
4674.6479	0.532	4965.7769	2.566	5253.4614	2.900	5652.0112	0.417
4678.8447	2.420	4966.0869	2.768	5254.9551	4.924	5652.3198	1.016
4680.2939	3.318	4967.2578	2.920	5255.6831	1.510	5655.4888	0.704
4680.4668	2.078	4967.8901	3.572	5255.7529	1.448	5655.4937	0.713
4682.5591	3.222	4968.3931	2.692	5257.6538	1.256	5655.4937	0.713
4683.5610	2.670	4969.9160	2.866	5259.0913	1.846	5658.5308	2.386
4685.0239	1.370	4970.4990	1.344	5262.6079	1.298	5658.6577	0.590
4687.3018	2.718	4970.6460	3.134	5262.8818	2.208	5658.8159	1.463
4687.3857	2.052	4973.1011	1.200	5263.3052	3.076	5659.6899	1.799
4690.1362	3.728	4977.0039	2.126	5263.3940	1.734	5660.8003	0.806
4690.3711	3.996	4977.6470	2.442	5263.8623	1.488	5661.3481	0.877
4690.3711	3.996	4978.1069	1.618	5265.9365	1.692	5662.5151	1.249
4691.4111	1.970	4978.6040	0.488	5266.5552	2.734	5662.9370	0.761
4700.1919	1.968	4978.6890	2.302	5269.5366	2.676	5665.6343	0.780
4700.4189	2.234	4979.5879	1.166	5270.3569	0.834	5667.6680	1.710
4701.0469	2.486	4980.2842	2.846	5273.1631	1.535	5677.6836	1.420
4701.0469	2.486	4980.5400	2.316	5273.3740	0.515	5679.0254	2.406
4702.9141	2.124	4982.5239	2.640	5273.6240	0.766	5686.1250	1.190
4705.4570	0.390	4983.2671	3.070	5274.9766	1.114	5698.0229	0.598
4707.2720	1.013	4983.8652	2.816	5277.3057	0.558	5698.3662	0.551
4707.4883	1.401	4985.2510	2.176	5277.3057	0.558	5701.5449	1.225
4708.9678	0.690	4985.5459	3.676	5280.2788	0.312	5702.3491	0.643
4709.0859	1.557	4986.2251	1.220	5280.3618	0.896	5705.4658	0.567
4710.2827	0.706	4986.9033	1.820	5281.7900	1.230	5707.0488	1.052
4712.1050	1.436	4991.2671	1.244	5283.6211	1.579	5709.3779	1.485
4714.0679	1.157	4991.7959	2.124	5284.4263	0.255	5711.8501	1.040
4714.1909	0.791	4994.1289	1.581	5284.6089	0.537	5712.1309	1.861
4716.8389	2.286	4995.4058	0.843	5288.5278	0.923	5715.0908	0.575

λ, Å	w	λ, Å	w	λ, Å	w	λ, Å	w
4719.1089	1.298	4999.1143	1.093	5293.9629	1.410	5715.1001	0.704
4720.9551	0.450	5001.8618	1.094	5294.5469	1.278	5717.8350	0.710
4720.9990	1.998	5002.5820	0.671	5298.7764	2.282	5721.7041	0.147
4726.1372	3.236	5002.7891	1.351	5300.4121	0.986	5721.7041	0.147
4727.0049	1.566	5004.2119	0.317	5302.2993	3.114	5731.7622	2.352
4727.3989	3.762	5004.3398	0.506	5307.3604	3.068	5732.8633	1.382
4728.5449	2.696	5005.7109	1.303	5308.7070	1.834		
4729.0171	2.408	5006.1172	1.585	5312.4731	0.848		
4729.6782	1.866	5007.2930	1.078	5317.5239	1.950		
4731.6001	2.332	5007.7280	0.636	5320.0391	0.635		
4733.5908	2.718	5012.0669	2.986	5321.1089	0.736		
4734.0938	1.462	5012.1528	1.802	5322.0410	0.649		
4735.8418	1.996	5012.4409	1.986	5323.5103	0.884		
4736.7720	2.418	5014.9409	2.028	5324.1777	1.618		

Bibliography

Ayres, T. R., Simon, T., Linsky, J. L., 1984, Sigma Geminorum (K1 III + ?) - Variability of the ultraviolet emission lines near conjunction, Astrophys. J., 279, 197–201

Berdyugina, S. V., 1998, Surface imaging by the Occamian approach. Basic principles, simulations, and tests, Astron. Astrophys., 338, 97–105

Berdyugina, S. V., 2005, Starspots: A Key to the Stellar Dynamo, Living Reviews in Solar Physics, 2, 8–+

Berdyugina, S. V., Tuominen, I., 1998, Permanent active longitudes and activity cycles on RS CVn stars, Astron. Astrophys., 336, L25–L28

Berdyugina, S. V., Solanki, S. K., Frutiger, C., 2003, The molecular Zeeman effect and diagnostics of solar and stellar magnetic fields. II. Synthetic Stokes profiles in the Zeeman regime, Astron. Astrophys., 412, 513–527

Bopp, B. W., 1983, Activity in Red Dwarf Stars, IAU Coll., 71, 363

Bopp, B. W., Dempsey, R. C., 1989, A new orbit for the RS Canum Venaticorum binary Sigma Geminorum, Publ. Astron. Soc. Pac., 101, 516–519

Bopp, B. W., Dempsey, R. C., Maniak, S., 1988, H-alpha spectroscopy of active-chromosphere stars. I - Six G-K giants, Astrophys. J. Suppl. Ser., 68, 803–819

Brown, S. F., Donati, J.-F., Rees, D. E., Semel, M., 1991, Zeeman-Doppler imaging of solar-type and AP stars. IV - Maximum entropy reconstruction of 2D magnetic topologies, Astron. Astrophys., 250, 463–474

Cameron, A. C., Horne, K., 1985, Cool Stars, Stellar Systems and the Sun. Lecture Notes in Physics, 254, 205–+

Collier Cameron, A., Duncan, D. K., Ehrenfreund, P., Foing, B. H., Kuntz, K. D., Penston, M. V., Robinson, R. D., Soderblom, D. R., 1990, Fast Spectroscopic Variations on Rapidly Rotating Cool Dwarfs - Part Three - Masses of Circumstellar Absorbing Clouds on Ab-Doradus, Mon. Not. Royal Astron. Soc., 247, 415–+

Deutsch, A. J., 1957, A method for mapping the surfaces of some magnetic stars., Astron.J., 62, 139–+

Deutsch, A. J., 1958, Harmonic Analysis of the Periodic Spectrum Variables, in IAU Symp. 6: Electromagnetic Phenomena in Cosmical Physics, (Ed.) B. Lehnert, pp. 209–+

Donati, J.-F., Collier Cameron, A., 1997, Differential rotation and magnetic polarity patterns on AB Doradus, Mon. Not. Royal Astron. Soc., 291, 1–19

Donati, J.-F., Semel, M., 1990, Zeeman-Doppler imaging - A new option for magnetic field study of AP and solar-type stars, Solar Physics, 128, 227–242

Donati, J.-F., Semel, M., Carter, B. D., Rees, D. E., Collier Cameron, A., 1997, Spectropolarimetric observations of active stars, Mon. Not. Royal Astron. Soc., 291, 658–+

Duemmler, R., Ilyin, I. V., Tuominen, I., 1997, A new radial velocity curve for the RS CVn star sigma Gem: Constraints on its physical parameters, Astron. Astrophys. Suppl. Ser., 123, 209–218

Eaton, J. A., 1990, Rotational Velocities of G and K Giants, Informational Bulletin on Variable Stars, 3460, 1–+

Eker, Z., 1986, Spectral-line variations in Sigma Geminorum, Mon. Not. Royal Astron. Soc., 221, 947–960

Engvold, O., Ayres, T. R., Elgaroy, O., Jensen, E., Joras, P. B., Kjeldseth-Moe, O., Linsky, J. L., Schnopper, H. W., Westergaard, N. J., 1988, Far-ultraviolet and X-ray emission of the long period RS CVn star Sigma Geminorum, Astron. Astrophys., 192, 234–248

Fried, R. E., Vaucher, C. A., Hopkins, J. L., Sabia, J. D., Krisciunas, K., Chambliss, C. R., Landis, H. J., Eaton, J. A., Hall, D. S., Henry, G. W., 1983, Five years of photometry of Sigma Geminorum, Astrophys. Sp. Sci., 93, 305–311

Goncharskii, A. V., Stepanov, V. V., Kokhlova, V. L., Yagola, A. G., 1977, Reconstruction of local line profiles from those observed in an Ap spectrum., Soviet Astronomy Letters, 3, 147–149

Goncharskii, A. V., Stepanov, V. V., Khokhlova, V. L., Yagola, A. G., 1982, Mapping of chemical elements on the surfaces of Ap stars. I. Solution of the inverse problem of finding local profiles of spectral lines, Soviet Astronomy, 26, 690–+

Gray, D. F., 1988, Lectures on spectral-line analysis: F,G, and K stars, Arva: Ontario Gray, 1988

Gray, D. F., 1992, The Observation and Analysis of Stellar Photospheres, The Observation and Analysis of Stellar Photospheres, by David F. Gray, pp. 470. ISBN 0521408687. Cambridge, UK: Cambridge University Press, June 1992.

Hall, D. S., 1972, A T Tauri-Like Star in the Eclipsing Binary RS Canum Venaticorum, Publ. Astron. Soc. Pac., 84, 323–+

Hall, D. S., Henry, G. W., 1979, Photometric Periods for the Wave in λ And, σGem, and HR 4665, Bull. Amer. Astron. Soc., 11, 630–+

Hall, D. S., Henry, G. W., Landis, H. W., 1977, Sigma 75 Gem: a Bright Variable Similar to HK Lac, Informational Bulletin on Variable Stars, 1328, 1–+

Harper, W. E., 1911, The orbit of σ Geminorum, Journal of the Royal Astron. Society of Canada, 5, 200–+

Harper, W. E., 1938, Publications of the Dominion Astrophysical Observatory Victoria, 6, 224

Hatzes, A. P., 1993, Doppler imaging stars with moderate rotation - The SPOT distribution on Sigma Geminorum, Astrophys. J., 410, 777–784

Henry, G. W., Eaton, J. A., Hamer, J., Hall, D. S., 1995, Starspot evolution, differential rotation, and magnetic cycles in the chromospherically active binaries lambda andromedae, sigma Geminorum, II Pegasi, and V711 Tauri, Astrophys. J. Suppl. Ser., 97, 513–549

Hertzsprung, E., 1924, Note on a peculiar variable star or nova of short duration, Bulletin of the Astronomical Institutes of the Netherlands, 2, 87–+

Hoffleit, D., Jaschek, C., 1982, The Bright Star Catalogue, The Bright Star Catalogue, New Haven: Yale University Observatory (4th edition), 1982

Jankov, S., Foing, B. H., 1992, Tomographic imaging of late-type stars from spectroscopic and photometric rotational modulation. I - Principle and mathematical formulation of the method, Astron. Astrophys., 256, 533–550

Jetsu, L., 1996, The active longitudes of λ Andromedae, σ Geminorum, II Pegasi and V 711 Tauri., Astron. Astrophys., 314, 153–164

Kovári, Z., Strassmeier, K. G., Bartus, J., Washuettl, A., Weber, M., Rice, J. B., 2001, Doppler imaging of stellar surface structure. XVI. A time-series analysis of the moderately-rotating K1-giant sigma Geminorum, Astron. Astrophys., 373, 199–210

Kurster, M., 1993, Doppler Imaging with a Clean-Like Approach - Part One - a Newly Developed Algorithm Simulations and Tests, Astron. Astrophys., 274, 851–+

Kurucz, R. L., 1993, Model Atmospheres (Kurucz, 1979), VizieR Online Data Catalog, 6039, 0–+

Nordgren, T. E., Germain, M. E., Benson, J. A., Mozurkewich, D., Sudol, J. J., Elias, II, N. M., Hajian, A. R., White, N. M., Hutter, D. J., Johnston, K. J., Gauss, F. S., Armstrong, J. T., Pauls, T. A., Rickard, L. J., 1999, Stellar Angular Diameters of Late-Type Giants and Supergiants Measured with the Navy Prototype Optical Interferometer, Astron. J., 118, 3032–3038

Nordon, R., Behar, E., Güdel, M., 2006, On temperature and abundance effects during an X-ray flare on σ Geminorum, Astron. Astrophys., 446, 621–626, `astro-ph/0510023`

Piskunov, N. E., 1990, The Sun and Cool Stars: Activity, Magnetism, Dynamos, IAU Colloq., 130, 309–+

Piskunov, N. E., Rice, J. B., 1993, Techniques for surface imaging of stars, Publ. Astron. Soc. Pac., 105, 1415–1421

Piskunov, N. E., Tuominen, I., Vilhu, O., 1990, Surface imaging of late-type stars, Astron. Astrophys., 230, 363–370

Piskunov, N. E., Kupka, F., Ryabchikova, T. A., Weiss, W. W., Jeffery, C. S., 1995, VALD: The Vienna Atomic Line Data Base., Astron. Astrophys. Suppl. Ser., 112, 525–+

Poe, C. H., Eaton, J. A., 1985, Starspot areas and temperatures in nine binary systems with late-type components, Astrophys. J., 289, 644–659

Press, W. H., Teukolsky, S. A., Vetterling, W. T., Flannery, B. P., 1992, Numerical recipes, Cambridge: University Press, —c1992, 2nd ed.

Rice, J., Wehlau, W., Khokhlova, V. L., Piskunov, N. E., 1981, The distribution of iron and chromium over the surface of Epsilon UMa, in Liege International Astrophysical Colloquia, pp. 265–270

Rice, J. B., 1996, Doppler imaging of stellar surfaces (review), in IAU Symp. 176: Stellar Surface Structure, (Eds.) K. G. Strassmeier, J. L. Linsky, pp. 19–+

Rice, J. B., Wehlau, W. H., Khokhlova, V. L., 1989, Mapping stellar surfaces by Doppler imaging - Technique and application, Astron. Astrophys., 208, 179–188

Rodono, M., Cutispoto, G., Pazzani, V., Catalano, S., Byrne, P. B., Doyle, J. G., Butler, C. J., Andrews, A. D., Blanco, C., Marilli, E., Linsky, J. L., Scaltriti, F., Busso, M., Cellino, A., Hopkins, J. L., Okazaki, A., Hayashi, S. S., Zeilik, M., Helston, R., Henson, G., Smith, P., Simon, T., 1986, Rotational modulation and flares on RS CVn and BY Dra-type stars. I - Photometry and SPOT models for BY Dra, AU Mic, AR Lac, II Peg and V 711 Tau (= HR 1099), Astron. Astrophys., 165, 135–156

Rosseland, S., 1928, Viscosity in the stars, Mon. Not. Royal Astron. Soc., 89, 49–53

Schuessler, M., Solanki, S. K., 1992, Why rapid rotators have polar spots, Astron. Astrophys., 264, L13–L16

Semel, M., 1989, Zeeman-Doppler imaging of active stars. I - Basic principles, Astron. Astrophys., 225, 456–466

Singh, K. P., Slijkhuis, S., Westergaard, N. J., Schnopper, H. W., Elgaroy, O., Engvold, O., Joras, P., 1987, X-ray spectrum of Sigma Geminorum - an RS Canum Venaticorum type binary, Mon. Not. Royal Astron. Soc., 224, 481–487

Smith, S. E., Bopp, B. W., 1982, Stellar surface phenomena - The H-alpha profile in RS CVn stars, Astrophys. Letters, 22, 127–130

Strassmeier, K. G., 1996, Observational evidence for polar spots, in IAU Symp. 176: Stellar Surface Structure, (Eds.) K. G. Strassmeier, J. L. Linsky, pp. 289–+

Strassmeier, K. G., Hall, D. S., Eaton, J. A., Landis, H. J., Barksdale, W. S., Reisenweber, R. C., Powell, B. E., Fernandes, M., Zeigler, K. W., Renner, T. R., Wasson, R., Nielsen, P., Louth, H., Chambliss, C. R., Fortier, G., Grim, B. S., Turner, L. C., Stelzer, H. J., Slauson, D. M., Fried, R. E., Brettman, O. H., Engelbrektson, S., Krisciunas, K., Miles, R., 1988, Starspot modeling of ten years of photometry of the long-period RS CVn binary Sigma Geminorum, Astron. Astrophys., 192, 135–146

Strassmeier, K. G., Hall, D. S., Fekel, F. C., Scheck, M., 1993, A catalog of chromospherically active binary stars (second edition), Astron. Astrophys. Suppl. Ser., 100, 173–225

Strassmeier, K. G., Kovári, Z., Washuettl, A., Weber, M., Rice, J. B., Bartus, J., 2003, Tracing the Spot Evolution on the Moderately-Rotating K1-Giant σ Geminorum, in The Future of Cool-Star Astrophysics: 12th Cambridge Workshop on Cool Stars, Stellar Systems, and the Sun (2001 July 30 - August 3), eds. A. Brown, G.M. Harper, and T.R. Ayres, (University of Colorado), 2003, p. 927-934., (Eds.) A. Brown, G. M. Harper, T. R. Ayres, pp. 927–934

Terebizh, V. Y., 1995a, Image restoration with minimum a priori information, Physics-Uspekhi, 38

Terebizh, V. Y., 1995b, Occamian approach in the image restoration and other inverse problems, Int. J. Imaging Systems and Techn., 6, 358–369

Terebizh, V. Y., Biryukov, V. V., 1992, The image randomness test for inverse problems, Astronomical and astrophisical transactions: the journal of the Eurasian Astron, 6, 37–57

Terebizh, V. Y., Biryukov, V. V., 1994, On the problem of stable image restoration, Astrophys. Sp. Sci., 218, 65–86

Tsuji, T., 1973, Molecular abundances in stellar atmospheres., Astron. Astrophys., 23, 411–+

Unruh, Y. C., 1996, Reliability tests for Doppler imaging, in IAU Symp. 176: Stellar Surface Structure, (Eds.) K. G. Strassmeier, J. L. Linsky, pp. 35–+

Unruh, Y. C., Collier Cameron, A., 1995, The sensitivity of Doppler imaging to line profile models, Mon. Not. Royal Astron. Soc., 273, 1–16

Vogt, S. S., Penrod, G. D., 1983a, Doppler Imaging of spotted stars - Application to the RS Canum Venaticorum star HR 1099, Publ. Astron. Soc. Pac., 95, 565–576

Vogt, S. S., Penrod, G. D., 1983b, Doppler imaging of starspots, in ASSL Vol. 102: IAU Colloq. 71: Activity in Red-Dwarf Stars, (Eds.) P. B. Byrne, M. Rodono, pp. 379–385

Vogt, S. S., Penrod, G. D., Hatzes, A. P., 1987, Doppler images of rotating stars using maximum entropy image reconstruction, Astrophys. J., 321, 496–515

Wade, G. A., Donati, J.-F., Landstreet, J. D., Shorlin, S. L. S., 2000a, Spectropolarimetric measurements of magnetic Ap and Bp stars in all four Stokes parameters, Mon. Not. Royal Astron. Soc., 313, 823–850

Wade, G. A., Donati, J.-F., Landstreet, J. D., Shorlin, S. L. S., 2000b, High-precision magnetic field measurements of Ap and Bp stars, Mon. Not. Royal Astron. Soc., 313, 851–867

Walter, F., Charles, P., Bowyer, S., 1978, X-ray emission from UX ARIETIS - RS Canum Venaticorum systems as a class of coronal X-ray sources, Astrophys. J. Let., 225, L119–L122

Wilson, O. C., 1978, Chromospheric variations in main-sequence stars, Astrophys. J., 226, 379–396

Yi, Z., Elgaroy, O., Engvold, O., Westergaard, N. J., 1997, ROSAT observations of the RSCVn binary σ Geminorum., Astron. Astrophys., 318, 791–796

Zhang, X. B., Zhang, R. X., 1999, Photometry and spectroscopy of the RS CVn system sigma Geminorum., Astron. Astrophys. Suppl. Ser., 137, 217–221

Acknowledgement

Lebenslauf

Name:	Alina Semenova	
Geburtstag:	28.Juni 1980	
Geburtsort:	Pavlograd, Ukraine	
Eltern:	Alexandr Zaika Zoya Zaika	
Staatsbürgerschaft:	ukrainisch	
Schulbildung:	9/1987–6/1997	Grundschule N9, Klasse mit Schwerpunkt Mathematik und Physik, (Pavlograd, Ukraine)
Studium:	9/1997–7/2002	Physikstudium an der Physikalischen Fakultät der Nationalen Universität Kharkiv, Ukraine Abteilung für Physik und Astronomie
	9/2000–1/2001	Bachelorarbeit: "Saturn. System of rings and natural satellites"
	9/2001–7/2002	Diplomarbeit: "Analysis of properties of the polarized continuum radiation of comets "
	3/2003–10/2006	Doktorarbeit am Max-Planck-Institut für Sonnensystemforsschung, Katlenburg-Lindau.